Apprehension of Resistive Characteristics of Plasma Ionized Hybrid Nano Fibrous Silicon

by

Chirag Paladiya

A Thesis Presented in Partial Fulfillment of the

Requirements for the degree of

Master of Applied Science

in

Mechanical Engineering

Faculty of Engineering and Applied science

University of Ontario and Institute of Technology

Oshawa, Ontario, Canada, 2018

© Chirag Paladiya December 4, 2018

Abstract

Literature review done for the study identified number of challenges with the conventional way of manufacturing nano patterned surfaces. Also, it indicated immense potential of nano structured surface as a sensing surface for numerous applications. Without using any complex and expensive conventional nano manufacturing method, synthesis of Hybrid Nano fibrous Silicon structure (HNfSi) was made possible by identifying useful laser and scanning parameters in this study. To employ such structure for various sensing applications as well as new generation batteries and capacitors, understanding of its resistive behavior was quite necessary. In this study, HNfSis bulk resistance and thickness based resistivity with variation in different laser and scanning parameters was studied successfully. Methods like 4-point resistivity measurement and parallel plate electrode configuration was employed to understand resistive behavior of HNfSi. In addition, considering immense surface area available with such structure and its benefits identified with literature review, ImageJ analysis was done to comprehend change in topological constituents and its dimensions with the variation in specified parameters. To understand such change in resistive behavior, various surface and material characterization methods like, SEM (Scanning electron microscope), Raman spectroscopy, light spectroscopy and EDX (Energy-dispersive X-ray spectroscopy) was employed. Overall, with this study, important laser parameters to generate HNfSi was identified successfully and their respective resistive characteristics were understood using mentioned methods.

Acknowledgments

First and foremost, my sincere thanks to my supervisor Dr. Amirkianoosh Kiani for providing me with this opportunity and constantly encouraging me to push my boundaries. He has been a great role model, supervisor, mentor, humble and hard working human-being who motivated me to fulfill my dreams and to be the best version of my self. His guidance has taught me to be positive in any condition and helped me comprehend important virtues for happy and stress free life. I have come so far in my research because of his trust in my abilities and ideal supervision provided by him. I am finishing my work here in UOIT as MASc student with sense of immense satisfaction and accomplishment. Thank you with all my heart! I also want to thanks examining committee members, Dr. Dipal Patel and Dr. Sayyed Ali Hosseini for reviewing my thesis and for their valuable feedback.

I would also like to further acknowledge and thanks all my friends who provided me warmth and comfort being my family away from home through out my journey here as an international student. I feel quite fortunate to get always dreamed multicultural experience with my roommates-cum-family and my beloved friends. I feel blessed to have you all in my life.

Also, I want to thanks all my uncles Kishor, Raju, Hansraj, Manu and all my aunt for their support towards my dreams and to give my family a ray of hope when needed the most.

Dedication

I am dedicating this research to my beloved parents, grandparents and siblings - Darshan and Jalpa for their love and encouragement while completing this work. Thank you for all your efforts and life long compromises you made throughout my upbringing to provide me the best possible opportunities and life that I would never change a bit if I get to live again. Entire credit for whatever I have accomplished till today goes to you all! Thank you!

Contents

Abstract ii

Acknowledgments iii

Dedication iv

Table of Contents v

List of Figures viii

List of Tables xii

Nomenclature xiii

1 Introduction[1] 1

1.1 Relevant sensor characteristics 2

1.1.1 Linearity 2

1.1.2 Hysteresis 3

1.1.3 Response time 4

1.1.4 Signal to noise ratio 5

1.2 Micro/Nano-structured sensing surface 6

1.2.1 Optical sensors 6

1.2.2 Chemical sensors 8

1.2.3 Biomedical sensors 9

1.2.4 Other Sensors 10

1.3 Fabrication: Nano-structured sensing surface 12

1.3.1 Etching techniques 12
1.3.2 Material deposition 18
1.4 Laser ablation and laser processing 28
1.4.1 Laser ablation : Process control 29
1.4.2 Advantages of laser approach 31
1.4.3 Possibilities with laser ablation 32
1.4.4 Research objectives 34

2 Materials and methods 37
2.1 Optical design/setup & laser 37
2.2 Resistivity measurements 38
2.2.1 4-point probe 38
2.2.2 Parallel plate electrode configuration 38
2.3 Dimensional analysis of HNfSi 39
2.4 Surface Characterization : SEM, Energy dispersive X-ray (EDX) and Raman spectroscopy 40
2.5 Light spectroscopy 40
2.6 Statistical analysis 41

3 Theoretical background 42
3.1 Temperature generation with laser ablation 42
3.2 Resistivity measurements 44
3.2.1 Four point probe 44
3.2.2 Parallel electrode configuration 45
3.3 Surface topology for sensing [2] 47
3.3.1 Surface area enhancement with nano particles 47
3.3.2 Nanofiber diameter for sensors 48
3.3.3 Critical silicon nanowire diameter 50

4 Effects of laser frequency, power and scanning loops[3] 52
4.1 Effects of variation in laser frequency 54

4.2 Effects of variation in laser power 59
4.3 Effects of number of scanning loops 64

5 Effects of laser ablation temperature and leading distance 69

5.1 Introduction 69
5.2 Effects of change in plasma temperature 70
5.3 Variation in leading for surface scanning 77

6 Research summary and future work 84

6.1 Effects on surface topology 85
6.2 Effects on resistivity 87
6.3 Future work[4] 88

List of Figures

1.1 Nanofiber generation on silicon substrate using laser ablation 30

2.1 Experimental setup for HNfSi fabrication. 38

2.2 Parallel plate electrode configuration for thickness based resistive characterization of HNfSi. 39

3.1 Four point probe for thin film resistance measurement. 45

3.2 HNfSi accommodation between two copper electrodes with figurative demonstration of heat affected zone (HaSi). 46

3.3 Surface area with miniaturization of the same volume. 47

3.4 Effect of nanowire diameter on sensitivity. 49

4.1 (a) Formation of nano fibers caused by accumulation of Re-solidified Silicon Nano-particles (R-SiNp). (b) SEM result of laser ablated silicon surface - mixture of nano particles and nano fibers. 52

4.2 Raman spectroscopy results for HNfSi. 53

4.3 (a) EDX result for the spot with R-SiNp on HNfSi (b) EDX results for spot with dense silicon nano fibers on HNfSi. 54

4.4 SEM images (resolution of 50,000X and 10,000X) of HNfSi produced by laser processing with repetition rate of (a) 600 kHz (b) 800 kHz and (c) 1200 kHz. 55

4.5 Comparison of distribution of (a) nano fiber (using 50,000X SEM image) and (b) R-SiNp (using 10,000X SEM image) diameter for HNfSi prepared with frequency of 1200 kHz, 800 kHz and 600 kHz. 55

4.6 Comparison of (a) nano fiber (using 50,000X SEM image) and (b) R-SiNp (using 10,000X SEM image) mean diameter for HNfSi prepared with frequency of 1200 kHz, 800 kHz and 600 kHz. 56
4.7 4-Point resistivity measurement of HNfSi processed with laser frequency of 1200 kHz, 800 kHz and 600 kHz. 57
4.8 EDX results for HNfSi processed with frequency of (a) 1200 kHz (b) 800 KHz and (c) 600 KHz with (d) presence of silicon and oxygen by weight%. 57
4.9 Light spectroscopy analysis for HNfSi processed with laser frequency of 1200 kHz, 800 kHz and 600 kHz 58
4.10 SEM images (resolution of 50,000X and 10,000X) of laser processed HNfSi with power level of (a) 10 W (b) 15 W and (c) 20 W. 59
4.11 SEM images (resolution of 50,000X and 10,000X) of laser ablated HNfSi with power of 20 W, 15 W and 10 W. 60
4.12 Comparison of (a) nano fiber (using 50,000X SEM image) and (b) R-SiNp (using 10,000X SEM image) mean diameter for HNfSi prepared with power of 20 W, 15 W and 10 W. 61
4.13 4-Point resistivity measurement of HNfSi processed with power of 10 W, 15 W and 20 W. 62
4.14 EDX results for HNfSi processed with laser power of (a) 20 W (b) 15 W and (c) 10 W with (d) presence of silicon and oxygen by weight%. 62
4.15 Light spectroscopy analysis for HNfSi processed with laser power of 20 W, 15 W and 10 W. 63
4.16 SEM images (resolution of 50,000X and 10,000X) of laser processed HNfSi prepared with number of loops - (a) 1 (b) 2 and (c) 3. 64
4.17 Comparison of (a) distribution and (b) mean of fiber diameter for HNfSi prepared with variation in scanning loops from 1 to 3. 65
4.18 4-Point resistivity measurement of HNfSi prepared with variation in scanning loop from 1 to 3. 65

4.19 EDX results for HNfSi prepared with laser scanning loop of (a) 1 (b) 2 and (c) 3 with (d) presence of silicon and oxygen by weight%. 66
4.20 Light spectroscopy analysis for HNfSi fabricated with variation in scanning loops from 1 to 3. 67

5.1 For various pulsation width, plasma temperature ΔT at Si surface with respect to (a) depth of the surface being processed and (b) radial distance from the center of focused laser spot. 71
5.2 Variation in thickness of HNfSi i.e. T(HNfSi) with change in pulsation width along with cross section image of respective HNfSi. . . . 72
5.3 Resistivity offered by HNfSi i.e. R(HNfSi) when prepared using laser plasma processing with various pulsation width. 73
5.4 (I) SEM images (resolution of 10,000X and 50,000X) of laser plasma processed silicon surface with pulsation width of (a) 1 ns (b) 2 ns and (c) 5 ns. (II) (a) Analysis of nanofibers with available diameter range (b) Change in mean diameter of nanofibers with change in pulsation width. 74
5.5 (I) Raman spectroscopy and (II) Light spectroscopy results for samples processed with pulsation width of 1 ns, 2 ns and 5 ns. 76
5.6 Gaussian profile of laser spot with its theoretical radius and three scenarios of laser plasma processing with change in leading values *(L)* of (I) 0.0125 mm, (II) 0.025 mm and (III) 0.05 mm. 78
5.7 Variation in HNfSi thickness i.e T(HNfSi) with change in leading along with cross section image of respective HNfSi. 79
5.8 Resistivity offered by HNfSi i.e R(HNfSi) when prepared using laser plasma processing with various values of leading. For employed resistivity measuring setup , ∞^* represents highly resistive nature of HNfSi approaching to non-measurable resistivity values when processed with leading value of 0.0125 mm. 80

5.9 (I) SEM images (resolution of 10,000X and 50,000X) of laser plasma processed silicon surface with leading of (a) 0.0125 mm (b) 0.025 mm and (c) 0.05 mm. (II) (a) Analysis of nanofibers with available diameter range (b) Change in mean diameter of nanofibers with change in leading. 81

5.10 (I) Raman spectroscopy and (II) Light spectroscopy results for samples processed with leading values of 0.0125 mm, 0.025 mm and 0.05 mm. 82

6.1 SEM and TEM image of HNfSi with Graphite nano particles embedded on it. 89

6.2 Conductivity of Silicon and HNfSi with various concentration of Graphite embedded on it. 89

6.3 For various laser frequencies, plasma temperature ΔT at Si surface with respect to (a) radial distance from the center of focused laser spot and (b) depth of the surface being processed. 124

6.4 For various laser power values, plasma temperature ΔT at Si surface with respect to (a) radial distance from the center of focused laser spot and (b) depth of the surface being processed. 124

List of Tables

1.1 Sensitivity comparison of PtTFPP based oxygen sensor with various probe geometry. 7

1.2 Comparison of operating temperature, minimum possible detection and probe geometry with different dopant in ZnO based CO chemical gas sensor. 9

1.3 Interferometry based pressure sensor 14

1.4 Different etching approaches for fabrication of solar cell surface (Silicon $< 100 >$) with different surface texture and reflectivity. 18

1.5 Change in sensitivity of WO_3 based NO_x detection sensor with respect to sensing surface characteristics 20

1.6 SnO_2 based sensor for C_2H_5OH detection fabricated using E-beam PVD 23

1.7 Graphene based sensors fabricated using CVD which exhibits extraordinary sensing capabilities. 25

1.8 General challenges offered by contemporary material deposition methods. 27

1.9 Topology change on porous silicon with respect to various laser process parameters. 33

6.1 Topological characterization of HNfSi with variation of various processing and laser parameters. 86

6.2 Topological characterization of HNfSi with variation of various processing and laser parameters. 87

Abbreviation

HNfSi = Hybrid Nano Fibrous Si/SiO_2 structure

PDMS = Poly-(dimethylsiloxane)

PtTFPP = Platinum (II) meso-tetrakis-(pentafluorophenyl)prophyrin

PSU = Polysulfone

PCL = Polycaprolactone

SNR = Signal-to-Noise Ratio

DNA = Deoxyribonucleic Acid

MRI = Magnetic Resonance Imaging

MEMS = Micro-Electro-Mechanical Systems

NEMS = Nano-Electro-Mechanical systems

SWCNT = Single Walled Carbon Nano Tubes

R-SiNp = Resolidified Silicon Nano Particles

QCM = Quartz Crystal Microbalance

PAA = Polyacrylic Acid

PVA = Poly(vinylalcohol)

F-P = FabryProt

SMF = Single Mode Fiber

RIE = Reactive Ion Etching

AOO = Anodic Aluminum Oxide

PECVD = Plasma Enhanced Chemical Vapor Deposition

PVD = Physical Vapor Deposition

ALD = Atomic Layer Deposition

TBCs = Thermal Barrier Coatings

PLD = Pulsed Layer Deposition

SERS = Surface Enhanced Raman Scattering

EDX = Energy dispersive X-ray

SEM = Scanning Electron Microscopy

TEM = Transmission Electron Microscopy

Chapter 1

Introduction[1]

Any ultra modern complex systems designed to work automatically or employing integrated semi-automatic mechanisms employs number of sensors and actuators to accomplish the purpose. One possible basic function of a sensor in such systems is to respond according to the change in a property or analyte concentration. Sensing surface in sensor is a vital component which detects the mentioned change. Interruption or initiation of the signal through sensing surface is elevated or transformed using transduction element which further helps the processing unit to calculate the measurand. In addition, with latest developments, trend of miniaturization within semi conductor industries have driven researchers to employ nano technology to facilitate and advance desired functioning and improved performance of sensors within a relatively smaller footprints.

Sensors can be classified based on various characteristics. Considering contact between sensing surface and analyte, it can be classified as contact and non-contact type of sensor. For example, laser sensors being used for measuring linear distance is classified as non-contact sensor because sensing surface does not require any direct contact to physical object to measure the distance of interest [1–3]. However due to required contact to alter resistance or capacitance associated with related pixel grid, in general, touch screen would considered to be a contact sensor [4, 5].

[1]Chapter 1 has been published as a review paper titled 'Nano structured sensing surface: Significance in sensor fabrication' in Elsevier journal Sensors and Actuators B. `https://doi.org/10.1016/j.snb.2018.04.085`.

Furthermore, depending on the nature of a sensor to produce or alter a signal, it can be classified as passive or active sensor. For example, simple strain gauge utilizes the change in resistance to measure the applied load or pressure which can be considered an active sensor. However, piezoelectric strain gauge initiates its own signal with respect to applied load or pressure eliminating the requirement of external energy source. Hence, it can be considered as passive sensor [6, 7]. Moreover, depending on the transduction requirements, sensors can be classified as either direct or hybrid sensors. For example, piezoelectric sensors convert or amplify generated signal for further processing requiring no extra transduction which can be identified as a direct sensor. However, some of the chemical sensors needs extra transduction element to generate or alter electrical signal to measure heat produced by first transducer from exothermic chemical reaction in analyte. Such sensors can be classified as hybrid sensors [8–11]. Furthermore, depending on the required data processing to generate useful statistical or visual demonstration of measured change, sensors can be classified as analog and digital sensors [1].

1.1 Relevant sensor characteristics

1.1.1 Linearity

Study of the sensor characteristics is quite important as it determines sensors' feasibility in certain application. Linearity of sensor is vital for accurate measurement throughout sensing range. Employment of MEMS (Micro-Electro-Mechanical Systems) pressure sensor by automobile, HVAC (Heating, Ventilation, and Air Conditioning), process control and aviation industries is common [12–15]. However, with the case like MEMS piezoresistive pressure sensor with flatbed diaphragm, sensitivity is proportional to ratio of diaphragm width to diaphragm thickness. Hence, sensitivity can be increased by employing larger width and thickness ratio. In contrary, the non-linearity error increases drastically with increase in such ratio at much faster rate. Therefore, it is difficult to achieve linearity and high

sensitivity for long range at the same time [16, 17]. As a solution, Aravamudhan et al. [18] have demonstrated the use of micro structure modification by employing double diaphragm instead of single diaphragm and resistivity measurement using wheatstone bridge network for MEMS piezoresistive pressure sensor which achieved sensitivity of $\approx 5.51\ mV/kPa$ with significant linearity. In contrary, Huang et al. [16] followed different approach of employing peninsula-structured diaphragm which achieved linearity on a wide range of pressure up to 5 kPa with sensitivity of 18 mV/kPa.

Introducing higher surface area to sensing surface and smaller probes enables higher linearity for humidity sensors. Higher sensor linearity in the case of Zinc Oxide (ZnO) nanowires with compare to ZnO nanorods is achieved in studies done by Zhang et al. [19]. Similarly, Su et al. [20] and Wang et al. [21] fabricated sensing surface consisting nano particles made of SiO_2 composed with poly(2-acrylamido-2-methylpropane sulfonate). Such sensor performed linearly over the range of $30-90\%$ of relative humidity. However, when nanofiberous structure made of quartz crystal microbalance (QCM) (coated with composition of polyacrylic acid (PAA)/poly(vinylalcohol) (PVA)) was used, with increased surface area, sensor performed linearly over wider range of $20-95\%$ of relative humidity.

1.1.2 Hysteresis

Apart from linearity, humidity sensors also suffer from sensor hysteresis which is the lag in response exhibited by a sensor in reacting to changes during sensing in different directions. The formation of cluster of sorbed water molecule on the sensing surface is the reason of hysteresis in humidity sensors [22]. These molecules can be removed by thermal passivation, vacuum or chemical passivation. Paska et al. [23] have introduced and established a new concept on involving material with higher molecular density or hydrophobic behavior on the sensing surface which reduces surface hydroxyl sites causing relatively less intense hysteresis. Hence, depending on the probe material and surface condition, the hysteresis of the sensor

can change. For example, in humidity sensor, Geng et al. [24] have used composites of mesoporous silica in their study which exhibits hysteresis of almost 4% while Wu et al. [25] have used composite nanofibers of Titanium dioxide(TiO_2) and Nafion which provides relatively higher surface area as a sensing probe and exhibits hysteresis of less than 2%.

In similar manner, sensors made with surface bounded carbon nanotubes for optical, chemical and displacement applications experience high hysteresis because charge trapped between substrate and ambient air while charge transfer between nano tubes [26,27]. Compared to nanotubes bounded on substrate, the approach of having two electrical gates with suspended single wall nanotube was employed by Cao et al. [28] which becomes hysteresis free after initial few seconds of operation. It can be because of reduced number of nanotubes resulting in a less trapped charges which can cause relatively low hysteresis. For further improvement, Muoth et al. [29] have integrated a different approach of direct growth of ultraclean and individual nanotube on non metal contacts following by deposition of palladium on the contacts instead of post- or pre-growth of nanotubes on metal contacts which exhibit gate hysteresis. The modification enabled sensor to achieve almost hysteresis free sensing.

1.1.3 Response time

In the same way, sensor response time, the dynamic sensor characteristic is also a deal breaker for real time monitoring. For example, sensors being used as gas or liquid flow meter need to be responsive for accurate and real time monitoring in critical applications. Additionally, power consumption and sensor size are also vital considerations for the modern devices. Kim et al. [30] fabricated MEMS sensor having diaphragm with heater element patterned on it. It was designed for flow direction and velocity detection based on the thermal anemometer principle with sensing probe having dimension of $3\ mm \times 3\ mm \times 0.52\ mm$. The sensor had response time of maximum up to 9 seconds with power consumption of 80 mW.

Velocity detection response time went down to 0.5 s with lower operating power of 0.15 mW when Wang et al. [31] used silicon nitride coated piezoresistor cantilever beam with width of 400 μm which was capable of detecting higher flow velocity up to 40 ms^{-1}. To exhibit the similar quality of low power consumption and potential with detection of extremely slow velocity up to 0.1 mm/s, Cubukcu et al. [32] used 2D array with diaphragm (thickness - 1.4 μm) made of $SiN_X - SiO_X$ (Silicon-Nitrogen and Silicon-Oxygen compounds) and thermistors with dimension of more than 7 μm. Overall, with relatively smaller heater element, it exhibited the average response time of 10 ms and sub-mW of power consumption. To conclude, with appropriate sensing method, reduced complexity and smaller footprint of device, it can operate with relatively lower power consumption and gain comparatively faster response.

1.1.4 Signal to noise ratio

For any particular setup and condition with a sensor, the ratio of smallest clearly measurable/identifiable signal to the maximum available random noise is known as Signal-to-Noise Ratio (SNR). This sensor characteristics is vital because transmission of signal representing any measurand can significantly affected by random noise experienced by the system. Hence, higher SNR is always desirable for any sensing device. Researchers have used smaller sensing probes with the higher surface area to achieve higher resolution by gaining high signal to noise ratio [33–36]. For example, Mu et al. [37] achieved SNR of 3 at minimum possible detection of 0.16 μM glucose by using nano particles (average diameter ϕ 20 nm) of NiO (Nickel oxide) mixed with carbon paste electrodes. In addition, Chikkadi et al. [38] have used nanotubes suspended between metal electrode for gas sensors with dry transfer technique causing elimination of process contamination and oxide charge traps which improved the SNR by 9 times with respect to SiO_2 gas sensor with substrate bound carbon nanotubes.

Overall, surface condition and topology play vital role in sensors' static char-

acteristics like sensitivity, resolution, hysteresis, linearity, and dynamic characteristics like response time. As mentioned, nano structuring of the sensing surface improves important sensor characteristics. Moreover, such basic change enables its use in various fields of applications. Use of such surface in various types of sensors are on immense surge because of numerous benefits. Following section includes brief literature review of different types of sensors with their performance and feasibility varying with change in sensing surface topology.

1.2 Micro/Nano-structured sensing surface

Trend of miniaturization has driven researchers to develop new concepts and modify existing approaches to be able to adopt sensing surfaces with nano particles and nano pores as they provide increased surface area with improved performance. Such trend will be discussed in following sections with context to various types namely, optical, chemical and biomedical sensors etc.

1.2.1 Optical sensors

Optical sensors are relatively versatile considering the possibility of translating physical properties into optical working principles. Because of variety of key parameters associated with optical properties such as wavelength, frequency and diffraction, optical sensors are employable for vast variety of applications in fields like automobile, aviation, biomedical and manufacturing [39–42]. The significance and trend of employing nano structured surfaces can be understood by the example of PtTFPP based oxygen sensors. Bedlek-Anslow et al. [43] first demonstrated concept of PtTFPP dispersed or dissolved on PDMS to be used as a gas sensor. To enhance the surface area with nano structured entities, Mao et al. [44] used same dye with binder material with micro pillar formation instead of flat surface configuration. Increased area contributed to ≈ 30 fold increase in sensitivity of the oxygen sensor. As the probe distribution was difficult with PDMS binding material, to

achieve further miniaturization, instead of PDMS, Xue et al. [45] used PtTFPP doped nano fibers with PSU core coated by PCL shell to enable biocompatibility of the sensor. In such a case, fabrication of nanofibers using electro-spinning provides better probe distribution with increased surface to volume ratio. In addition, oxygen affinity associated with material elevates the sensitivity of the sensor significantly. Figure 1.1 shows summery of PtTFPP based gas sensors and related performance measures.

Probe	**Polymer Matrix**	**Sensing Surface Geometry**	**Sensitivity**	**Respo. Time**	**Ref.**
PtTFPP	PDMS	Thin film with thickness of 5 μm	$Ksv^G \approx 0.02\ hpa^{-1}$	-	[43]
PtTFPP	PDMS	Pillar arrays ϕ $50 \times 40\ \mu m$ length with Pitch of 150 μm	$Ksv^G = 0.29\ hpa^{-1}$ $Ksv^L \approx 1.837$ $(mg/L)^{-1}$ $I_0/I^L_{100@DO5mg/L} = 10$	16.8 s	[44]
PtTFPP	PSU core coated with PCL	Thin film of 100 μm with layer of nano fibers ϕ $394 - 997$ nm	$Ksv^{L-PSU} = 3.16$ $(mg/L)^{-1}$ $I_0/I^L_{100@DO5mg/L} = 15$	$0.38 \pm 0.03\ s$	[45]

Table 1.1: Sensitivity comparison of PtTFPP based oxygen sensor with various probe geometry.

Similar advantage was noticed when nano particles and nano porous surface were employed for sensors to detect heavy metal ions from the common environmental pollutants. For example, Verma et al. [46] have used thin film made of silver and indium tin oxide coated with composite made of pyrrole and chitosan to detect ions of cadmium (Cd^{2+}), lead (Pb^{2+}) and Mercury (Hg^{2+}). Such use of plasmon resonance (SPR) approach enabled detection of those pollutants with minimum concentration of 0.293 nM. However, change in topological structure with enhanced surface area and improved approach could enable detection with even smaller concentration. For example, Balaji et al. [47] have reported use of optically transparent cage silica monoliths having highly ordered mesoporous structured cubes with space-group of fm3m for detection of Pb^{2+}, Cd^{2+}, Sb^{3+} (Antimony) and Hg^{2+}. The method allowed detection of heavy metal ions by

noticeable change in color of the sensing surface visible with naked eyes at even lower concentration of 0.01 nM (nanomolar).

1.2.2 Chemical sensors

In general, chemical sensors employ two basic components - a molecular recognition system and the physiochemical transducers. Sensing surface, (also known as receptors) being key element of sensor, which interacts directly with the analyte molecules. Very common interaction between those two can be adsorption, ion exchange or liquid to liquid extraction. Due to these possibilities, chemical sensors are heavily employed in various applications [48–50]. Undesirable change in climate conditions due to global warming and production of unwanted gases are becoming major challenges in modern era. Hence, for environmental observations and other similar purposes, analysis of gas compositions is one of the most common use of chemical gas sensors [51, 52].

Furthermore, nano structuring of the sensing surface with improved approach can enhance the performance of related chemical gas sensors. Generally, metal oxide thin film senors have receptors which transfers the charges to and fro with analyte species in interest. Following the same ideology, Müller et al. [53] demonstrated possible use of ZnO (Zinc Oxide) thin film as chemical sensor. Such chemical gas sensor had silicon wafer as base material with sputtered ZnO thin film on the top having thickness ranging from 80 to 2000 nm. Similarly, recent studies have proven the potential of ZnO for the CO sensing applications [54–57]. However, ZnO based gas sensors needed major improvement considering its high operating temperature of $\approx$ 400 ℃ and poor gas selectivity [58]. To improve the operating temperature with enhanced performance and to lower the resistance for minimized electrical consumption in ZnO based gas sensors, approach of doping of conductive material was followed in further studies [59, 60]. Such inclusion of dopant material, depending on dopant's inherent characteristics (i.e atomic properties) and the way of insertion into host material can alter overall crystalline

structure, defects and surface area of related sensing element. In addition, its basic or acidic property can affect the affinity towards particular gas [61]. Therefore, selection of dopant material with relevant structuring of sensing surface can significantly affect the performance of ZnO based gas sensor. Summery of such sensors for detection of CO gas has been discussed in table 1.2. Overall, the improvement in terms of lowered operating temperature and high detection limit can be achieved through the help of appropriate doping material along with nano structured sensing surface [61–64].

Probe	**Dopant**	**Operating Temperature**	**Probe Dimensions (Average)**	**Minimum possible detection of CO**	**Ref.**
ZnO	Ga	300 ℃	Crystalline Size of 55 nm with Grain Size of 120 nm	5 ppm	[61]
ZnO	Au	250 ℃	ZnO and Au film thickness, in order - 40 nm, 2 nm	5 ppm	[62]
ZnO	Cu	150 ℃	Crystalline grains of $\approx \phi$ 5 nm	6 ppm	[64]
ZnO	Pd	Room Temperature	Nano dots of ϕ 10 nm with interplanar distance of 0.39 nm, 600 Nano dots per μm	100 ppb	[63]

Table 1.2: Comparison of operating temperature, minimum possible detection and probe geometry with different dopant in ZnO based CO chemical gas sensor.

1.2.3 Biomedical sensors

Sensors employed in biomedical applications can be considered relatively crucial as their performance may affect living entity or organ directly or indirectly. For example, modern implantable biomedical sensors can measure heat, flow rate, pressure, electrical, and chemical properties inside the living organ [65]. In addition, with possible miniaturization in cell phone technology and semiconductor industry, it is possible to manufacture widely affordable biomedical sensors embedded on the

patches and wearable gadgets to monitor heart rate and activity monitoring for calories burnt [66]. However, the application of implantable sensors remain strictly restricted for research purposes because of the size and constrain related to limited battery life and constant power supply [67]. However, because of promising possibility of miniaturization, relevant physiochemical property, and vast applicability, the study of biomedical sensors has been escalated quickly. For instance, the research for magnetic actuation, use of magnetic particles for the MRI (Magnetic Resonance Imaging) and study of sequencing of DNA (Deoxyribonucleic Acid) has already established the potential of the biosensors [68–71].

In addition, for some critical applications, biomedical sensor must have capacity to measure extremely small quantities of entity of interest. For instance, measurement of magnetic signal produced by organs with the order of 10^{-10} T [65]. Also, extremely small measurement is required while identifying DNA translocations as it occurs with the speed of $\mu s\ Base^{-1}$ producing very short pulse of ionic current with the order of picoampere [72]. To overcome the problem, in many studies, the researchers have focused on measuring those small ionic currents using nano probes and nano pores [73–76]. Additionally, extremely small detection is also necessary when it comes to sensing of heavy metals in various medium for health and environment monitoring. For such detection, researchers have already proven the potential of enzyme based nano biosensors through studies [77–80]. Apart from high surface to volume ratio for small detection, according to some studies, nano porous structures can be beneficial for low signal-to-noise (SNR) ratio [81–84]. Overall, requirement of high accuracy and measurement of extremely small quantity have driven researchers to use nano probes or nano porous surfaces.

1.2.4 Other Sensors

As discussed, for improved performance and enhanced suitability, importance of nano structured sensing surface in the field of optical, chemical and biomedical sensors can be understood using examples. Similar to these types of sensors, as men-

tioned, advancement in the MEMS and Nanoelectromechanical systems (NEMS) have encouraged researchers to develop miniature sensors to monitor new generation electric devices [85–87]. Such miniaturization has driven researchers towards using nano structured surfaces and nano probes for accurate and precise sensing. Huang et al. [88] and Zhang [89] have shown the potential of nano structured sensing surface for relatively higher sensitivity of acoustic wave sensor. Similarly, the study done by Pramanik et al. [90] shows the possible use of porous silicon membrane for the pressure sensing application. Additionally, porous silicon has much shorter response and consume less energy than the bulk silicon piezoresistive pressure sensors [90–92].

Furthermore, to enable the next phase of cell phone technology, flexible touchscreen is being researched excessively. Adaption of nano structured surface with relevant material can be a deal breaker approach in such cases. For example, Ramuz et al. [93] has demonstrated potential of film made of nano structured PDMS as flexible, transparent, and stretchable pressure sensitive skin. Furthermore, in resent research, for the photo detection application, the potential use of single walled carbon nano tubes (SWCNT) was demonstrated in studies done by Nanot et al. [94] and St-Antoine et al. [95]. Also, SWCNT sensing surface offers extremely fast response up to picosecond and compatibility to work with infrared light with broadband [96, 97].

Overall, nano structured sensing surface has significant potential for accurate and precise sensing in variety of field along with possibilities for improvement. Furthermore, numerous techniques are employed to manufacture such nano structured surfaces as discussed in the following section. Nature of the manufacturing processes along with the associated feasibility and offered advantages with inherent limitations can affect the performance and practicality of the sensor for various applications. Following section includes a brief discussion on the effect of various fabrication methods on the sensors' performance and practicality of approach.

1.3 Fabrication: Nano-structured sensing surface

Immense research and development of nano technology was perhaps enabled because of commercialization of nano technology in semiconductor industry, MEMS device manufacturing and medical research [98–100]. Deposition of particles at nano scale and generation of thin films, various lithography techniques, etching and patterning are the key approaches being used for major micro and nano manufacturing applications [101]. Further discussion is based on major nano manufacturing techniques and their use in the context of sensing surface fabrication with their respective advantages and challenges.

1.3.1 Etching techniques

Etching process is considerably older than all other nano-fabrication processes. Use of etching processes for manufacturing and engraving is mentioned in the literatures as early as 1645 [102]. Since 1950s, The modern versions of the etching techniques have been accepted as one of the most significant unconventional manufacturing processes for micro and nano fabrication [103]. Wet and dry etching, plasma and ion-beam assisted etching are few types of modern etching techniques. The versatility of the etching process makes it feasible to be used at different level of manufacturing stages to serve various purposes. For instance, as demonstrated by Zhu et al. [104] it can be used as the main process to manufacture sensor surface or it can be used as a part of manufacturing process as mentioned in study done by Abeysinghe et al. [105]. Additionally, it can be used for post processing to improve performance of certain sensing devices as well [106].

1.3.1.1 Wet etching

Wet etching first enabled the material removal at micro level without any physical interaction. For example, the concept of basic fiber optic pressure sensor using two small plates with optical fiber in the middle was first introduced by Fields et al. [107] in 1980. The sensor itself had a dimension to the scale of centimeter.

Further miniaturization of the fiber optic sensor up to the scale of millimeter became possible when the new concept of measuring change in frequency of quartz crystal under longitudinal tension by using optical fiber was employed by Ingold et al. [108]. With the help of the etching, it was first possible to further reduce the size of Fiber-optic sensors upto micro level by following approach of FabryProt (F-P) interferometry. Therefore, fiber optic sensor fabricated by Abeysinghe et al. [109] has a cavity generated by wet etching of fiber core by buffered hydrofluoric acid solution on the top end of the fiber which has diameter of 200 μm, which was then enclosed by diaphragm with a thickness of 7 μm. The sensor had a capacity to respond linearly in the range of $\approx 0 - 551\ kPa$. In many F-P interferometry based sensors, the adhesive used for the packaging of the sensor limited its operating temperature. To overcome the problem of temperature limitations with the sensor working with same principle and with almost similar size, Zhu et al. [110] used all-fused-silica structure developed using wet chemical etching by hydrofluoric acid combined with fusion splicing and cleaving process. The sensor could perform linearly in the range of $\approx 137 - 1310\ kPa$ in temperatures as high as 530 ℃. One of the problems with the diaphragm based FabryProt (F-P) interferometry sensors was the damage to diaphragm when it was handled under over stressed conditions.

To overcome the problem, researchers employed techniques that do not require diaphragm manufacturing using etching as it may limit the miniaturization. Li et al. [111] proposed use of Mach-Zehnder interferometer based sensor with twin core (elliptical core with minimum diameter of 6.5 μm) fiber between two single core fibers. Femtosecond laser was used for drilling through one core of twin fiber and other was remained as reference arm. Such sensor exhibited high sensitivity and ability to function accurately under 2 MPa of pressure without any danger of failure caused by relatively high pressure. Contrary, the sensor exhibited significant error with temperature variation. To overcome such limitation, Liu et al. [112] developed a sensor which overcame these difficulties with high temperature operation capabilities and larger pressure range by using electrical arc discharge in conjunc-

tion with single mode fiber (SMF) to fabricate sub micro pressure sensor. The sensing probe employed extremely thin diaphragm made without using etching. Furthermore, table 1.3 depicts the summery of discussion in this section.

Sensor Information	**[109]**	**[110]**	**[111]**	**[112]**
Interferometry Type	Fabry-Prot	Fabry-Prot	Mach-Zehnder	Fabry-Prot
Fiber Diameter and Material	Borosilicate multi-mode glass fiber ϕ 200 μm	All fused silica structure with silica fiber ϕ 125 μm	Twin core fiber between two single mode fiber ϕ 125 μm	Silica fiber ϕ 125 μm with diaphragm-sealed cavity
Fabrication method	Wet etching using buffered HF	Wet etching using HF combined with fusion splicing and cleaving	Femtosecond laser-machining and drilling	Electrical arc discharge technique
Diaphragm Thickness	7 μm	4.08 μm	elliptical core $\approx \phi$ 6.5 μm	Less than 170 nm
Linear pressure range	$\approx 0 - 551$ kPa	$\approx 137 - 1310$ kPa	$\approx 68 - 1999$ kPa	$\approx 0 - 1999$ kPa
Operating Temperature	Similar to operating temp. of silica glass fiber	Tested with linearity @500 ℃ for ($\approx$ 172 − 1034) kPa	Tested @ room temp. Exhibits error of 4.4 kPa/℃	Linear behavior when tested up to 1100 ℃. Exhibits error of 0.10 kPa/℃

Table 1.3: Interferometry based pressure sensor

Despite wet etching process being simple, cost effective, selective and suitable for high throughput, it possesses significant limitations which forces researcher to further modify it. In some cases, the surface structuring process control is difficult with wet etching [113, 114]. Additionally, when wet etching is used in subsequent operations or in a step fashion, the contamination may take place which needed to be removed by further cleaning processes [115]. In addition, often wet etching also requires chemicals that are not environmental friendly. In many cases, it

produces undesired notches, undercut and pinholes in the structure. The structural accuracy in certain process like e-beam evaporation and sputtering is difficult to achieve because of difficulty in controlling surface roughness, swelling problems, and difficult residual stress control with wet etching processes. Furthermore, the process is slow and quite expensive and has a patterning limitation up to few microns [116–121]. In addition, for materials like silicon, the etch characteristics would change depending on the crystalline orientation which affect the versatility of the wet etching process [122].

1.3.1.2 Dry etching

Some of the problems faced with wet etching can be overcome by using dry etching processes. Comparatively higher resolution can be achieved using dry etching since it does not have intense isotropy problem as wet etching. In addition, dry etching also noticeably limits the amount of toxic chemicals which can be significant in case of wet etching and difficult to dispose because of toxic and corrosive nature of the chemicals [114,123]. To achieve desired results in terms of surface geometry patterning, generally, dry etching process is accompanied by lithography process. Francioso et al. [124] used photo lithography followed by dry plasma etching to manufacture array of TiO_2 strips with width of 500 nm and pitch of 800 nm, deposited on silicon substrate for gas sensing application. The comparison of the results state the effectiveness of patterned sensor in terms of response (I_{gas}/I_{air}) is $\approx$ 9 times better than the sensor with solid film with similar doping and in same operating condition with presence of 2% ethanol in dry air.

Considering requirement of expensive mask in photo lithography process and difficulty to manufacture it along with hindrance of lithographic resolution, Epifani et al. [125] used multiphase RIE patterned TiO_2 with interspersed Pt nano crystals with size of 2-3 nm. The sensor was capable to detect H_2 with concentration as low as about 1000 ppm. Furthermore, unlike conventional mask used by Francioso et al. [124], Lu et al. [126] used unconventional etching mask template made of

Anodic Aluminum Oxide (AAO) array. By integration of AAO and reactive ion etching (RIE), a modified version of dry etching process, was used to generate TiO_2 (Titanium dioxide) macro porous surface on silicon substrate with pores ranging from 100 nm to 700 nm. The sensor employing this surface exhibited almost double the sensitivity of a sensor having non-porous surface. At room temperature, it could detect 500 ppm concentration of O_2 gas with 8% sensitivity ($S = (R_0 - R)/R_0 \times 100\%$, where R and R_0 are resistance with and without presence of analyte gas). Additionally, it is also possible to further reduce patterning size by using Deep Reactive Ion Etching (DRIE) as demonstrated by Lee et al. [127]. The group was successfully able to develop an array of random silicon nanotips with radius of 20 to 100 nm on silicon substrate for micro sun sensor for Mars rovers.

Despite having significant advantages over wet etching; dry etching offers some difficulties as well. Generally, dry etching process is relatively costly because of time required for the process and sophisticated equipment [128]. The etching rate with all the gases are not similar hence some of them offer really low etching rate and lower selectivity [129]. Additionally, some of the dry etching techniques cause isotropy problems and releases the heat which can alter the dimension of etched structure [114]. Some of the problems offered by etching techniques can be confronted by modification and combination of various approaches like demonstrated by Alavi et al. [130], who used laser machining with the etching process to achieve high aspect ratio within the structure which used to be limited because of the inherent characteristics of combination of photomicrography and etching process. Similarly, to work with mask-less procedures and eliminate use of expensive process like photo-lithography in structuring of graphene oxide nanosheets, Zhou et al. [131] have successfully demonstrated the use of laser etching techniques which are relatively fast and offers easy process control.

1.3.1.3 Stain etching

Furthermore, as discussed earlier, the fabrication of porous surface with minimum possible dimension is useful to enhance sensing characteristics up to some extent. Marrero et al. [132] have stain etched silicon surface using combination of hydrofluoric acid (HF), nitric acid (HNO_3) for solar cell fabrication which has surface texture with scale of μm. The surface achieved low reflectivity of 5% at spectrum wavelength range of 500-1000 nm. Anti-reflective nature of surface can be quite useful in several sensing applications like determination of relative position of the sun using micro sun sensor which employs anti-reflective surface [127]. Table 1.4 shows the structural topology achieved with various etching approach and their reflectivity along with the effective spectrum range. Furthermore, Sapelkin et al. [133] have used stain etching with combination of HF, HNO_3 and fluoroboric acid (HBF_4) to fabricate porous silicon for their studies of potential cell culturing and biocompatibility with porous silicon. The porous surface prepared with the stain etching had pore size varying from 50 to 100 nm. In experiments, the treated surface was proven to be much more compatible with cell adhesion with respect to untreated surface. The positive biocompatibility of a sensing surface can facilitate easy in-vivo sensor employment [134]. For further modification, instead of using HF based acid for etching, Becker et al. [135] used galvanic etching technique to fabricate porous silicon with successful fabrication of nano pores with the size below 3 nm.

With all these possibilities of being beneficial for sensor fabrication, stain etching also offers few difficulties. For instance, there is an incubation period associated with the formation of porous silicon when it is immersed in wafer etching solution which then followed by bubble formation with poor reproducibility and difficult layer generation control [139]. Additionally, the corrosive constituents associated with HF can be harmful to prefabricated patterns made with materials like silver and gold. For example, stain etching with HF decays silver contacts on substrate surface lowering the solar cell fill factor in case of solar cell surface fabrication [140].

Sensor Information	[136]	[137]	[132]	[138]
Etching Type	Plasma etching with SF_6 and O_2	Wet etching using Tetra-methyl ammonium (TMAH)	Stain etched with HNO_3 and HF with deposition of SIN_X using PECVD*	Wet Etching with HF and H_2O_2
Surface structure	Non-structured pyramids $\approx$ 200 nm	Non-structured pyramids $5 - 10$ μm	Dispersed non-structured pyramids $1 - 2$ μm	Dispersed structured pyramids $200 - 500$ nm
Reflectivity	13.3%	13%	Below 5%	3%
Effective spectrum range for optimum reflectivity	$300 - 1200$ nm	$350 - 1100$ nm	$500 - 1000$ nm	$300 - 900$ nm

*Plasma Enhanced Chemical Vapor Deposition

Table 1.4: Different etching approaches for fabrication of solar cell surface (Silicon $< 100 >$) with different surface texture and reflectivity.

Also, it is difficult to control the pore size resulting in diverse but relatively small range of dimension which might be a hindrance in applicability and versatility of the approach for sensing surface fabrication [141]. The controllable fabrication of porous silicon structure is possible by using nano and femto second laser by employing ablation process as it has been already proved through studies [142–144].

1.3.2 Material deposition

Physical vapor deposition (PVD), chemical vapor deposition (CVD) and atomic layer deposition (ALD) are the most commonly used material deposition methods for fabrication of nano and micro structured surfaces. Thin film generation is the most common application of these approaches and mostly they are combined with other micro-nano manufacturing processes for patterning of nano structure [145–147]. It is possible to achieve several surface characteristics and

conditions using these deposition methods. One of the major application is to enhance the suitability of surface by fusing it with nano particles or coating for enhancement of surface durability such as for life span improvement of battery electrode [148, 149]. The enhancement in battery life span can facilitate easy in-vivo sensor employment [150, 151]. In addition, it is also used for stacking of extremely thin layers of material over surfaces with large area [150]. Potentially, thin film deposition techniques can facilitate easy mass production of the sensing surfaces [152, 153]. Moreover, possibility to work at micro and nano level makes it useful for generation of composite materials like silicon nano fibers sputtered or coated with gold particles to enhance electrical conductivity and biocompatibility which can ease in-vivo sensor applications with enhanced performance [91, 92].

1.3.2.1 Physical vapor deposition

Sputtering

Physical vapor deposition is done mainly by using two different approaches namely sputtering and evaporation. Sputtering involves two step process, namely, sputter emission or erosion and deposition. Erosion of target surface happens by particle bombardment followed by deposition of sputtered material on a substrate. The technique generates thin film layer over a substrate. For example, deposition of ZnO nanobelts by Radio Frequency (RF) sputtering onto a copper tube for ethanol sensing [154]. As discussed before, use of porous surface is quite normal in gas sensing applications. In 1995, Sberveglieri et al. [155] presented the possible use of tungsten trioxide (WO_3) for detection of NO_x gases. Leading approach towards sophistication, Kim et al. [156] fabricated WO_3 thin films for NO_x gas sensing using DC reactive sputtering, which had particles with the size less than 100 nm, achieving detection limit as low as 5 ppm with relatively good sensitivity. Similarly, to achieve wide but lower optimum operating temperature range, Zeng et al. [157] used DC magnetron sputtering technique forming porous surface with pore size of about 9.3 nm which had optimum working temperature range of $100 - 250$ ℃ and

Change in sensing surface characteristics	**Parameter Varied in fabrication process**	**Sensitivity**	**Ref.**
Effective surface area from 2.6 m^2/g to 19.1 m^2/g	Discharge gas pressure respectively from 0.4 Pa to 12 Pa	$@^{ot*}$ 200 ℃ and 1 ppm of NO_2 $[(R_g - R_a)/R_a]^{\bullet}$ Increased from ≈ 50 to 450	[159]
Change in density of deposited layer from 7.39 g/cm^2 to 5.09 g/cm^2	Discharge gas pressure respectively from 1.3 Pa to 10 Pa	$[R_g/R_a]^{\bullet}$ Increased from ≈ 20 to 77	[158]
Doping of sensing surface with noble materials @ 0.2 at%, Deposition @ 1.3 pa-room temperature and surface annealed @ 873 k	Gold (Au) Doped	≈ 20	
	Pure WO_3	$\approx 7 - 9$	
	Platinum (Pt) Doped	≈ 3	
	Ruthenium (Ru) Doped	≈ 2	
Varying crystalline structure with annealing temperature	Annealing done @ 350 ℃	$@^{ot*}$ 300 ℃ $[R_g/R_a]^{\bullet}$ ≈ 11	[160]
	Annealing done @ 400 ℃	$@^{ot*}$ 300 ℃ ≈ 15	
	Annealing done @ 450 ℃	$@^{ot*}$ 300 ℃ ≈ 20	

• R_a and R_g are the electrical resistances before and after the introduction of NO_x, respectively.
• $@^{ot*}$ = at the operating temperature of

Table 1.5: Change in sensitivity of WO_3 based NO_x detection sensor with respect to sensing surface characteristics

it could detect upto 1 ppm concentration of NO_x. With sputtering, for the case of WO_3 based NO_x sensors, it is possible to manipulate the sensing surface conditions by controlling density of the deposited film, surface area and associated annealing process resulting in a strong possibility to get optimum performance [158–160]. Table 1.5 provides insights on change in sensing characteristics of WO_3 based NO_x sensors with respect to mentioned parameters.

Despite having enormous use in different applications, sputtering presents some

challenges as well. With magneto sputtering, target surface exhibits non-homogeneous electron charge distribution because of the electron trapped in magnetic field contributing to a difficulty in thickness control. In addition, target material utilized for deposition is less than 30%; rest of the material is normally deposited on unwanted surfaces and walls of used sputtering chamber [161]. Furthermore, the process deposits on areas other than substrate such as non-eroding target areas contributing to waste of expensive material. Also, the stabilization and control are quite difficult with hysteresis effect present in the operation [161]. Moreover, the control of surface texture and patterning are quite difficult with sputtering. For instance, generation of Cadmium Selenide (CdS) films using sputtering causes irregular grain size and rough surface which affect the performance of the sensor wherever it is employed and extra process of heat treatment will be necessary to overcome these problems [162]. Also, annealing of the sputtered films are difficult due to relatively high density [163]. Handling of reactive sputtering can be difficult with DC arc control as it forms insulating layers on the target surface along with the process which can have the charged up electric field that can result in breakdown. In addition, achieving stoichiometry films can be difficult due to possibility of poisoning of target surface [164]. In addition, the sputtering equipments in general are expensive and have slow deposition rate [165]. However, to fuse the material deposited using sputtering, laser ablation can be a useful approach as demonstrated by Hamnza et al. [92]. In addition, it is already proven that the laser ablation process, in general, provides better process control [166, 167].

E-beam evaporation

Instead of bombarding argon ions on the target, in evaporation, the vapor is generated by electron beam or heating of target in vacuum chamber which will be then deposited on the substrate surface. E-beam evaporation is often useful for deposition of nano-fibers and nanotubes for various applications including sensor fabrication [168–171]. Conventionally, due to high temperature deposition of the material and resulting undesirable material property, gas sensor manufactured us-

ing E-beam PVD exhibited poor response. But, modern approach of using nano particles and nanotubes to enhance surface characteristics is quite helpful. For example, as demonstrated by Wisitsoraat et al. [168], depending on the operating temperature, nanotube dispersed SnO_2 surface is 2 to 7 times more sensitive than pure SnO_2 surface. Also, the sensor is relatively two times faster in terms of recovery and response with relatively lower operating temperature. Similarly, Kolmakov et al. [172] have successfully used vapor deposition of Pd (Palladium) particles on nanowires and nanobelts to enhance gas sensing characteristics of SnO_2 based sensors. In addition, E-beam PVD allows thickness control which is really helpful to understand the sensor behavior associated with the coating thickness as demonstrated by Durrani et al. [173] in their experiments. Furthermore, considering recent needs and trends, it is important to miniaturize the sensor to make it feasible for real life use. McAlpine et al. [174] have used combination of various deposition techniques with E-beam PVD to generate Si-nanowire patterned flexible plastic surface that can be employed in wearable sensing devices exhibiting ppb (Parts Per Billion) level of sensitivity for NO_2 gas. Additionally, E-beam PVD process can achieve deposition rate at sub nano level (0.01 nm/s) enabling deposition of extremely thin layer over the substrate [175]. As discussed before, the trend to follow miniaturization with different combinations of sensor probe to get optimum sensing capabilities is also followed in the case of E-beam PVD. For example, over the years, by using material with high conductivity and porous surface, it is possible to fabricate SnO_2 based sensor which can detect C_2H_5OH at concentration of 1 ppm with high response (≈ 15 for $(R_a - R_g)/Rg$) [176]. The comparison of SnO_2 based sensors, manufactured using E-beam PVD, with various probe dimensions and their response for the sensing of C_2H_5OH (Ethanol) is shown in table 1.6.

It is common to notice that all of the evaporation techniques employs vacuum chamber for the deposition which helps to maintain the purity of a film and enables the evaporation at relatively low temperature. Contrary, employing a vac-

Ref.	[177]	[178]	[176]
Dopant/coating material	-	Ag Nano Cluster $5-50\ nm$	Unique dome structure with dual side Au coating with thickness of $\approx 2\ nm$
Probe dimension	SnO_2 Nanowires with $\approx \phi$ $100\ nm$	SnO_2 nanowires with ϕ $30-60\ nm$	Array of domes made of SnO_2 with wall thickness of $100\ nm$ and $\approx \phi\ 700\ nm$
C_2H_5OH **Concentration**	$100\ ppm$	$100\ ppm$	$50\ ppm$
Operating Temperature	500 ℃	450 ℃	300 ℃
Sensitivity	$(R_a/R_g) =$ 26.5	(R_a/R_g) ≈ 55	$(R_a - R_g)/R_g = 486.8$

Table 1.6: SnO_2 based sensor for C_2H_5OH detection fabricated using E-beam PVD

uum chamber can be really expensive and it can be the most costly equipment in whole PVD process [179, 180]. Additionally, due to poor selectivity, it can make the deposition of alloys difficult. Also the process itself by nature follows the line-of-sight trajectories for the deposition. Thus, without movement of substrate surface or proper geometry it is difficult to achieve homogeneous film thickness around the substrate. In addition, the process offers only few parameters to vary in order to achieve different surface properties [168, 181]. As the process employs relatively high temperature, it can be a problem for some materials as it will affect the surface condition of the deposited film. When PVD is used for formation of Thermal Barrier Coatings (TBCs), high temperature causes sintering of the coating resulting in unstable surface having higher thermal conductivity and Young's modulus [182]. The pulsed laser deposition (PLD) can be a useful approach to overcome some of the problems faced with PVD. It is possible to retain stoichiometry of the target surface with PLD process as it heats the local region instead of entire target thus it makes deposition of alloys easy. In addition, substrate achieves relatively low temperature making deposited surface more stable and also

PLD process facilitates easy handling as the laser is situated outside of the vacuum chamber [183]. Possibilities with the laser approach discussed in detail in the upcoming sections.

1.3.2.2 Chemical vapor deposition

Similar to PVD, CVD is also a very well known and widely used technique for thin layer generation in various applications. The acceptability of the CVD process can be because of scalability it offers or possibility of precise control and uniformity of deposited film [184, 185]. Also CVD is useful in several medical application as it offers thickness uniformity with no need of physical interaction. For instance, Carvalho et al. [186] have used CVD process for human tooth restoration purpose. Furthermore, for commercially fabricated nanotubes, CVD is the most popular and widely used among other methods like arc-discharge and laser ablation [187]. From the review, trend of miniaturization of sensor probes using CVD and its combination with other techniques can be noticed easily. For instance, Ghosh et al. [188] demonstrated the potential of spray and CVD deposited ZnO films doped with different noble metals like Pt (Platinum) and Pd were sensitivity towards hydrogen gas. Roy et al. [189] then fabricated a ZnO based sensor using CVD and concluded that the operating temperature plays significant role in achieving optimum sensitivity of the sensor. Also, sensitivity and optimum performance of their sensor was obtained around operating temperature of 400 ℃. Using the same approach, Barreca et al. [190] fabricated ZnO based sensor which employed 1D structure of nano assemblies which shown possibility to detect CO concentration up to 100 ppm with response time of 1 minute at relatively lower operating temperature of 200 ℃. Following the same methodology, Wang et al. [191] demonstrated that by employing nanorodes made of ZnO material with diameter ranging from $90 - 200$ nm and length of $1.7 - 2.1$ μm, it could function accurately for ethanol concentration of 50 ppm at the same operating temperature

Sensing application	Sensing probe geometry	Enhanced sensing characteristic	Comparison	Ref.
Humidity sensing	Graphene layer with thickness of 15 nm	30 ms response and recovery time	More than 33 times faster than conventional sensors with nanowires [192–194]	[195]
Glucose sensing	Graphene layer with thickness of 0.5 nm	Sensitive towards glucose concentration of 3.3-10.9 mM	Covers the full range of concentration of glucose required for medical diagnostics	[196]
Detection of DNA hybridization	Graphene channel of $45 \times 90 \mu m$ with 20 nm Cr and 100 nm Au layer on each graphene site	sensitivity as low as 100 fM	10 times lower detection limit than prior transferred CVD G-FET DNA sensors.	[197]
Strain sensing	Graphene mesh with scale of μm	≈ 50 mV current generation with 0.1% strain	For similar strain, $\approx$ 1.5 times of voltage signal generation than conventional ZnO nanowire based sensor	[198]
Ele-chemical Piezoelectric sensing	Theoretical graphene membrane thickness of 0.335 nm	Deflection of 202 nm with pressure difference of 477 $mbar$	20-100 times sensitive than conventional MEMS sensors	[199]

Table 1.7: Graphene based sensors fabricated using CVD which exhibits extraordinary sensing capabilities.

with the response time of just ≈ 37 s. Furthermore, as mentioned before, because of various possibilities with CVD, it has become very popular with generation of graphene for different sensing applications where extreme sensitivity is required. Table 1.7 enlist some of the sensors made with graphene using CVD which exhibit great suitability to the application and extraordinary sensitivity with compare to conventional sensors employing MEMS approach and nanowires.

With all the advantages, CVD offers few challenges as well. Traditional CVD

methods are time consuming and also expensive in terms of energy spent for the process [200]. In addition, CVD manufactured graphene field effect transistors can exhibit lower transconductance with fewer mobility carriers and high intrinsic resistance which forces researchers to use high k (dielectric constant) and ultra-thin dielectrics which make the process relatively more complicated [201]. As discussed before, use of a vacuum chamber for CVD process can increase the cost and complications. As certain CVD processes use high temperature, they cause stress in the substrate surface and deposited film itself [202]. The precursor used in the process can be highly toxic depending on the nature of process and in some cases, expensive if they are metal-organic [203]. Plasma enhanced CVD , a modified version of the CVD, also suffers from few drawbacks mainly, deposited film being unstable with aging and humid atmosphere, stress existence in the film, significant time consumption in several applications and costly equipment [204]. Some of the disadvantages can be overcome by using laser ablation and laser processing. For example, as demonstrated by Ye et al. [205], the synthesis of graphene is possible with laser processing which will potentially eliminate the use of toxic precursor and processing at elevated temperature. Table 1.8 shows summery of previously discussed general challenges offered by contemporary material deposition methods.

1.3.2.3 Atomic layer deposition

Same as conventional deposition methods, ALD method has its own challenges. Few of the major drawbacks of the approach are lower throughput and excessive time consumption as the growth per cycle can be order of Å [206, 207]. Same as CVD processes, the ALD also employs the precursor gases for the process which can be toxic in many cases [208]. However, there has been always attempts to use metal organic or non-toxic precursors to make the process safer and reduce the contamination [209–211]. Aside from all those limitations, ALD is becoming pop-

Method	Challenges
Sputtering	• Difficult to manage uniform deposition thickness with controlled porosity of thin film. • Less than 30% of actual target surface is used for deposition. • Deposition happens on unwanted equipment areas as well. • Control of surface texture is difficult. • Achieving stoichiometry of films is difficult. • Costly equipments and relatively slow deposition rate. • Deposited film may have high density with lower porosity which can be hindrance in several sensing applications.
Evaporation deposition	• Vacuum chamber involved in the process makes it expensive. • Deposition of alloys can be difficult due to inherent nature of poor selectivity. • Thickness homogeneity over the substrate is difficult on fixed surface due to line of sight trajectories followed by the process. • Deposition at high temperature can affect the surface stability. • Offers very few parameter to vary the deposited surface characteristics.
Chemical vapor deposition	• If employed, vacuum chamber involved in the process makes it expensive. • The precursor gas used in the process can be highly toxic and non-environment friendly. • Use of metal organic gas as a precursor can be expensive. • In case of alloys with different thermal expansion coefficient, deposition at high temperature can affect the surface stability and induce stresses. • The process can be time consuming in some cases. For example, deposition of super lattice structures.

Table 1.8: General challenges offered by contemporary material deposition methods.

ular because of its precise process and thickness control capabilities and excellent self limiting characteristics [212–214]. Considering all these advantages that can be gained, it is quite common to see wide use for sensing surface coating with ALD and combining it with other techniques [215–217]. One of the major application of the ALD is to enhance the performance of existing surface conditions by coating of various materials. For example, Lotfabad et al. [218] have used ALD process to coat TiO_2 on silicon nanowires to enhance the cyclic stability and coulombic efficiency of lithium ion battery which can be beneficial for in-vivo sensor applications. Similarly, Feng et al. [219] have used ALD process to coat Pd nano particles with alumina to prevent sintering and enhance stability at higher temperature. Following the same approach, Liu et al. [220] have coated semiconductor electrodes with passivation layers to enhance the water-splitting performance for better hydrogen extraction from water source. In addition, ALD process may be used for the enhancement of electrical performance of silicon nanowires by coating it with material with higher electrical conductivity. Considering all these possibilities, it is safe to say that ALD can be a huge advantage for sensing performance enhancement by modifying surfaces with coatings.

Overall, discussion in this section includes advantage and limitations offered by various manufacturing methods for fabrication of nano structured sensing surfaces along with their effect on sensors' performance. Many of the limitations can be overcome by simply employing inexpensive laser ablation process. Furthermore, basic functioning of the laser processing and its potential to be used for sensing surface fabrication with research possibilities and current works are discussed in the following section.

1.4 Laser ablation and laser processing

The approach of laser ablation for nano fabrication was first reported by Morales et al. [221]. Since then, for nano-micro fabrication, laser is used for manufacturing of porous film and particles made of materials like titanium, tantalum, carbon,

silicon and many other non metallic materials [222–226]. Porous surfaces made with various materials are used in many sensing applications. For example, porous silicon for vapor and optical sensing, porous zinc oxide for gas sensing, and porous titanium dioxide for humidity sensing [227–230].

Furthermore, specific studies of porous titanium and silicon using laser ablation can be seen on significant surge. The growing interest in porous titanium can be because of the biocompatibility and its wide spread use in biomedical field for implant fabrication. Additionally, years of available experience with titanium in biomedical field can help to comprehend suitability in terms of nano-bio research and development [231–234]. Similarly, silicon has been widely accepted in semiconductor industry since decades ago helping researchers to understand its behavior through years of available research. Abundance of silicon material on the earth made it a promising candidate for future research.

1.4.1 Laser ablation : Process control

Ultrashort laser pulses employ unconventional melting phenomenon to process the surface. Tom et al. [235] indicated in their study that top layer ($\approx$ 100 Å) of silicon crystals distorted in 150 fs after the surface was excited by 100 fs laser pulse. This study then supported by Stampfli et al. [236] who demonstrated that silicon lattice structure destroyed within 100 fs of time once the electron hole plasma was created. The time of distortion was quite shorter than time needed for crystals to melt in conventional fashion. Later on, in another study, Stampfli et al. [237] concluded that laser induced energy causes the excitation of electron with higher extent than its stable limit resulting in atoms having enough energy to destroy structure and rapidly melt it in much shorter time than conventional melting. In other words, femtosecond laser ablation provides melting without any phase transformation at the focal point resulting in a local heating instead of bulk heating which provides better control over target properties.

The picosecond and nanosecond laser may have extremely small melt pool at

the focal point because of relatively larger pulse duration. These laser characteristics can provide uniform surface property to achieve homogeneous sensing behavior in application such as gas detection. Additionally, laser ablation induced nano particles provide good stability which might be helpful to achieve longer useful lifespan for sensors [238, 239]. As mentioned, instead of conventional heating which involves phase transformation, laser ablation with controlled parameters interacts with the electron of the surface material which then followed by conventional heating in nearby regions [240]. The concentrated laser provides power at the scale of GW/cm^2. The produced plasma creates its own controlled environment within the laser spot which induces a surface breakout through multi step behavior creating a shock wave [241, 242]. Figure 1.1 depicts the formation of nanofibrous structure caused by plum expansion for silicon substrate.

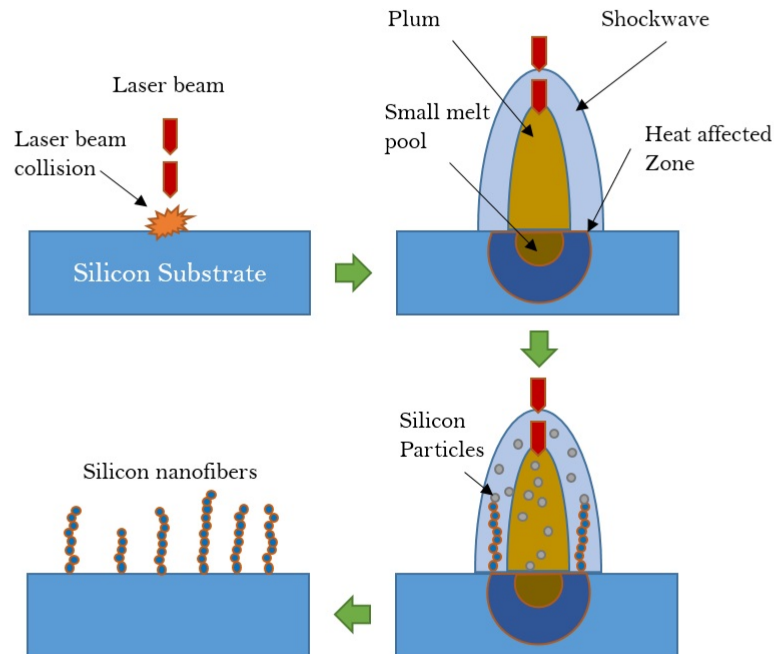

Figure 1.1: Nanofiber generation on silicon substrate using laser ablation

In other words, the electromagnetic energy and momentum transfered from laser beam to surface eject the electrons causing temperature rise and resulting in formation of ionized gas (plasma) which expands like shock-wave around substrate surface being processed. The continues process causes accumulation of energy which overtakes the ablation threshold of the material resulting in removal

of surface particles. Plasma, after the formation of small melt pool at focal point, contains mixture of ions, electrons, and nanoparticles. In ambient air, plum core is hot compared to expanded plum causing particles to move towards relatively cooler region. Hence, lower temperature in such region causes nucleation and crystallization of accumulated solid structure [243]. The solidified particles are formed by aggregate-aggregate and atom-aggregate attachments [244]. The resulting structure can have particles or mesh-like geometry with nano level which cab be recognized as nanofibrous structures [243].

1.4.2 Advantages of laser approach

Localized heating in case of laser ablation can reduce the stability problem as overall substrate is maintained at relatively lower temperature [91]. The fabrication of nanowires and processing is possible at ambient condition as demonstrated by Colpitts et al. [245]. The elimination of vacuum chamber for nano processing makes the approach relatively cost effective than any other conventional deposition method discussed earlier. In addition, the process provides number of parameters like laser frequency, power, scanning speed and patterning methodology to alter the porosity and diameter of the nanowires. Also, in laser processing, laser beam relieves energy on a material surface in the form of very strong but short pulses as explained in section 1.4.1 which creates localized heating in very small region instead of bulk material uniform temperature elevation eliminating the possible effect on crystalline structure or bulk material properties. Furthermore, altering surface topology with conventional methods can be extremely expensive. During photo-lithography process, changing a pattern requires different photo-mask costing upto $100k each because of complicated fabrication process [142]. Instead of using expensive photo-mask patterning at micro level, it is also possible to use laser induced silicon amorphous patterned layer as etch stop as demonstrated by Kiani et al. [142]. Later, they demonstrated the control of pattern width by varying laser pulse duration and number of pulses [143]. In addition, all conventional nano and

micro fabrication techniques involve some kind of gas for which leak proof enclosed cabinet is a necessary increasing overall cost and possibility of environmental contamination or toxicity if hazardous precursors are being used. Laser processing done for nano or micro fabrication does not need any precursors as can be seen in many studies [221, 246–248]. Furthermore, laser processing also facilitates inherent pulse width variation with nano-second, pico-second and femto-second laser for divers possibilities.

1.4.3 Possibilities with laser ablation

To the best of our knowledge, only few groups have done study on control and effect of laser ablation parameters. Kiani and his research group [91, 92, 143] have studied the effect of laser processing parameters like power, various combinations of laser power and frequencies, scanning overloop and line spacing on patterned surface characteristics like pattern width, size of particles, conductivity of porous nanowires, doping concentration and diameter of nanowires. Similarly, Tull et al. [153] have demonstrated the possibility of variation in silicon surface morphologies using variation in a number of femtosecond laser pulses for a specific pulse duration. The variation in process demonstrated formation of defined array of irrupted silicon pillars as the number of femtosecond pulses increased from 100 to 600 with the pulse duration of 100 fs. In the same way, Kuzmin et al. [249] have used different pulse duration of femtosecond laser to control the nano particles made of silicon processed while submerged in ethanol. They varied pulse duration from 35-900 fs which resulted in nanoparticles with different size varying from few nano meters to 200 nm. Table 1.9 depicts the summery of these studies for porous silicon substrate.

Considering all ease of process and freedom of changing operating parameters, combination of laser ablation with other modern techniques can be a promising approach to fabricate sensing surface with various desirable characteristics. Hamza et al. [92] have used sputtering method to deposit gold particles on the porous

Laser System	Laser parameter varied	Effect on topology	Ref.
Diode-pumped and Yb-doped femtosecond laser system with laser spot ϕ 10.4 μm	Combination of power (94.8-6.25 W) and frequency (8-26 MHz)	Pattern width variation 5.80 − 4.05 μm @ scanning speed of 100 m/s	[143]
Nd:YAG nanosecond laser with laser spot ϕ 20 μm	Laser power 2.35-9 W @ condition 1	Average silicon particle size ≈ 4-14 nm @ 5 overlap config.	[91]
Nd:YAG nanosecond laser with laser spot ϕ 20 μm	1-5 overloop config. @ condition 1	Average fiber diameter ≈ 75-125 nm @ Power-12 W	[92]
Femtosecond laser with laser spot ϕ 150 μm (SF_6 atmosphere @ 67 kPa)	Number of laser pulses 100-600 @ 100 fs pulse duration, 800 nm wavelength, Laser fluence of 8 KJ/m^2, frequency of 1 kHz	Bulk rough surface to Surface having array of erupted pillars	[153]
Nd:YAG nanosecond laser with laser spot ϕ 20 μm	1-5 overloop config. @ 2.35 W and condition 1	Conductivity (Siemens/cm) ≈ 0.75-1.25	[91]
femtosecond laser system (Spectra-Physics Spitfire Pro) with gaussian beam diameter of 12 mm (at the $1/e^2$ level)	Pulse duration of 35 to 900 fs @ 800 nm wavelength, frequency of 1 kHz, Laser fluence of 4 KJ/m^2, 10 min exposure	Silicon nano particle with diameter less than 3 nm to 200 nm (Silicon immersed in a 95% ethanol)	[249]
Nd:YAG nanosecond laser with laser spot ϕ 20 μm	9-2.5 W @ 0.025 mm leading @ condition 1	Gold concentration in laser processed gold sputtered silicon film 2-5.2 %	[91]

Condition 1 : 0.025 mm leading distance, scanning speed of 100 mm/s and frequency of 100 kHz.

Table 1.9: Topology change on porous silicon with respect to various laser process parameters.

silicon substrate fabricated by laser processing which provided relatively higher conductivity due to fused gold nano particles available in porous structure which might be useful to enhance performance of the sensor employing silicon sensing surface. Furthermore, according to a study done by Powell et al. [250], porous silicon fabricated using femtosecond laser exhibits surface enhanced Raman scattering

(SERS) activity which can be significant for nano-Raman sensing applications. The method recommends use of Rhodamine 6G (R6G) and CrystalViolet(CV) chemical dyes to get maximum enhancement factor at the order of 10^6 with respect to bulk silicon to measure the weak and scattered signal. Enhancement factor for SERS devices defined as EF = $((I_{NS}/N_{NS})/(I_{sub}/N_{sub}))$. Where, I_{NS} and I_{sub} are intensities of Raman signal from the nano web structure and from the substrate while N_{NS} and N_{sub} are number of molecules contributing to the Raman signal from nano web structure and from the substrate. Later, Powell et al. [251] fused silicon amorphous structure with gold nano particles which further improved the enhancement factor by 10 times relative to pure silicon porous structure. In addition, they used similar approach by doping silicon nanocore structure with Au and AuPd for the detection of biomolecule L-glutathione (GSH). The approach improved enhancement factor by almost 100 times with respect to pure silicon nanocore structure for L-glutathione detection [252]. Similarly, using laser ablation, Sima et al. [243] have controlled porosity of alumina coated with cerium stabilized zirconium dioxide doped hydroxyapatite to enhance bioreactivity and biocompatibility which can contribute to porous silicon surface adaptability for in-vivo sensing application. Noticeably, it can be a promising approach to use atomic layer deposition with laser ablation to coat laser fabricated nanowires with various material by controlling thickness at atomic level or to chemically modify the nanoporous surface to explore sensing possibilities with new approach as demonstrated by Makra et al. [253]. Overall, modified silicon sensing surfaces may have better properties in terms of conductivity, biocompatibility or film stability depending on the modification approach, coating material and coat thickness resulting in a sensor having better sensing characteristics.

1.4.4 Research objectives

As discussed in previous section, importance of nano and micro structured surface for the sensing purpose are immense. Various techniques being used for the fab-

rication may offer significant advantages and limitations depending on numerous parameters. However, latest approach of laser ablation could be an inexpensive and simple method to fabricate such sensing surface. The fabrication of silicon nano fibrous structure with laser ablation has already been proven in recent studies done by A. Kiani and his research group [91,92]. Hence, considering possibilities of providing large surface area with nano particles and nano fibers, its potential to be used as a sensing surface along with its characteristics of being biocompatible and abundance of silicon material on planet earth, makes it a viable candidate for being used as a sensing surface [227, 228, 245]. In addition, to the best of our knowledge, until now, there has been few studies (discussed in the Table 1.9) to comprehend porous silicon surface morphology produced with varying laser parameters. However, variation in electrical properties of such porous silicon with different laser parameters are yet to be understood. Considering advantages offered by relatively inexpensive and simple approach of laser ablation, for porous silicon to be used as a sensing surface, it is essential to understand the effect of laser ablation with various parameters on electrical properties along with variation in surface topology. Study of such electrical behavior offered by porous silicon can enable the estimation of required transducers and similar electrical components to employ it as a sensing surface.

As mentioned, there are number of laser parameters such as frequency, pulsation width, power, scanning speed, number of loops and leading distance available for the process variation. Here, leading (L) is the distance between two consecutive scan processed on specimen during laser plasma processing and number of scanning loop is the count of laser passed through same ablated surface. For instance, 3 NL would mean laser beam has passed 3 times over the same surface. Such parameters might have their own way to affect the ablation process. As an example, increasing power simply increases the energy supplied to a specific spot per unit time. However, changing pulsation width with same power value can affect the way energy delivered on the same surface. Similarly, other mentioned scanning

parameters also affects the energy delivered per unit area per unit time.

In addition, considering increasing use of silicon as a sensing surface, parameters like scanning speed, number of scanning loops and leading distance can affect the rate of the production directly which can cause significant financial impact to the manufacturer. To fabricate HNfSi on 10 mm$\times$10 mm silicon surface with leading of 0.05 mm and scanning speed of 100 mm/s, the processing time required would be $\approx$ 20 sec. Also, if leading is decreased to 0.025 mm with same scanning speed, the total processing time would increase to $\approx$ 40 sec. Similar effect can be seen with variation in scanning speed and number of loops as well. Moreover, parameters like laser power directly relate to the power consumptions which could affect financial aspect of manufacturing as well as its direct or indirect involvement with preservation of environment. Considering feasibility of use of porous silicon as a sensing surface, associated topological features and its diverse resistive behavior, it is vital to understand the effect of all the control parameters involved with laser processing.

The main objective of the carried out studies are listed as follows:

- Determine the feasibility of generating Hybrid Nano-Fibrous Si/SiO_2 structure (HNfSi) consisting only nanofibers, only nano-particles and hybrid structure containing both nano-particles and nanofibers using a ultrashort (picosecond/nanosecond) pulsed laser.

- Investigate the effects of various laser parameters e.g. frequency, power, pulsation width, number of loops and leading distance on topology, material and optical properties of HNfSi.

- Understanding the effects of laser parameters on bulk electrical resistivity offered by HNfSi having diverse nano constituents.

- Study of thickness based resistive behavior offered by HNfSi consisting various form of nanostructure formed with variation in ablation temperature and direct laser processing overlap.

Chapter 2

Materials and methods

As discussed in the previous section, for this study, it was decided to use nano/pico second laser ablation for the generation of micro/nano structured sensing surface. Furthermore, Ytterbium laser was employed along with required optics and computer controlled 2D scanner to focus and pattern the silicon surface. Various methods, used for further analysis of resistive, optical, material and topological characteristics of generated sensing surface, are discussed in this chapter along with equipment and software used for accurate results.

2.1 Optical design/setup & laser

The schematic diagram of setup used for laser plasma processing of silicon surface can be seen in Figure 2.1. Ytterbium discontinues fiber laser (IPG Laser Model : YLPP-1-150V-30) along with wavelength of 1064 nm was employed for laser plasma processing of n-type silicon $< 100 >$ wafer. Initial laser diameter of 7.6 mm was reduced to final theoretical spot diameter of ≈ 29 μm. To achieve such focused laser spot, iris diaphragm along with two axis galvo scanner mirror (JD2208 by Sino-Galvo) with the help of F-theta lens having focal length of 63.5 mm were employed. Laser parameters like frequency, power, pulsation width, laser processing speed, leading distance were set to, 1200 kHz, 15 W, 150 ps, 100 mm/s and 0.025 mm respectively along with 1 scanning loop unless varied. In addition, more than one

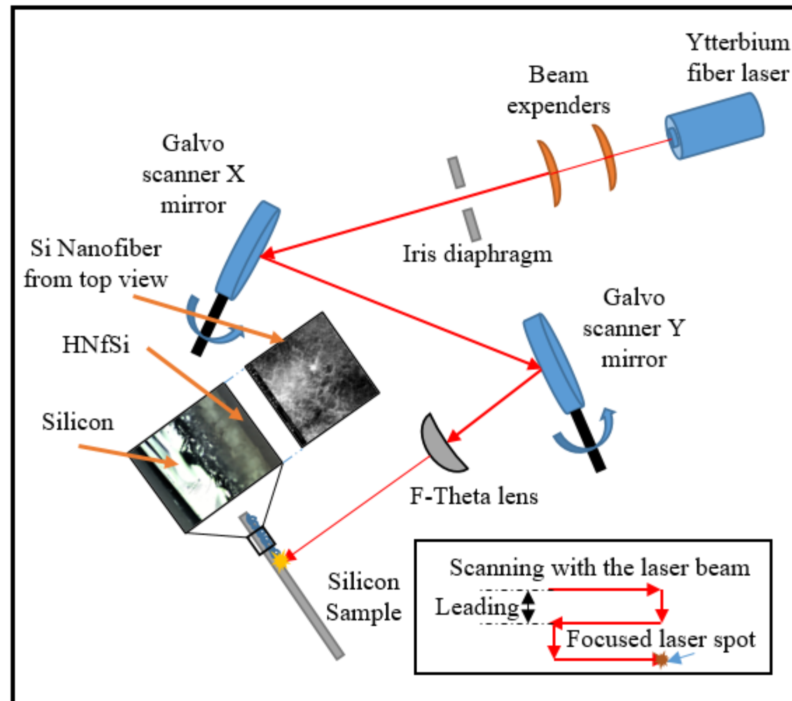

Figure 2.1: Experimental setup for HNfSi fabrication.

set of similar samples were generated to maintain integrity of the results gained through various surface characterization and resistivity tests.

2.2 Resistivity measurements

2.2.1 4-point probe

4-Point probe (NAPSON Corporation TC - 150u - 100g) was used to measure direct bulk resistivity of prepared samples. It was measured on 5 different and random locations on each sample to compensate any deviations in homogeneity of ablated surface.

2.2.2 Parallel plate electrode configuration

Schematic diagram of parallel plate electrode configuration used for resistivity measurement with the help of Keithley 2001 is shown in Figure 2.2. Because the electrical resistivity offered by prepared samples is significantly higher than the

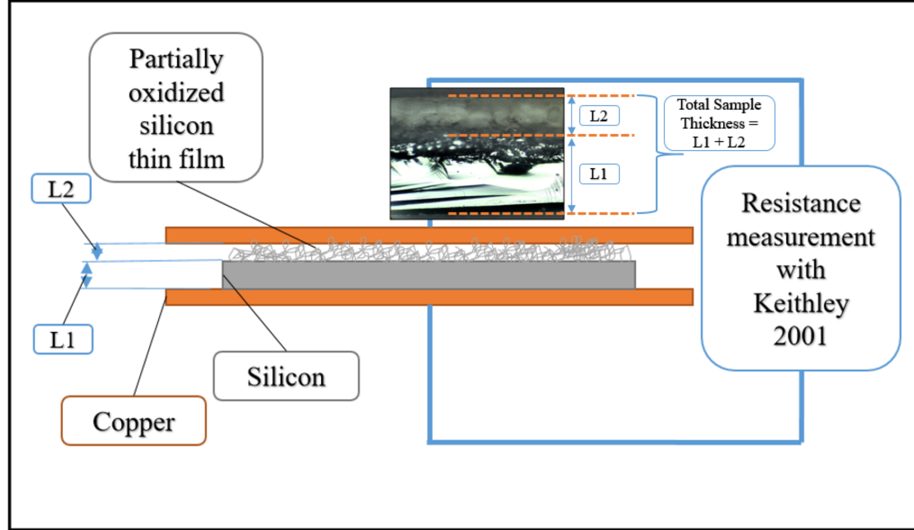

Figure 2.2: Parallel plate electrode configuration for thickness based resistive characterization of HNfSi.

same possessed by measuring system, any system resistance was avoided during the calculations. Furthermore, as shown in Figure 2.2, L2 is identified as average thickness of HNfSi (i.e T(HNfSi)) and L1 is an average thickness of left over silicon underneath the generated HNfSi. Furthermore, thickness of HNfSi measured with the help of ImageJ analysis and vernier micrometer was applied to calculate thickness based resistance. In addition, for the simplicity, resistance offered by heat affected zone on the processed surface considered to be the same as a silicon wafer.

2.3 Dimensional analysis of HNfSi

Optical microscope (Leitz laborlux 12 me) was used to capture the cross section of processed silicon with HNfSi produced on it. ImageJ software (v 1.501 by Wayne Rasband at the National Institutes of Health, USA.) was employed to measure the HNfSi thickness ($L2$ in Figure 2.2) on the processed silicon. To set the scale during ImageJ analysis, overall thickness ($L1+L2$ in Figure 2.2) of processed silicon including HNfSi was referred which was measured with high precision Mitutoyo digital vernier micro meter (Model MDH-25M with least count of 0.0001 mm or 0.1

μm). In addition, ImageJ analysis was also employed to analyze Scanning Electron Microscope (SEM) images of HNfSi to comprehend its geometrical characteristics like fiber diameter and fibrous density.

For the integrity of fibrous diameter values, clearer SEM image out of two high resolution images with magnification of 50,000X and 10,000X was referred. In each case, fiber diameter is an average diameter value obtained from 60 randomly spread spots in the same SEM image. In addition, fibrous density was calculated using black and white image threshold feature in the ImageJ analysis where relatively black pixels could be counted as a void and white pixels as a presence of fibrous structure. However, such qualitative measurement may change with deviation of few percent as it relies on individual judgment. Considering such factors, for all the measurements done using ImageJ analysis, basic error of 5% is assumed.

2.4 Surface Characterization : SEM, Energy dispersive X-ray (EDX) and Raman spectroscopy

To enable advanced topological study of HNfSi, Quanta 3D 200/600 scanning electron microscope was employed. In addition, EDX (Equipment used : EDAX Genesis 4000 energy dispersive X-ray system) and Raman spectroscopy tests (Equipment used : Renishaw Raman Imaging Microscope System 2000) was used for the detection of relative oxidization level and to confirm the respective concentration of silicon and oxygen present on HNfSi.

2.5 Light spectroscopy

To analyze the reflective characteristics of the HNfSi, light spectroscopy for visible spectrum range was done using Ocean Optics USB 2000+ along with the help of full possible light intensity provided by Fiber-Lite MI-150. In addition, all of the data was processed and extracted using Spectrasuit software.

2.6 Statistical analysis

For reliable data analysis, Microsoft Excel 2016 and Matlab R2018a was used. As stated before, for ImageJ analysis, 5% of error is assumed for geometrical measurements done using SEM images. Furthermore, error bar presented in all of the graph represents possible one standard deviation in measured quantity. To analyze the significant difference between means, 95% of confidence level was applied to One Way Anova analysis with one factor. In addition, wherever noticed, the lack of significant difference between respective means is discussed in further explanation.

Chapter 3

Theoretical background

As mentioned earlier, laser setup employed for the study facilitates variation of important laser parameters like frequency, power, pulsation width along with numerous scanning parameters like scanning speed, loop and leading distance. However, laser parameters may have significant effect on fabricated topology considering its effect on the way the heat transfer takes place during the ablation process. Alteration in such laser parameters changes the deposition sequence and ablation intensity affecting resulting structure's morphology significantly. Hence, possible theoretical effect of various laser parameters on ablation temperature is studied along with theoretical background needed to analyze the resistance offered by generated HNfSi using various resistance measuring methods. In addition, for efficient sensing performance, requirement of theoretical minimum fiber diameter was studied.

3.1 Temperature generation with laser ablation

Although, ablation process is immensely complex; assuming conventional mode of heat transfer with all the available laser parameters, it is possible to obtain some insight on the probable effect on ablation temperature with its variation. For application of conventional heat transfer model with Gaussian profile of the laser beam, use of cylindrical coordinates is essential. One dimensional heat flow

using cylindrical coordinates can be described as below.

$$\left[\frac{\partial^2 t}{\partial r^2} + \frac{1}{r}.\frac{\partial t}{\partial r} + \frac{1}{r^2}.\frac{\partial^2 t}{\partial \phi^2} + \frac{\partial t^2}{\partial z^2}\right] k + \frac{q_g k}{K} = \frac{\partial t}{\partial \tau} \tag{3.1}$$

In equation 3.1, r, ϕ and z depicts cylindrical coordinates. In addition, k(thermal diffusivity) and K (thermal conductivity) are assigned specified characteristics for the material of interest. However, due to no internal heat generation along with assumption of complete homogeneity of processed silicon, dependency on coordinate ϕ will be eliminated as well as internal heat generation rate q_g would be zero. Hence equation 3.1 can be modified as below,

$$\left[\frac{\partial^2 t}{\partial r^2} + \frac{1}{r}.\frac{\partial t}{\partial r} + \frac{\partial t^2}{\partial z^2}\right] k = \frac{\partial t}{\partial \tau} \tag{3.2}$$

However, such equation presents simpler heat flow behavior along the axis parallel to incident angle. Considering reduction in laser power with increasing depth, the behavior of temperature might not be linear along the progressive distance. To mimic the laser processing on a material block, considering Gaussian profile of the laser beam, these equation was further modified into two dimensional heat flow equation for a ring heat source by Carslaw et al. [254, 255]. Such equation can be described as below,

$$T_{r,z,\tau} = \frac{Q}{4\rho c(\pi k\tau)^{3/2}} exp\left[\frac{-r^2 - r'^2 - z^2}{4k\tau}\right] I_0\left(\frac{rr'}{2k\tau}\right) \tag{3.3}$$

In this equation, k,ρ and c represent, in order, thermal diffusivity, density and specific heat of the material of interest. Q is the total heat deposited on material being processed and r' is the radius of a corresponding ring. In addition, I_0 denotes the modified Bessel function. Using equation 3.3 along with Laplace transformation and integration of Gaussian profile with radius d, John Ready [255] introduced equation suitable for prediction of temperature profile for noncontinuous laser. Furthermore, Hendow et al. [256] presented the same equation with

modification for temporal pulse profile longer than 10 ns as shown below,

$$\Delta T(r,z,\tau) = \frac{I_{max}\gamma\sqrt{k}}{\sqrt{\pi}K}\int_0^{\tau} \frac{1}{\sqrt{t}\left[1+\frac{8kt}{W^2}\right]} e^{-1\left[\frac{z^2}{4kt}+\frac{r^2}{4kt+\frac{1}{2}W^2}\right]} dt \quad (3.4)$$

In equation 3.4, peak intensity is the ratio of power and laser spot area. So, intensity is calculated as $I_{max} = (4P_{measured})/(\pi d^2 f \tau)$. In addition, f is the laser pulse frequency, $P_{measured}$ is the laser power, k is the diffusivity of the material, K is the conductivity of the material, γ is the fraction of pulse energy absorbed by material, τ is the laser pulsation width, z is the plasma ionization depth, r is the radius of laser spot diameter with respect to center of plasma ionization, and W is the value of beam's field radius ($1/e$). In our study, pulse width are specified within four steps, namely, 150 ps, 1 ns, 2 ns and 5 ns. It is important to note that equation 3.4 is used only for primary judgment of the effect of important laser parameters assuming completely typical heat transfer taking place even with pulsation width lower than 10 ns.

3.2 Resistivity measurements

3.2.1 Four point probe

Four point probe was employed to measure the resistivity for porous silicon prepared with variation in frequency, power and scanning loops. Regular setup for the four point probe can be seen in Figure 3.1. When the distance between all four probes considered to be same (i.e S1 = S2 = S3 = S = 1 mm), for the large area, resistivity of the surface (ρ) would be [257],

$$\rho_0 = \frac{V}{I} 2\pi S \times F\left(\frac{l}{S}\right) \quad (3.5)$$

In equation 3.5, V is the measured voltage, I is the current, S is the distance

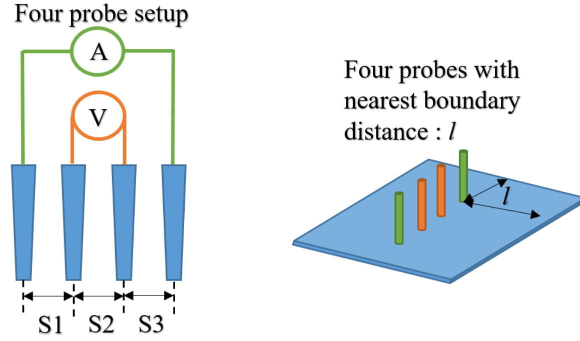

Figure 3.1: Four point probe for thin film resistance measurement.

between two consecutive probes, and l is the minimum possible distance of any of four probe from the boundary of sample. Here, the ratio $F(l/S)$ is a correction factor considering the fabricated thin film with finite area. Considering available ratio of $l/S > 3$ in carried experiments, for any configuration involving electrodes parallel or perpendicular to boundary with it being conductive or non conductive boundaries, the correction factor could be considered $F(l/S) \approx 1$ [257]. Hence, considering our interest in relative resistivity measurements and larger area of the thin film relative to probe size and distance between probes, the thin films can be considered large enough to employ simple concept with equation 3.5 for resistivity measurement. Considering our interest in characterizing silicon wafer with porous thin film fabricated on it as a whole, unclear boundary conditions between pure silicon, heat affected zone and nanostructured silicon; relative comparison of resistivity was taken into account.

3.2.2 Parallel electrode configuration

Using 4 point probe, it was possible to measure bulk resistivity of the fabricated HNfSi. However, in order to measure thickness based resistivity of just the fibrous structure, parallel electrode configuration was used. As shown in Figure 3.2, fabricated HNfSi along with silicon wafer was placed between two copper electrode connected to the resistivity measuring setup. Resistance offered by such setup was measured to be $\approx 6\ \Omega$. Such resistance was simply ignored considering very high

resistive properties of HNfSi.

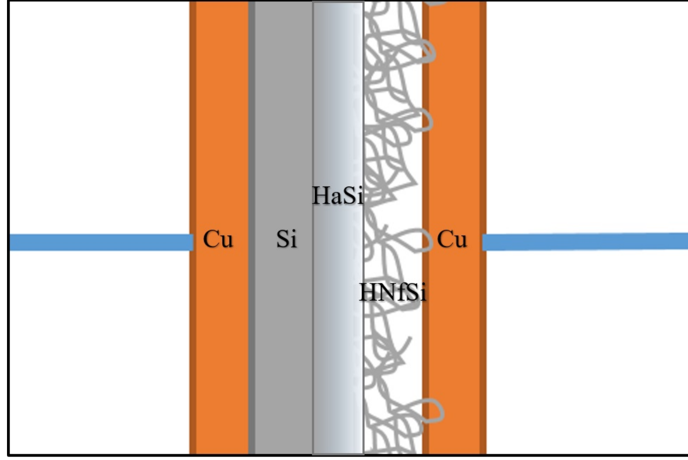

Figure 3.2: HNfSi accommodation between two copper electrodes with figurative demonstration of heat affected zone (HaSi).

As shown in Figure 3.2, all the components associated with such configuration connected in series with the resistivity measuring circuit. Hence, resistance offered by copper, silicon, heat affected zone in silicon and HNfSi can be denoted as R_{Cu}, R_{Si}, R_{HaSi} and R_{HNfSi} respectively. Total resistance, R_{Total}, offered by such system can be shown with equation below,

$$R_{Total} = 2 \times R_{Cu} + R_{Si} + R_{HaSi} + R_{HNfSi} \tag{3.6}$$

Upon laser processing of polycrystalline silicon, the formation of defect states would occur at the grain boundaries along with enlarged grains causing decrease in conductivity. When laser ablation rate in such process was increased from 300 mJ/cm^2 to 400 mJ/cm^2, conductivity of the heat affected film was decreased from ≈ 0.3 S/cm to ≈ 0.1 S/cm [258]. However, in this study, only the single crystal silicon (99.99% pure) was used. Therefore, with no irregular crystalline boundaries, heat affected zone in pure silicon is less likely to have drastic change in resistivity. Considering immense resistive behavior of manufactured fibrous thin film, slight increase in resistivity of heat affected zone can be assumed to be the

same as silicon for simplicity. Hence,

$$R_{Total} = R_{Si} + R_{HNfSi} \rightarrow R_{Total} = \left(\frac{\rho l}{A}\right)_{Si} + \left(\frac{\rho l}{A}\right)_{HNfSi} \tag{3.7}$$

In above equation, l represents the thickness of respective entity. Similarly, A depicts least cross section area available with such configuration. Total resistivity offered by Si is calculated to be 0.361 $M\Omega.mm$. Hence, with ImageJ analyzed dimensions of thickness associated with Si and HNfSi, resistivity offered by specific fibrous structure can be calculated with equation below,

$$\rho_{\ HNfSi} = \left(\frac{A}{l}\right)_{HNfSi} \left[R_{Total} - \left(\frac{\rho l}{A}\right)_{Si}\right] \tag{3.8}$$

3.3 Surface topology for sensing [2]

3.3.1 Surface area enhancement with nano particles

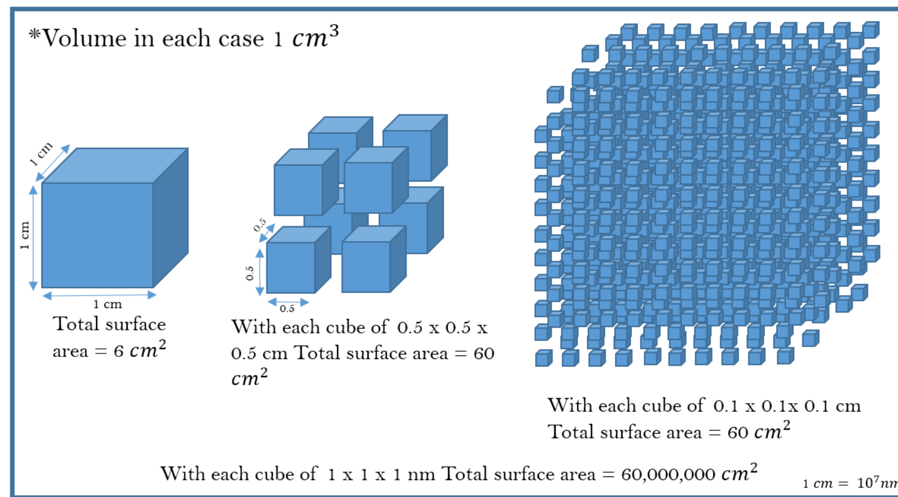

Figure 3.3: Surface area with miniaturization of the same volume.

As discussed earlier, the surface area of sensing probe plays an important role in performance of the sensor. Exponential enhancement of the surface area with miniaturization can be understood by Figure 3.3. Same cube with 1 cm^3 volume

[2]Chapter 3.3 has been published as a review paper titled 'Nano structured sensing surface: Significance in sensor fabrication' in Elsevier journal Sensors and Actuators B. `https://doi.org/10.1016/j.snb.2018.04.085`.

which normally possess 6 cm^2 of area, can have area of 6×10^7 cm^2 if spliced in to nano cubes. It is easy to understand that the molecular detection possibilities in application such as gas sensing can be higher with enhanced surface area and with smaller probes which can be quite beneficial for miniaturized sensors with high sensing performance.

3.3.2 Nanofiber diameter for sensors

As per conventional approach to understand resistivity or conductivity, associated diameter and transmission length of structure affects such characteristics significantly. In case of nano fibers, this effect can be maximized considering its significantly small diameter. In addition, due to potential of HNfSi to be used as sensing surface of anthropometric sensors where change in electrical conductivity is measured; understanding effect of fiber diameter on electrical characteristics is essential. As shown in Figure 3.4, consider the nanowire with E_D free electrical carriers with charge q which has effective surface diameter of D_a initially. After interactions with analyte, the thickness of a layer by accumulated analyte molecules would be $D - D_a$. To counter effect, depending on the nature of charged molecules, the free carriers from nanowires will accumulate to the surface which then reduce the effective diameter from D_a to D_b. Considering the drift carrier velocity [259], basic current estimation for nanowire with radius R_a would be,

$$I = Carrier\ velocity(\nu) \times Area(\pi {R_a}^2) \times Electrical\ charge(qE_D) \tag{3.9}$$

Ideally, the charge accumulated on the nanowires in form of analyte should be equal to the charge accumulated by free carriers inside the nanowire. The relation between both can be shown with equation 3.10. Where E_{mol} is number of foreign molecules recited on the nanowires. If all these information would be used to calculate the sensitivity by employing general definition of sensitivity in terms of induced current as $S \approx (I_a - I_b)/I_b$, then performance can be shown in the form

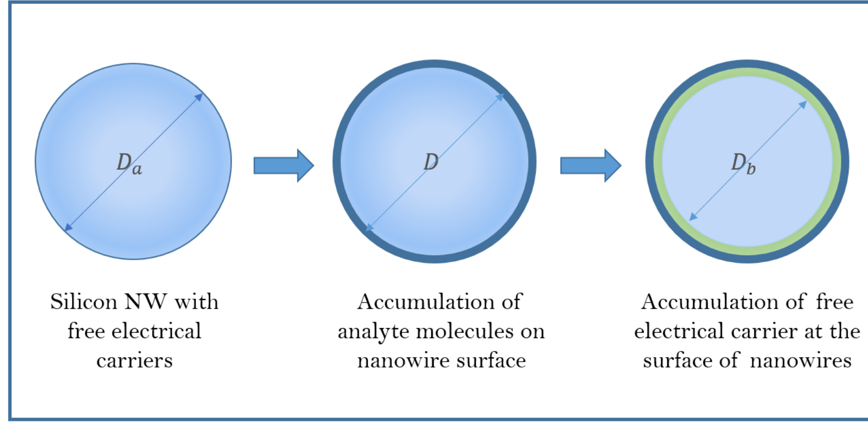

Figure 3.4: Effect of nanowire diameter on sensitivity.

of equation 3.11 [260, 261].

$$Q_{mol} = qE_D(\pi {R_a}^2 - \pi {R_b}^2) = qE_{mol}\pi D_a \tag{3.10}$$

$$S \approx \frac{E_{mol} D_a}{E_D {R_a}^2} \approx \frac{4E_{mol}}{E_D D_a} \tag{3.11}$$

As per basic understanding, reducing diameter should reduce the electrical conductivity; contrary above equation depicts that sensitivity can increase with reducing diameter and lowering doping density because reduced carrier numbers can help magnify the change as initial current would be smaller and resulting change would be relatively larger causing higher sensitivity. In addition, the equation suggest that increase in a diameter caused by analyte molecule accumulation can result in a higher sensitivity which might be because of simultaneous increase in sensing surface area.

The equation 3.11 presents some limitation with detection of uniformity of charge on surface, fail to account for effect of fluidic environment on performance, variance in charge because of presence of not-in-interest molecules and detection of depletion mode operation without separating it from accumulated charge. Despite all the limitations, basic comprehension can be gathered as nanowires with smaller diameter and lower doping concentration can be helpful to achieve higher sensing performance. Despite the advantages, it is necessary to consider that the

trend of sensing improvement with miniaturized probe may not provide significant advantage after reaching certain level because of inherent sensing limit associated with diffusion, time required for analyte molecules to encounter sensing probe and settling time [262, 263]. In addition, potentiometric sensing behavior can be limited by charge type of the analyte molecules. For example, in case of nonporous surface, if the substrate is charged, it will repel the analyte molecules with the similar charge type causing an inaccurate analyte detection [264].

3.3.3 Critical silicon nanowire diameter

As the depletion zone formation happens near the surface of nanowires, it is important to control the non conductive zone to maintain current flow. If diameter of the nanowire is reduced below certain level, the number of mobility charges can be reduced relatively because of comparatively smaller available volume. Furthermore, depletion zone at the time can be bigger to overtake the full diameter of a fiber causing accumulation of all free carriers from the nanowires and making it almost impossible to flow the current to detect a signal. In case of silicon nanofibers, laser processing in ambient condition can lead to oxidized nanofibers formed with layer of SiO_2 [265]. The formation of layer can significantly affect the performance as it contains the trapped charges near to $Si - SiO_2$ interface.

for such case, to avoid full depletion of the nanowires Schmidt et al. [266] have derived equation to calculate the critical radius of nanowires with related interface trap level density. The calculated value is a radius for full depletion of a nanofibers. Hence, according to equation 3.12 radius above critical radius will be a safe value to achieve partial depletion in nanowires.

$$a_{critical} = \frac{\varepsilon_s}{q^2 E_{it}} \left[-1 + \left[\frac{4q^2 E_{it}}{\sigma \varepsilon_s} (q^2 E_{it} \psi_0 - Q_f) \right]^{1/2} \right] \tag{3.12}$$

In equation 3.12 ψ_0 is a potential at $r = 0$, E_{it} is an interface trap level density ($ev^{-1}cm^{-2}$), ε_s is a relative permittivity of silicon, Q_f is a density of fixed oxide

charges and q is an elementary charge. For simplification, expansion of square root of such equation to the first order can be written as equation 3.13. According to the equation 3.12, reduction in the value of trapped charge densities can help achieve smaller critical radius. One of the approach to accomplish that could be annealing process in oxygen atmosphere which forms high quality oxide followed by short annealing in hydrogen atmosphere ensuring passivation of remaining interface states [267].

$$a_{critical} \approx \frac{2}{\sigma}(q^2 E_{it} \psi_0 - Q_f) \tag{3.13}$$

In both of the equations, estimation of terms like ψ_0 is quite complicated as it requires knowledge of density of available donors and acceptors as well as density of states in the conduction and valence band [266, 268]. However, in our study, content formation of SiO_2 can be estimated relatively which limits the accuracy. In addition, such mathematical model also ignores the variation in dimensions of nano fibers and charges fused from the bulk silicon underneath the fibrous structure. Furthermore, it is also important to note that the oxidation layer developed on fibrous structure may not have uniform cross section and homogeneity throughout oxidized layer. However, with the additional work in future, obtained available information on SiO_2 content, behavior with varying surface topology and other required quantities, one might be able to calculate and correlate critical diameter required for efficient performance with the context to application in interest.

Chapter 4

Effects of laser frequency, power and scanning loops[3]

As explained in section 1.4.1, laser plasma processing causes the accumulation of naoparticles dispersed on the surface and in some cases, structured as nano fibers. Such accumulation can be identified through TEM (Transmission electron microscopy) results of nanofibers as shown in figure 4.1(a).

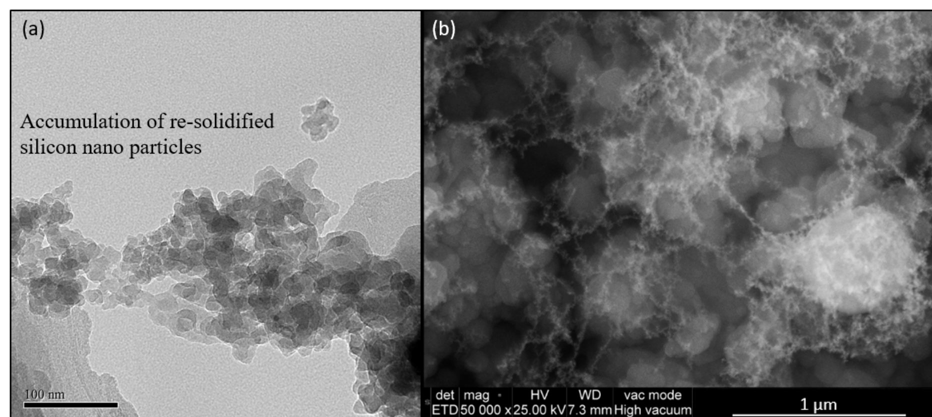

Figure 4.1: (a) Formation of nano fibers caused by accumulation of Re-solidified Silicon Nano-particles (R-SiNp). (b) SEM result of laser ablated silicon surface - mixture of nano particles and nano fibers.

As the ablation process being conducted in air, the re-solidified particles and nanofibers may get oxidized [92, 265]. In case of ablation with pico-second laser,

[3]Chapter 4 has been published with title 'Pulsed ionized mesh-like assembly of hybrid silica nanostructures with controlled resistivity' in Elsevier journal Applied Surface Science. https://doi.org/10.1016/j.apsusc.2018.05.107.

pulsation width being quite smaller than time required for conventional melt down of crystals, with enough power and frequency, it can enable evaporation without phase transfer (i.e metal to vapor conversion) [235–237]. This will motivate the generation of relatively smaller melt-pool with dense fibrous structure. Thus, silicon ablation process done using pico-second laser could be more beneficial for fiber generation than laser with longer pulsation width.

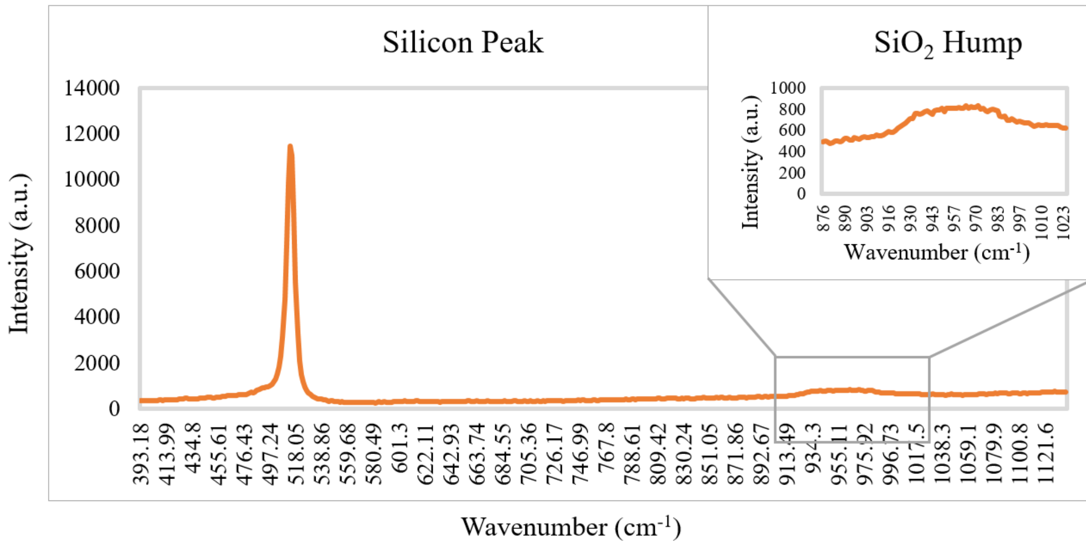

Figure 4.2: Raman spectroscopy results for HNfSi.

In this study, the SEM results depicts the generation of R-SiNp (Re-solidified Silicon Nano Particles) with nano fibrous structure as shown in Figure 4.1(b). Silicon and silicon dioxide characteristics can be identified at wavelength of 519 cm^{-1} and 954 cm^{-1} respectively in Raman spectroscopy results by observing the signal domination at such wavelengths [269]. Considering the frequency peak and hump, presence of Si and SiO_2 resulted from oxidation of fibers and silicon particles can be noticed in Raman spectroscopy results shown in Figure 4.2. As fibrous topology offers more surface area with oxidized fibers, the oxygen content on the same area increases significantly. Contrary, the silicon content remains dominating where there is a presence of R-SiNp which can be noticed from the EDX results shown in Figure 4.3(a) and 4.3(b). Moreover, content proportion of the nano fibers and R-SiNp plays an important role in various characteristics of the HNfSi. In this

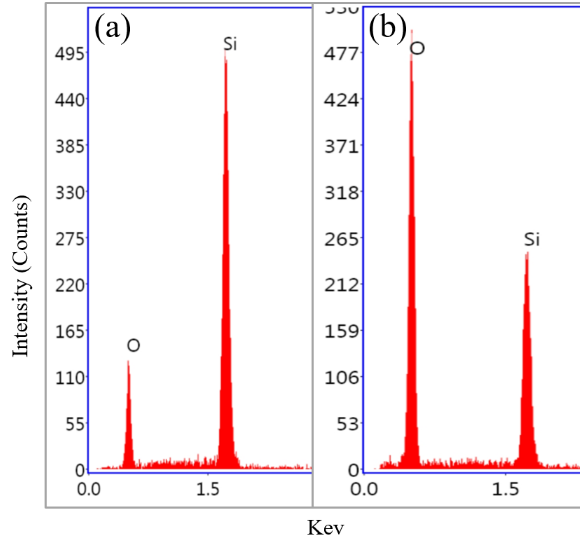

Figure 4.3: (a) EDX result for the spot with R-SiNp on HNfSi (b) EDX results for spot with dense silicon nano fibers on HNfSi.

study, we have used various laser parameters such as frequency, power and scanning parameter like loop to generate HNfSi with different topological conditions. Furthermore, focus of this study is to determine the change in bulk electrical resistance of HNfSi with respect to variation in different laser and scanning parameters.

4.1 Effects of variation in laser frequency

Silicon laser ablation processing was done at frequency value of 1200 kHz, 800 kHz and 600 kHz with keeping other laser and scanning parameters constants as mentioned in section 2.1. SEM results for the samples prepared at described frequencies are shown with resolution of 50,000X and 10,000X in Figure 4.4 along with the detailed analysis of topological characteristics in Figure 4.5 and 4.6.

As it can be noticed on Figure 4.4(a), fiber formation did not happen with the frequency of 600 kHz. From ImageJ analysis of Figure 4.4(a), the diameter of R-SiNp was found to be ranging from $\approx$ 175 nm to 725 nm. Contrary, as we increase the frequency from 600 kHz to 800 kHz, presence of nano fibers was found as shown in Figure 4.4(b). Such fibrous structure occupies area fraction of $\approx$ 17% of total area and R-SiNp with diameter ranging from $\approx$ 175 nm to 675

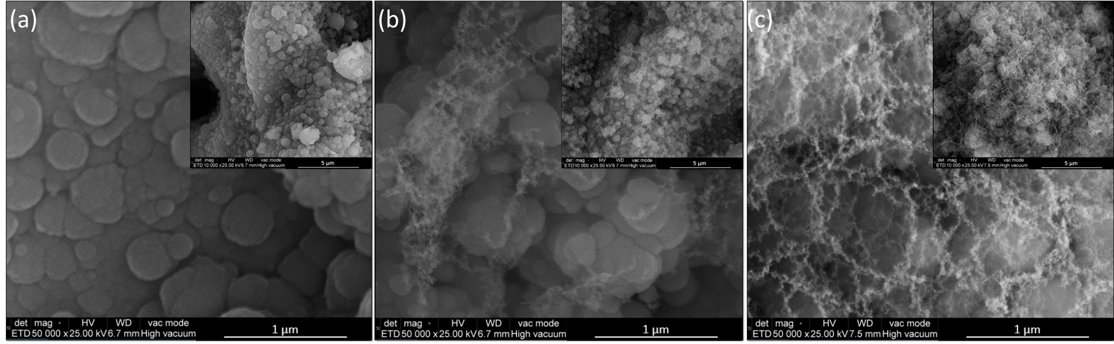

Figure 4.4: SEM images (resolution of 50,000X and 10,000X) of HNfSi produced by laser processing with repetition rate of (a) 600 kHz (b) 800 kHz and (c) 1200 kHz.

nm. Further increase in frequency results in considerable generation of fibrous structure which can be seen in Figure 4.4(c). The area covered by the fibrous structure increased from 17% to almost 42% when frequency was elevated from 800 kHz to 1200 kHz. In addition, with the same increment in frequency, the existence of R-SiNp bounded by nano fibrous structure was identified in Figure 4.4(c). The diameter for R-SiNp was found to be ranging from $\approx$ 225 nm to 975 mm. It is important to note that the particles above $\approx$ 600 nm is more of cluster made of small particles rather than a single identifiable R-SiNp. Such clusters above 1 μm are not considered for the ImageJ analysis.

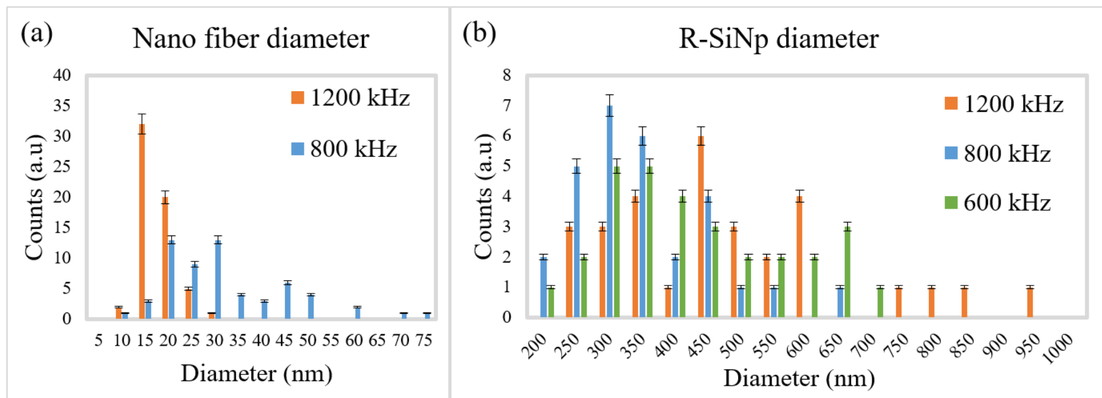

Figure 4.5: Comparison of distribution of (a) nano fiber (using 50,000X SEM image) and (b) R-SiNp (using 10,000X SEM image) diameter for HNfSi prepared with frequency of 1200 kHz, 800 kHz and 600 kHz.

Moreover, the distribution of particles and nanofibers with respect to their diameter range can be seen in Figure 4.5. From the analysis of Figure 4.5(a), the

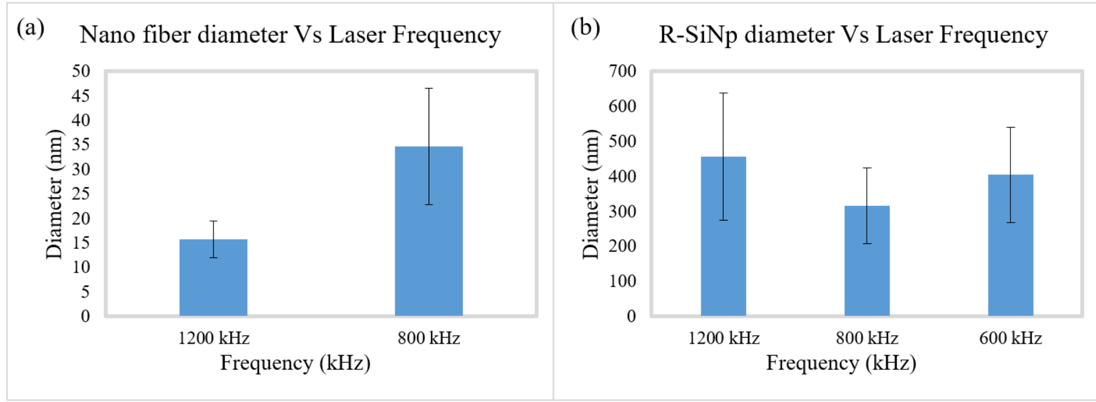

Figure 4.6: Comparison of (a) nano fiber (using 50,000X SEM image) and (b) R-SiNp (using 10,000X SEM image) mean diameter for HNfSi prepared with frequency of 1200 kHz, 800 kHz and 600 kHz.

diameter of silicon nanofibers manufactured using 1200 kHz frequency laser ablation was found to be in a relatively short range of $\approx$ 8 nm to 33 nm with average diameter of $\approx$ 15.5 nm. Contrary, with the use of 800 kHz of frequency, it was observed to be in wide range varying from $\approx$ 12 nm to 77 nm with average diameter of $\approx$ 34.7 nm. Hence, significant difference was observed between average nano fiber diameter of samples processed with 1200 kHz and 800 kHz of laser frequency as shown in Figure 4.6(a). Furthermore, as per Figure 4.5(b), samples prepared with 600 kHz laser frequency ablation have diverse and non-uniform trend for particle formation. Contrary, for frequency of 800 kHz, almost 70% of formed R-SiNp particles have diameters ranging from $\approx$ 175 to 425 nm. However, as shown in Figure 4.5(b), the distribution with respect to size of R-SiNp is observed to be random and non-uniform for the sample processed with frequency of 1200 kHz. As shown in Figure 4.6(b), It is important to note that, there was no significant difference between the average diameter of R-SiNp formed with laser ablation frequencies of 1200 kHz and 600 kHz. However, difference of the same was considerable when compared with the sample processed using 800 kHz of laser frequency.

Such variation in topological structure of HNfSi can impact the electrical behavior in various terms. From Figure 4.7, the normal trend of increase in resistance can be noticed as the frequency is varied from 600 kHz to 1200 kHz. Resistance

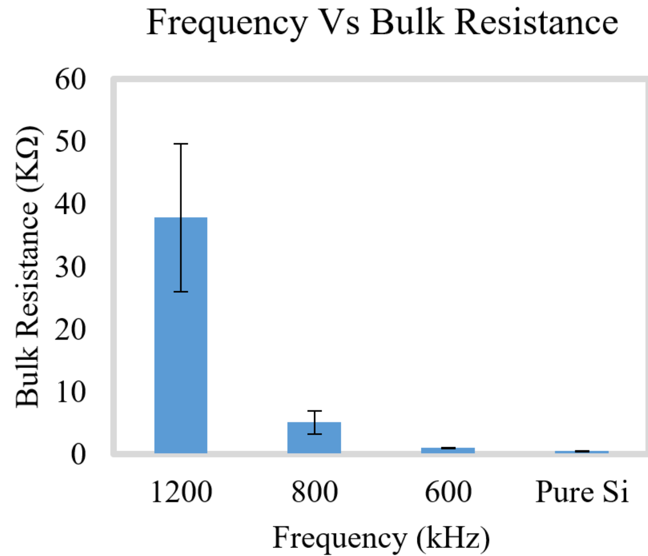

Figure 4.7: 4-Point resistivity measurement of HNfSi processed with laser frequency of 1200 kHz, 800 kHz and 600 kHz.

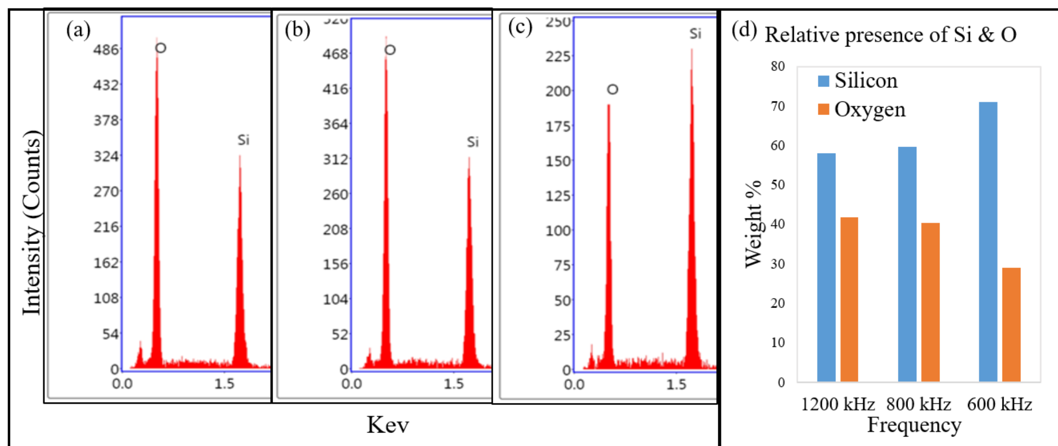

Figure 4.8: EDX results for HNfSi processed with frequency of (a) 1200 kHz (b) 800 KHz and (c) 600 KHz with (d) presence of silicon and oxygen by weight%.

change could be caused due to many possible factors namely porous fibrous topology, oxidized nano fibers and also content of R-SiNp. Such increase in resistance can be justified by the ImageJ analysis of Figure 4.4 and EDX results shown in Figure 4.8. As discussed before, transcending towards high laser frequency helps formation of dense nano fibrous structure with lessening of R-SiNp. In case of ablation with relatively lower laser frequency, higher content of R-SiNp causes lower surface area resulting in a relatively lower SiO_2 content which enables somewhat moderate resistive behavior of HNfSi. Contrary, laser ablation with relatively

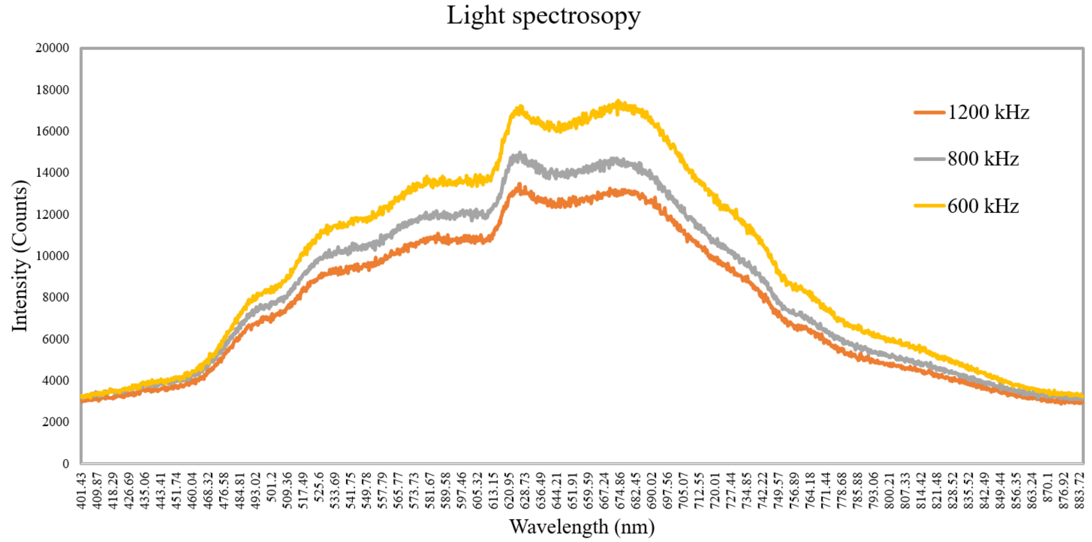

Figure 4.9: Light spectroscopy analysis for HNfSi processed with laser frequency of 1200 kHz, 800 kHz and 600 kHz

higher laser frequency produces much more surface area with dense fibrous structure along with dominating SiO_2 content causing intense resistive behavior. Minor increase in resistance for HNfSi prepared with frequency of 800 kHz with respect to 600 kHz and drastic elevation in resistance with frequency of 1200 kHz with respect to 800 kHz can be explained from availability of silicon nano fibrous structure from Figure 4.4. HNfSi prepared with 1200 kHz of frequency possesses much dense and defined fibrous structure than HNfSi prepared with 800 kHz of frequency causing drastic elevation in resistance. Similarly, HNfSi processed with 800 kHz has minor presence of fibrous structure contributing to slightly higher resistance than HNfSi prepared with 600 kHz of frequency.

Furthermore, light spectroscopy results of HNfSi, as shown in Figure 4.9 depicts significant difference in terms of light reflectance characteristics for HNfSi processed with different laser frequencies. The difference between light absorption can be caused due to the overall topological characteristics of the ablated silicon surface. As discussed before, increase in frequency enables the formation of fibrous structure causing overall enlarged surface area. Hence, the light absorption increases with wider available surface area. Overall, due to provision of proper plum atmosphere with increase in frequency, the laser ablation causes formation

of oxidized and dense fibrous structure contributing to intense resistive behavior of ablated HNfSi. The effect of power on similar physical and electrical properties of HNfSi is discussed in the next section.

4.2 Effects of variation in laser power

Silicon samples were prepared using three different power levels - 10 W, 15 W and 20 W. The parameters like pulsation width, scanning speed and leading distance were kept constant as before. Laser frequency was set to 1200 kHz with 1 loop of scanning for specimen preparation. SEM results of HNfSi prepared with different power level can be seen in Figure 4.10 with resolution of 50,000X and 10,000X respectively.

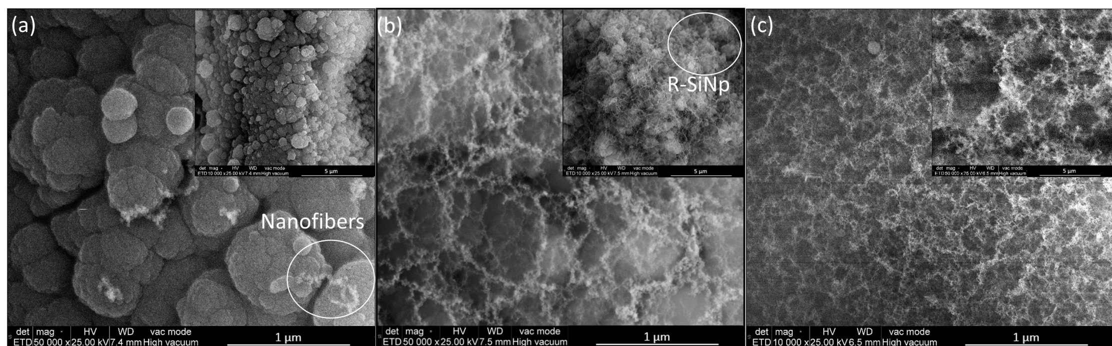

Figure 4.10: SEM images (resolution of 50,000X and 10,000X) of laser processed HNfSi with power level of (a) 10 W (b) 15 W and (c) 20 W.

From the SEM results, it was observed that the effect of power can be significant on the generation of fibrous structure and R-SiNp. With relatively lower power of 10 W, the laser ablation process generates HNfSi made of R-SiNp with almost no existence of silicon nano fibers which can be seen in Figure 4.10(a). From detailed observation of Figure 4.10(a), it was found that there is a minute formation of fibrous structure is taking place as described using circle mark. As the power is increased from 10 W to 15 W, formation of the nano fibers structure becomes more evident because of increase in overall ablation energy which can be seen from Figure 4.10(b). However, significant amount of R-SiNp can be seen underneath

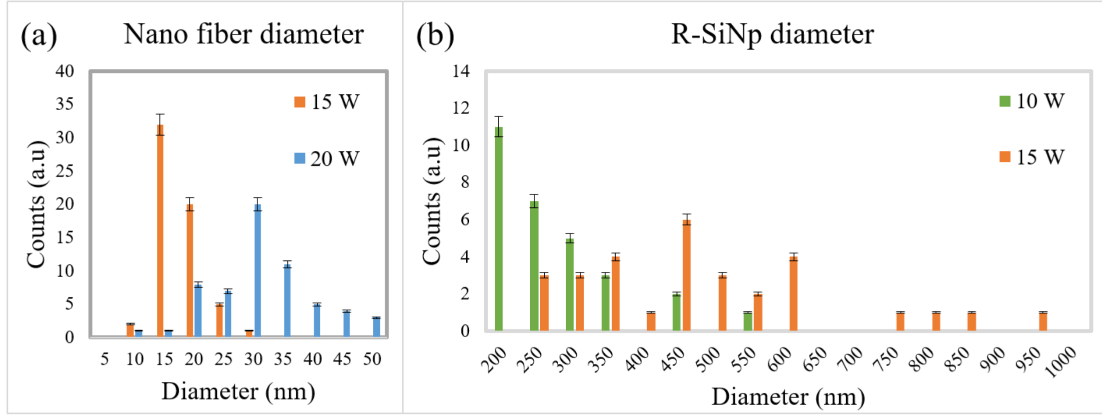

Figure 4.11: SEM images (resolution of 50,000X and 10,000X) of laser ablated HNfSi with power of 20 W, 15 W and 10 W.

the fibrous structure in low resolution figure as shown using circle marks. Overall, laser ablation with power value of 15 W forms the R-SiNp covered with fibrous structure. Furthermore, dense and uniform fibrous structure is achieved when laser power was increased from 15 W to 20 W. Figure 4.10(c) depicts the porous, uniform and 3D-fibrous structure formed with the laser power of 20 W.

Detailed ImageJ analysis of Figure 4.10 was done to inspect the topological structure formed using ablation with various power values which can be seen in Figure 4.11 and 4.12. Formation of fibrous structure instead of dominating R-SiNp with increase in the power was observed as shown in Figure 4.10. By analyzing Figure 4.11, for the silicon sample processed with 10 W of power, diameter of R-SiNp was observed to be in range of ≈ 175 nm to 575 nm. Increase in power from 10 W to 15 W contributes to more energy per pulse resulting in a suitable higher temperature which enables the formation of porous structure made of R-SiNp and silicon nano fibers. Such increase in power enables the formation of R-SiNp particles having diameters ranging from ≈ 225 nm to 975 nm. It is important to note that the significant difference between average diameter of R-SiNp was found for samples processed with 10 w and 15 W of laser power as shown in Figure 4.12(b).

In addition, nanofibers formed with 15 W of power have diameter ranging from ≈ 8 nm to 33 nm with area fraction of ≈ 42% of total area. However, the most

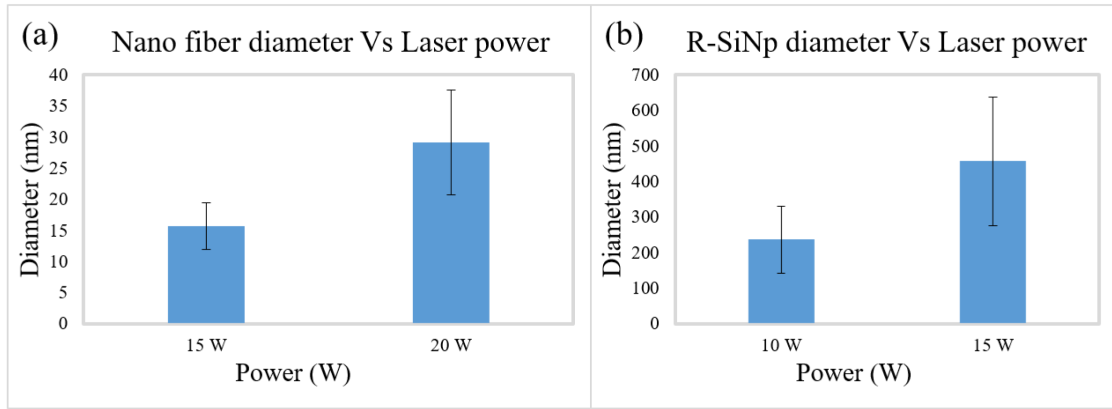

Figure 4.12: Comparison of (a) nano fiber (using 50,000X SEM image) and (b) R-SiNp (using 10,000X SEM image) mean diameter for HNfSi prepared with power of 20 W, 15 W and 10 W.

fibers has average diameter of ≈ 15.5 nm. As the power was elevated from 15 W to 20 W, significant change was observed in size of nano fibers and presence of R-SiNp. With the highest power among all three power values, diameter of formed nano fibers found out to be ranging from ≈ 8 nm to 53 nm with average diameter of ≈ 29.2 nm. Also, the area fraction was covered with fiber increased from ≈ 42% to 59% with elevation in laser power. Moreover, significant difference of silicon nano fiber mean diameter was observed between samples processed with laser power of 15 W and 20 W as shown in Figure 4.12(a). Overall, elevation in power values from 10 W to 20 W provides topological structure ranging from complete R-SiNp to dense and porous surface made of silicon nano fibers.

To understand the basic electric characteristics of resistance offered by all three samples prepared with various power values, the 4-point probe was employed. Results achieved from the test are shown in the Figure 4.13.It is evident to notice significant increase in resistive behavior of the processed samples as the power values were elevated. Increase in resistive behavior can be explained from the ImageJ analysis. As already described in section 4.1, content proportion along with topology of R-SiNp and silicon nano fibers can be a key contributing factor for such resistive characteristics. When lower power level of 10 W was employed, the generated R-SiNp tends to offer relatively less surface area with lower content

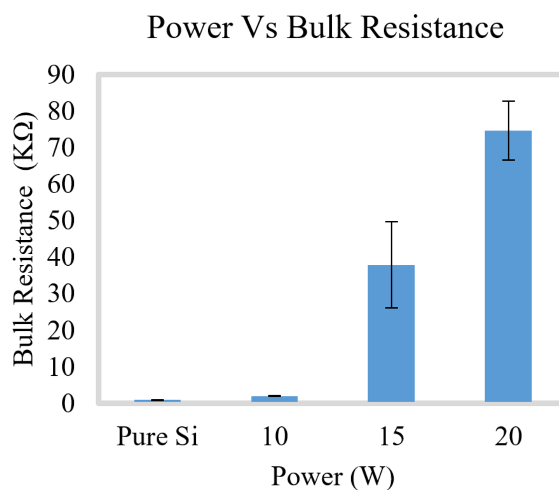

Figure 4.13: 4-Point resistivity measurement of HNfSi processed with power of 10 W, 15 W and 20 W.

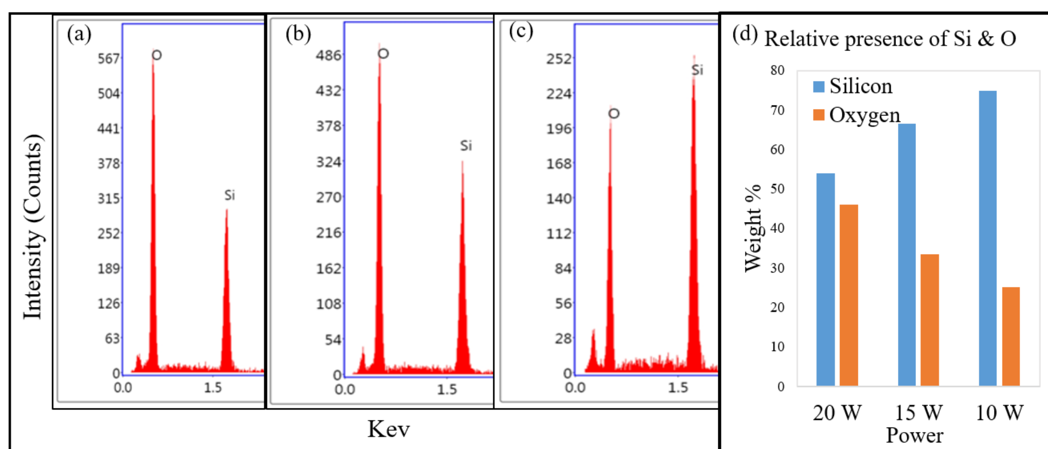

Figure 4.14: EDX results for HNfSi processed with laser power of (a) 20 W (b) 15 W and (c) 10 W with (d) presence of silicon and oxygen by weight%.

of SiO_2 which contributes to mild resistive behavior. Contrary, with increase in power values, instead of R-SiNp, formation of silicon nano fibers takes place which causes enhanced surface area with higher amount of SiO_2 caused by oxidation of newly formed silicon nano fibers. Moreover, same trend of domination of SiO_2 with increase in frequency can be confirmed by EDX analysis of HNfSi as shown in Figure 4.14. As discussed before, SiO_2 having relatively intense resistive characteristics affects the electrical behavior offered by processed HNfSi which can be seen in Figure 4.13.

Furthermore, presence of nano fibers can be observed from the reflectivity of

HNfSi. Enhanced surface area can cause higher absorption of the same source of light. Figure 4.15 depicts the light reflected by HNfSi processed with various power level. As expected, the specimen prepared with highest power level offers

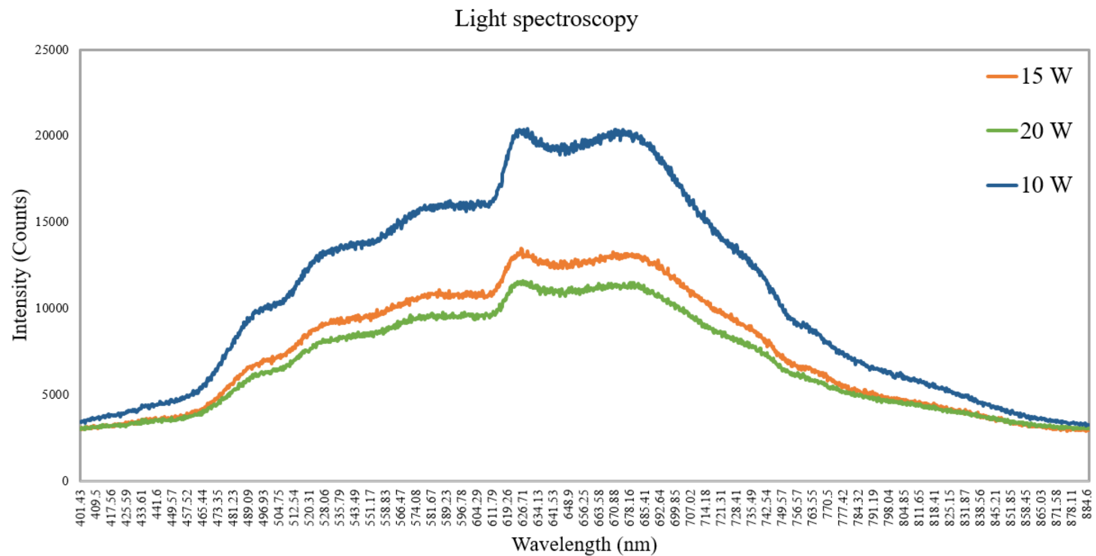

Figure 4.15: Light spectroscopy analysis for HNfSi processed with laser power of 20 W, 15 W and 10 W.

least reflectivity mainly due to higher surface area offered by silicon nano fibers. Contrary, sample ablated with least power value offers the highest reflectivity which can be due to dominating content of R-SiNp on HNfSi. However, there is not as significant difference were identified between reflectivity of samples processed with power level of 15 W and 20 W. The reflective characteristics of top most surface of both of the ablated samples can be quite similar as R-SiNp formed underneath the layer of nano fibrous structure in case of laser ablation with 15 W, does not play significant role in this analysis.

Overall, amount of energy released to the ablated surface using ultra short pulses can significantly affect various characteristics of nano structured surface. Depending on the power level, energy released to the surface can form topology made of R-SiNp, 3D porous silicon nano fibers or combination of both. Depending on the structural topology of HNfSi along with oxidation level, laser processed silicon can possess diverse resistive characteristics.

4.3 Effects of number of scanning loops

Scanning parameter - number of ablation loop was varied from 1 to 3 to prepare three different samples. Other important parameters like scanning speed, leading distance and pulse duration were kept constant as described before. Also, laser parameters like frequency and power were set at, in order, 1200 kHz and 15 W for preparation of all test specimens. SEM results for laser ablated HNfSi with such variation are shown in Figure 4.16.

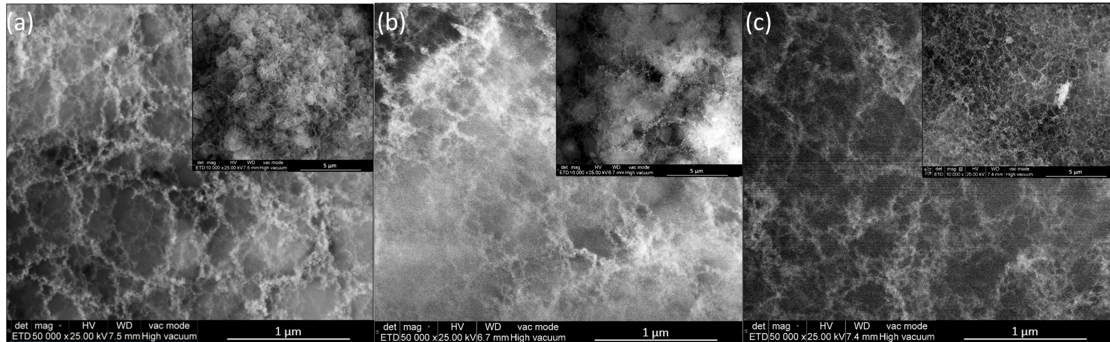

Figure 4.16: SEM images (resolution of 50,000X and 10,000X) of laser processed HNfSi prepared with number of loops - (a) 1 (b) 2 and (c) 3.

Significant formation of nano fibers in each case was found. However, visual analysis of sample prepared with 1 loop indicates presence of R-SiNp covered with silicon nano fibers as shown in 4.16(a). When laser scanning was performed two consecutive times, the R-SiNp covered with silicon nano fibers seems to be converting in densely accumulated fibrous structure on top of randomly shaped R-SiNp chunks which can be seen in 10,000X Figure 4.16(b). With significant generation in nano fibrous structure, scanning of ablation surface for three times produced completely porous and defined silicon nano fibers.

As shown in Figure 4.17(a), ablation with 1 number of loop creates fibrous structure with relatively narrow range of diameter i.e.$\approx$ 8 nm to 33 nm with area fraction of $\approx$ 42% of total area. Ablation on already fabricated fibers with second loop, the distribution of fibers with available diameters changes drastically as shown in Figure 4.17(a). For, HNfSi fabricated with 2 consecutive scan of laser ablation have diameter ranging from $\approx$ 8 nm to 77 nm with area fraction of $\approx$

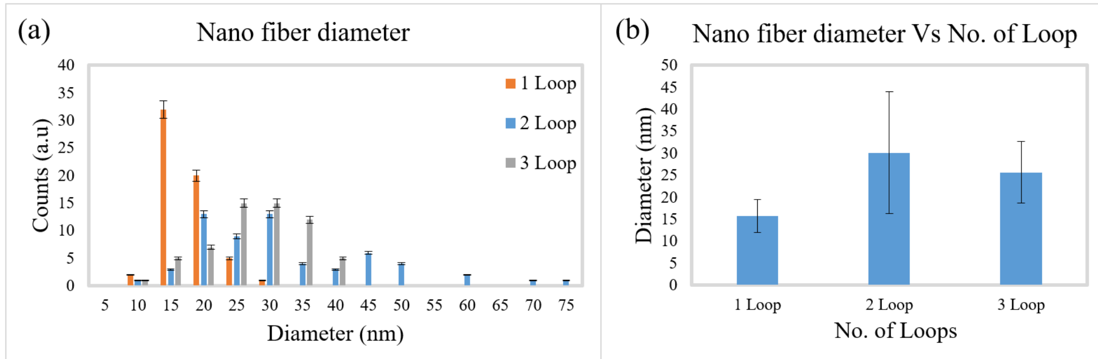

Figure 4.17: Comparison of (a) distribution and (b) mean of fiber diameter for HNfSi prepared with variation in scanning loops from 1 to 3.

57% of total area. However, when laser processing was done with repetition of 3 loop, the range of diameter of silicon nano fiber decreases with numbers ranging from ≈ 8 nm to 43 nm along with area fraction increment of ≈ 4%. Furthermore, mean diameter of ≈ 15.5 nm for samples processed with 1 loop increase to ≈ 30.2 nm when ablated again with second loop. However, when processed with 3 consecutive loops of scanning, fiber mean diameter decreases to ≈ 25.7 nm. Anova analysis with one factor and confidence level of 95%, suggests that there is significant difference between mean diameter for fibers processed with different loops as shown in figure 4.17(b).

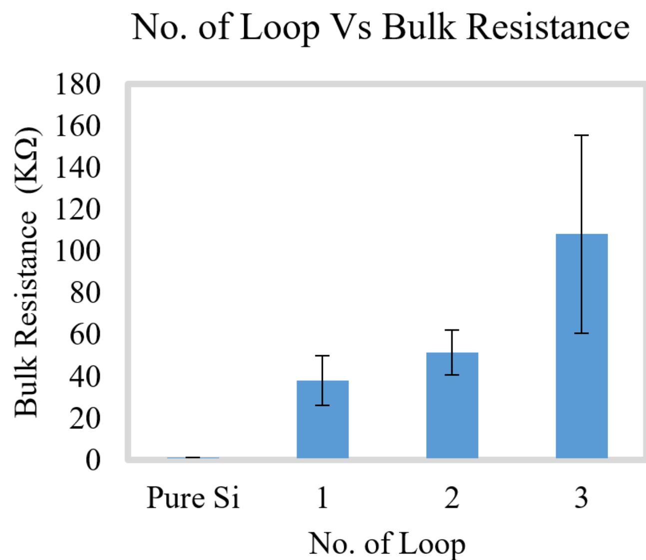

Figure 4.18: 4-Point resistivity measurement of HNfSi prepared with variation in scanning loop from 1 to 3.

4-point probe measurements were carried out to comprehend resistive characteristics of HNfSi prepared with various number of loops. The result of 4-point probe resistivity measurements are shown in 4.18. From Figure 4.18, positive surge in resistive behavior with increase in number of loop was observed. In addition, increment in resistivity of specimen worked with two scanning loops seems minor when compared with resistance of surface ablated with only one loop. Contrary, the change in resistance is drastic when compared sample processed using three loops of scanning. The presence of fibrous structure with dominating R-SiNp for one scanning loop and available dense fibrous structure with relatively less R-SiNp content with two consecutive loops could be the reason of minor elevation in resistance when number of loop increase from 1 to 2. Also minor, instead of significant, change in resistance could be due to presence of R-SiNp in both of the samples. However, when processed with third consecutive loop, available dense fibrous structure with no R-SiNp and dominating SiO_2 content offers most resistive behavior. Overall, increase in a number of processing loop causes formation of relatively uniform fibrous structure consisting dominating SiO_2 content (as shown in Figure 4.19 with EDX analysis of the same samples) along with lessening of R-SiNp contributing to magnified resistive behavior.

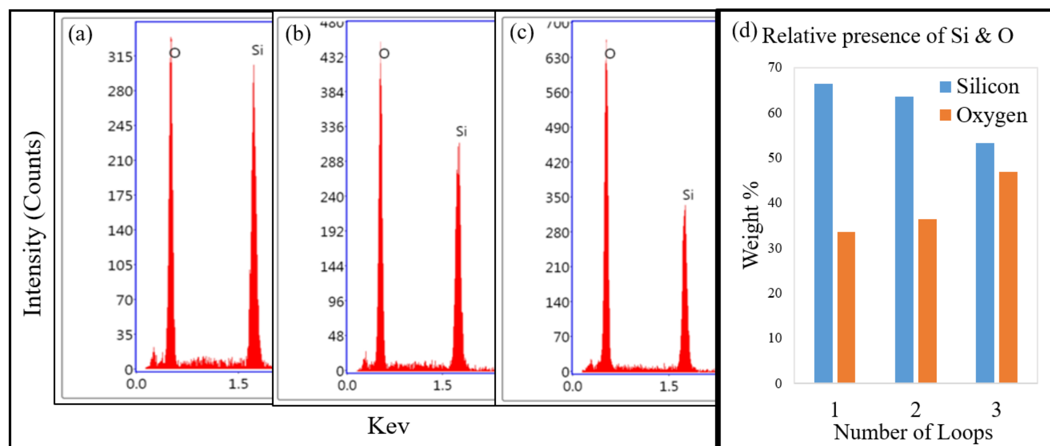

Figure 4.19: EDX results for HNfSi prepared with laser scanning loop of (a) 1 (b) 2 and (c) 3 with (d) presence of silicon and oxygen by weight%.

Understanding the formation of fibrous structure with varying number of loop is

significantly different than silicon ablation with various laser power and frequency values. While laser processing, first loop creates fibrous or R-SiNp structure, or combination of both depending upon the laser and scanning parameters as shown in 4.16(a). However, second consecutive loop may have to process surface with different characteristics than silicon. It may consist of SiO_2 coated on hybrid structure made of nano fibers and R-SiNp with extremely rough and non-uniform surface. In such case, it is important to note the value of absorption coefficient of such surface with SiO_2 embedded in hybrid structure could be significantly different than that of pure silicon wafer (i.e. 59.9 cm^{-1} at 1000 nm [270]). For example, pure glass (schott 8486 suprax glass) has absorption coefficient of 0.3 cm^{-1} at 1000 nm [271]. However, this does not indicate the true absorption coefficient of hybrid structure but suggests the possibilities of it being lower than that of pure silicon. Hence, if the surface area is increased with amount of elevated SiO_2, the surface could have relatively increased reflective behavior. Also, the same could affect further ablation and enable formation of relatively dense fibrous structure as shown in Figure 4.16(b). In addition, third consecutive loop would work similarly with generation of more fibers as it has to deal with dominating fibrous structure consisting SiO_2 which was generated at the end of second loop of ablation.

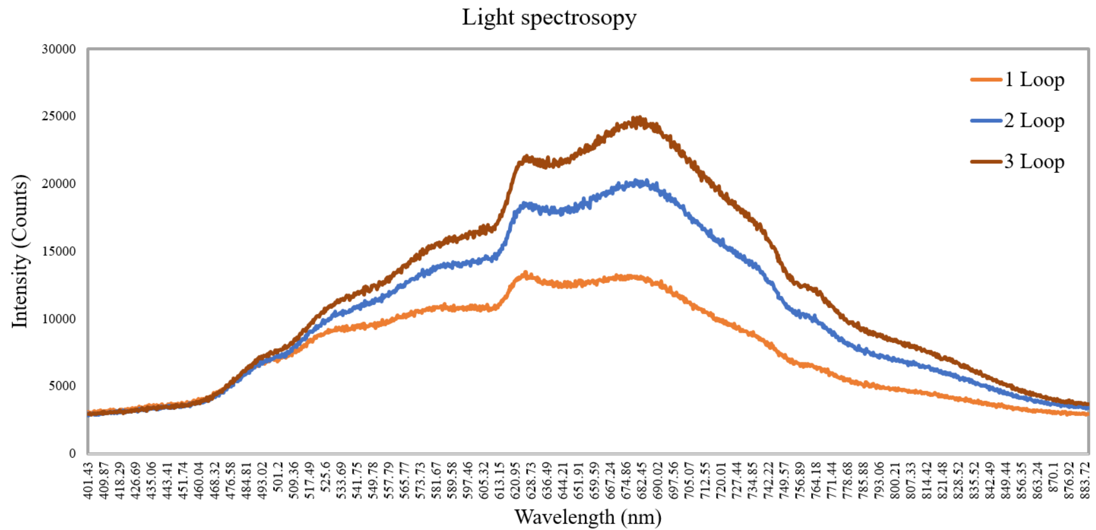

Figure 4.20: Light spectroscopy analysis for HNfSi fabricated with variation in scanning loops from 1 to 3.

Light spectroscopy results shown in Figure 4.20 depicts that the reflectivity of ablated surface increases as the number of laser processing loops were increased. As discussed before, hybrid structure made of silicon nano fibers and R-SiNp with partially oxidized outer surface is relatively less reflective than samples processed with two or three loops. As the content of SiO_2 increases with second consecutive loop of ablation, the reflective nature of the surface becomes more evident as shown in Figure 4.20. In addition, third consecutive loop increases density of oxidized fibers causing relatively intense reflective behavior of the ablated surface. Overall, variation in scanning loop causes significant changes in surface topology for next consecutive loop resulting in a complex ablation process which creates dense fibrous structure with increased number of loop and elevated SiO_2 content resulting in a resistive behavior with such trend.

Chapter 5

Effects of laser ablation temperature and leading distance

5.1 Introduction

As discussed in previous section, there are number of laser parameters which can affect various characteristics of HNfSi. However, ablation temperature and extent of process overlap can only be effectively controlled by, in order, pulsation width and the leading distance. Resistance studied in the previous section is a combine electrical property of HNfSi mounted on processed Silicon and possible heat affected zone underneath the fibrous structure. In addition to HNfSi's use as a sensing surface, it might be a good candidate for new generation of electrodes, transistors, capacitors, solar cells and batteries. For such applications, approach of employing nano-porous thin-films fabricated using various micro-nano manufacturing processes can be seen on a great surge [272–278]. With such trend, it is important to analyze resistive behavior and effect on thickness of generated fibrous layer as a separate entity with varying processing conditions. Hence, to understand the thickness based resistive behavior of HNfSi, parallel electrode configuration in conjunction with keithley 2000 was employed as shown in section 2.2.2.

5.2 Effects of change in plasma temperature

As mentioned in previous discussions, laser plasma processing with ultra short pulsation follows unconventional melting of the surface in interest. In addition, the generation of Si nano fibers caused by shock-wave and localized heating produced due to instant energy supply on the Si surface is already discussed in section 1.4.1. Hence, importance of localized temperature rise achieved during the laser plasma processing is quite significant considering generation of HNfSi.

However, for most industries and research in general, lasers are vastly known for their capability to perform operations like marking, trimming, scribing, micro-machining, diamond and silicon cutting [279–282]. Hence, in general, nano second laser is quite affordable for small scale research and manufacturing facilities in comparison to highly sophisticated pico second laser. Taking such facts into account, for this part of study, by utilizing the available laser setup with nano level of pulsation width, we were able to vary pulse width in three steps of 1, 2 and 5 ns. In addition, leading was set to 0.05 mm for all three type of samples. Theoretical difference between the range of plasma temperature achieved with various pulsation width can be understood by model developed by Hendow et al. [256]. As discussed, decrease in pulsation width should enable delivery of significant extent of energy in shorter time followed by relatively higher possibilities with local heating along with decremental bulk temperature rise. For, laser pulsation width smaller than 6 ns, it is assumed to have square shaped temporal profile, Hence, theoretical model developed by Hendow et al. can be stated as equation 3.4.

In equation 3.4, peak intensity is a ratio of power and the laser spot area. So, intensity is calculated as $I_{max} = (4P_{measured})/(\pi d^2 f \tau)$. In addition, f and F are laser pulse frequency of 1200 kHz, $P_{measured}$ and P are laser power of 15 W, k is a silicon diffusivity with value of 0.88×10^{-4} m^2/s, K is a Si conductivity with the value of 155 W/mK, γ is a fraction of pulse energy absorbed by material i.e. 1-R where R = refractive co efficient of silicon (0.325), τ is a laser pulsation width, z is a plasma ionization depth, r is a radius of laser spot diameter with respect to

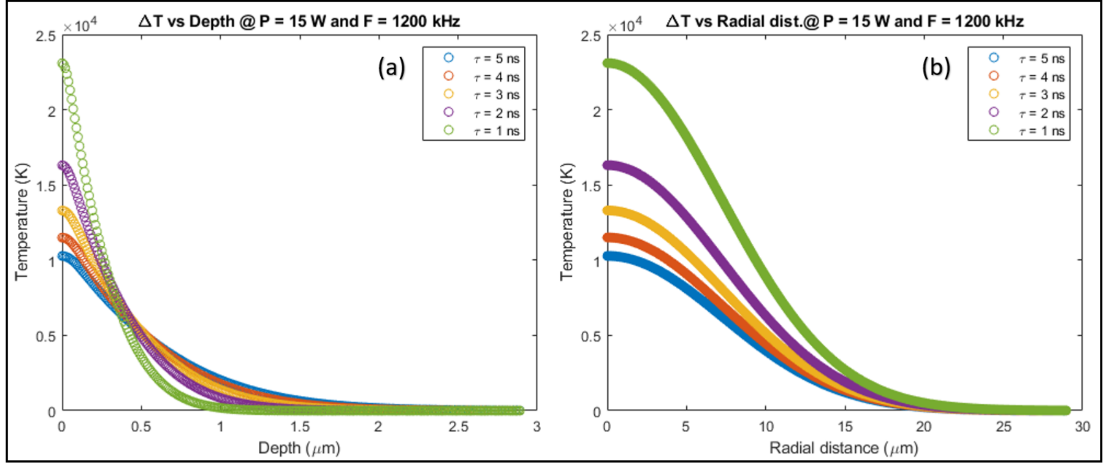

Figure 5.1: For various pulsation width, plasma temperature ΔT at Si surface with respect to (a) depth of the surface being processed and (b) radial distance from the center of focused laser spot.

center of plasma ionization and W is the value of beam's field radius $(1/e)$ with value of 2.8977×10^{-5} m. Overall, using equation 3.4, theoretical change in plasma temperature ΔT at Si surface being processed, caused by various available laser pulsation width with range of 1 to 5 ns can be seen in Figure 5.1.

After observing Figure 5.1, it is evident that decrease in pulsation width causes the higher plasma temperature. Also, rise in ΔT is not linear with linear decrement in pulsation width. Smaller τ value enables quite higher temperature at vicinity of laser spot with uniform distribution of heat over the surface instead of bulk Si material. For example, as observed in the Figure 5.1, for pulsation width of 1 ns, relatively higher temperature only persist until ≈ 1 μm of Si depth while heat distribution with same intensity of heat is spread over radius of ≈ 20 μm. Overall, relatively shorter pulsation width provides better processing condition for formation fo HNfSi.

As discussed earlier, three steps of pulsation width was available with the laser setup employed for the specimen preparation namely, 1, 2 and 5 ns. Thickness and cross section of HNfSi processed with all three pulsation width is shown in Figure 5.2. As discussed with reference to equation 3.4, higher and uniform surface ablation temperature helps in suitable condition for successful laser plasma processing

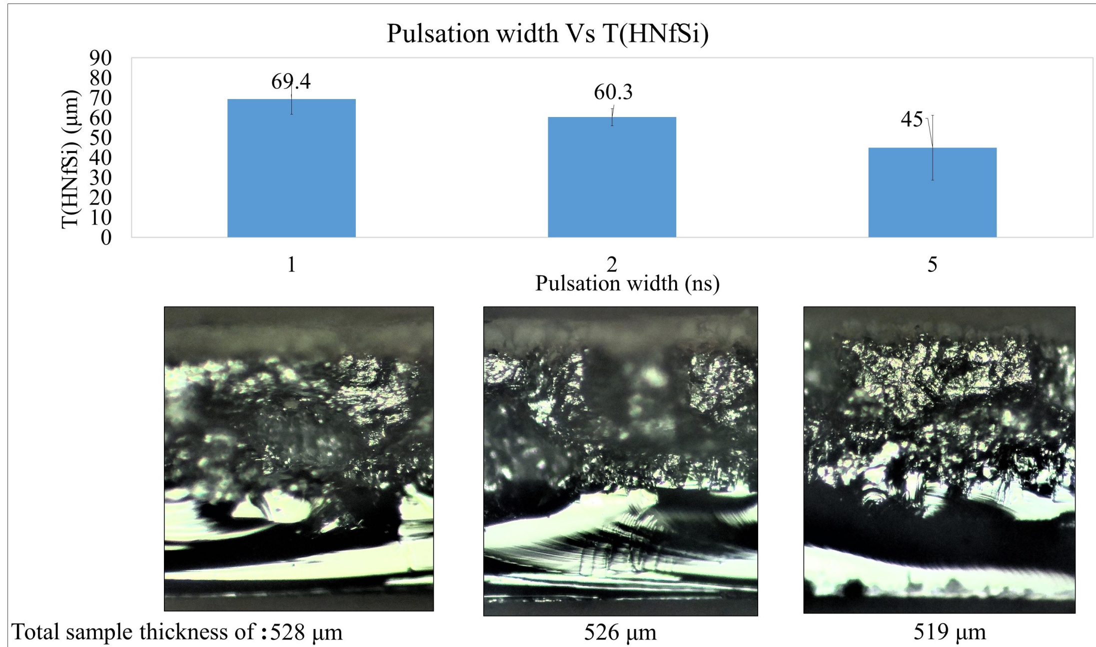

Figure 5.2: Variation in thickness of HNfSi i.e. T(HNfSi) with change in pulsation width along with cross section image of respective HNfSi.

which can be confirmed by increase in T(HNfSi) with reduction in pulsation width as noticed in Figure 5.2. In addition, decrease in T(HNfSi) is considerably large when pulsation width was decreased from 2 ns to 5 ns. Furthermore, if material content present in HNfSi is assumed to be same with identical topology for all three samples prepared with different pulsation width, then thickness based resistivity offered with parallel plate electrode configuration should be similar with increase in T(HNfSi).

However, from observing Figure 5.3, when samples prepared with different pulsation width, the relation between T(HNfSi) and resistance offered based on unit T(HNfSi) is not completely linear. Resistance offered per unit thickness by the thickest HNfSi, generated using shortest pulsation width, is highest among all three samples. Considering increase in offered resistance per unit thickness with HNfSi fabricated using diverse pulsation width, it is easy to conclude that besides from T(HNfSi), material and topology of the same might be a key factor for such sudden increase in resistance.

As discussed before, to comprehend the topological conditions of fabricated

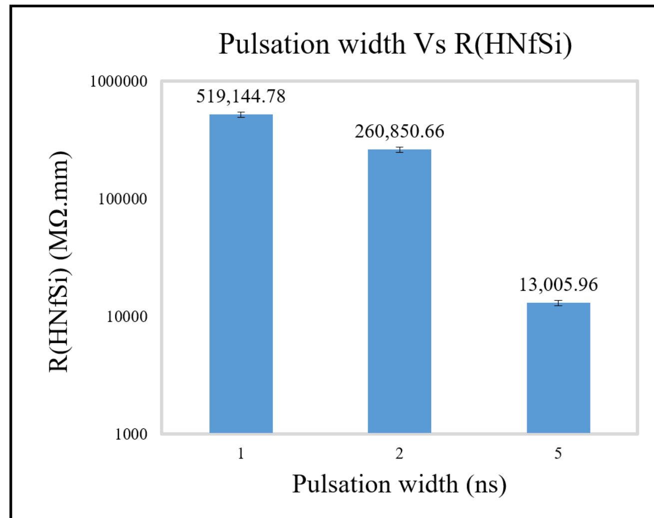

Figure 5.3: Resistivity offered by HNfSi i.e. R(HNfSi) when prepared using laser plasma processing with various pulsation width.

HNfSi, SEM and ImageJ analysis was used. The images captured with SEM analysis is shown in Figure 5.4(I). From the Figure 5.4(I)(c), it is noticeable that with the pulsation width of 5 ns, there is no generation of nano fibers is taking place. This might be because of the less intensive plasma temperature achieved with higher τ values as described before with the help of figure 5.1. As the pulsation width was shorten to 1 ns, the plasma temperature was increased by more than 2 times of what it was with the pulsation width of 5 ns. Such change in plasma temperature might have significant effect on the generation of nano fibers which can be confirmed with Figure 5.4(I)(a) and 5.4(I)(b). From the same figures it is noticed that, relatively more defined and dense nano fibers was achieved when τ value was decreased from 5 ns to 2 ns and then 1 ns. In addition, significant difference was noticed between the nanofibers formed on the HNfSi fabricated with pulsation width of 1 ns and 2 ns. Although in this case, the change in pulsation width is not as large as two extreme limits utilized in experiments, the plasma temperature achieved through pulsation width of 2 ns is significantly lower than that achieved with 1 ns as shown in Figure 5.1. This might be a reason behind difference of the fibrous structure achieved with pulsation width of 1 ns and 2 ns.

To push further the understanding with diverse resistive behavior, ImageJ anal-

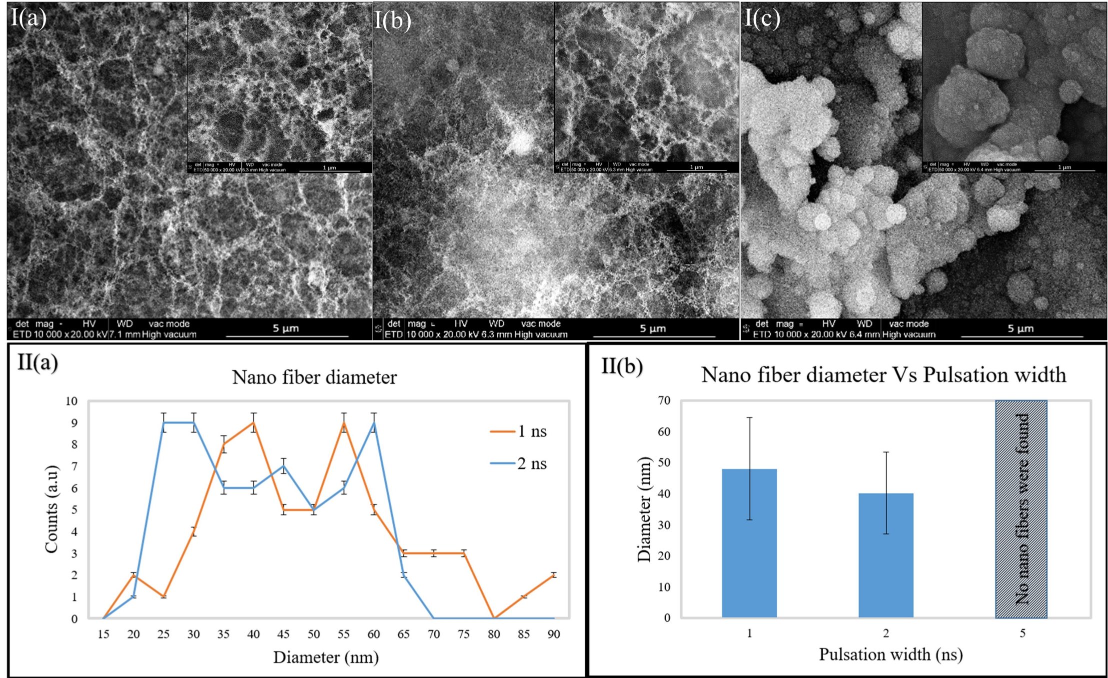

Figure 5.4: (I) SEM images (resolution of 10,000X and 50,000X) of laser plasma processed silicon surface with pulsation width of (a) 1 ns (b) 2 ns and (c) 5 ns. (II) (a) Analysis of nanofibers with available diameter range (b) Change in mean diameter of nanofibers with change in pulsation width.

ysis was employed to understand the effect of pulsation width on available fiber and particle diameters along with the porosity achieved. In addition, these analysis can help analyze the effect of surface area and fabricated geometry on the resistivity offered by HNfSi. As shown in Figure 5.4(II)(a), range of fiber diameter achieved with pulsation width of 2 ns is 20 to 65 nm which decreased to 35 to 65 nm when pulsation width reduced to 1 ns. In addition, mean diameters of nano fibers is increased from $\approx$ 40 nm to $\approx$ 48 nm when pulsation width was elevated from 1 to 2 ns. However, from the visual inspection of Figure 5.4(I)(a) and 5.4(I)(b), it is noticed that the fibers achieved with pulsation width of 1 ns is much more dense and defined. Contrary, HNfSi fabricated with 2 ns has fibers concentrated in several places instead of uniform spread. Hence, fibers achieved with 1 ns pulsation width would have much clear surface to ambient interaction than that achieved with 2 ns value of τ. Furthermore, from ImageJ analysis with similar black and white color intensity, area covered with fibers increased from $\approx$

56% to ≈ 70% when pulsation width decreased from 2 ns to 1 ns.

Considering the laser plasma processing being done under ambient conditions with significantly high temperature achieved at the processing surface, if it assumed that oxidization of nano-fibers and nano-particles are taking place, then the justification of sudden increase in resistivity offered by unit thickness of HNfSi would be quite evident. HNfSi prepared using pulsation width of 1 ns provides surface with defined and dense nano fibers, which offers higher surface area with more electrical insulation in effect because of the oxidization achieved through higher plasma temperature. Such topological condition can raise the thickness based resistance offered by HNfSi to significant level. However, further increase in pulsation width could cause decrement in HNfSi resistivity because of formation of nano fibers with relatively inferior quality which might decrease the surface area and reduced oxidization level caused by relatively lower plasma temperature. In addition, with pulsation width of 5 ns, generated HNfSi does not occupy any nano fibers which results in significantly less surface area along with relatively lower oxygen content which would offer less resistance than that can be gained with the samples prepared with 1 ns and 2 ns of pulsation width.

As mentioned before, the specimen preparation process was done under ambient conditions. Such high temperature achieved at the center of laser spot may causes oxidization of formed structure. Also, depending on the laser and scanning parameter HNfSi can have nanofibers or nano particles and in some cases, combination of both. Ideally, as nano fibers offers much more surface area than nano particles, Oxygen content achieved with nano fibers should be higher than that of attained with nano particles. EDX results from both of the spots having dominating nano fibrous and nano particles structure confirms the significant presence of oxygen as shown in Figure 4.3. In addition, Figure 4.3 confirms that the area with nano fibrous structure has significantly higher oxidation level. The confirmation of availability of oxidation also justifies the effect on resistivity caused by topological conditions offered by nano fibrous and nano particles present in HNfSi. Overall,

results achieved with SEM, ImageJ analysis and EDX tests proves the importance of surface topology and oxidization level in affecting the thickness based resistance offered by HNfSi.

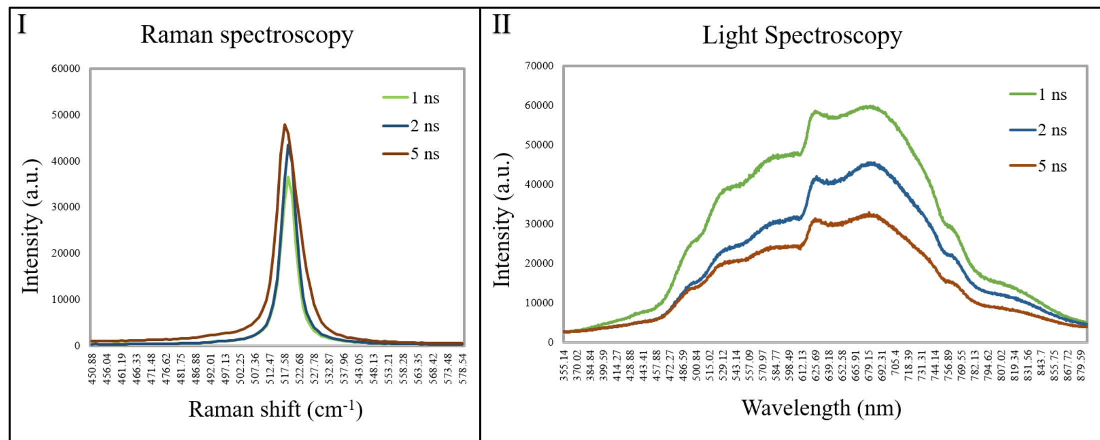

Figure 5.5: (I) Raman spectroscopy and (II) Light spectroscopy results for samples processed with pulsation width of 1 ns, 2 ns and 5 ns.

Considering the surface area offered with nano fibrous structure and nano prticles, interacting surface available for oxidation with ambient atmosphere in each case is different. HNfSi prepared with pulsation width of 1 ns has the highest surface area considering quality of nano fibers present. Hence, it should have highest level of oxidation and least amount of pure silicon present in generated HNfSi. Contrary, samples prepared with pulsation width of 5 ns contains nano particles in generated HNfSi resulting in least surface area available among all three samples for oxidation in ambient atmosphere. Results shown in the Figure 5.5(I) confirms that the available relative amount of pure silicon increases as the pulsation width was varied from 1 ns to 5 ns. It can also be helpful to justify decrease in resistivity offered by HNfSi with increase in pulsation width due to intense presence of silicon which enables HNfSi to be less resistive in case of samples prepared with relatively higher pulsation width.

In addition, light spectroscopy results shown in Figure 5.5(II) shows steady trend of increase in reflective behavior as the pulsation width was varied from 5 ns to 1 ns. For light spectroscopy results, it is important to consider that, with visible range of light, pure silicon (absorption coefficient of 1.84×10^6 cm^{-1} at

250 nm and 300 K [283]) is much less reflective than pure glass (SiO_X) or silica (fused quartz, absorption coefficient of 0.025 cm^{-1} at 250 nm and 300 K [284]). However, it is also essential to consider that pure glass or pure silica does not represent, in order, oxidized nano prticles and fibers or processed silicon material associated with it. It just suggests the possibility of oxidized HNfSi being highly reflective when it has highly oxidized nano particles and nano fibers present on it. Furthermore, considering the surface area offered with nano fibers for samples prepared with shorter pulsation width, HNfSi should have less reflectivity. Instead, HNfSi consisting quality nano fibers offers highest reflectivity which is caused by intense oxidation level present with enhanced surface area. Overall, pulsation width can affect laser plasma temperature significantly resulting in a partially oxidized diverse topology made of nano particles or nano fibers along with variation in T(HNfSi) which can cause immense effect on resistivity offered by HNfSi.

5.3 Variation in leading for surface scanning

Leading is one of the most important parameter for laser plasma processing as it determines the processing time required to prepare HNfSi. Hence, considering the future potential of such inexpensive process to be utilized for large scale fabrication of HNfSi, it is important to understand its effect on HNfSi with respect to its topological properties and electrical characteristics to enable and ease accelerated fabrication. In our study, considering theoretical laser spot diameter of $\approx 29\ \mu$m with employed laser system, the leading has been changed with three steps of 0.0125 mm, 0.025 mm and 0.05 mm to prepare HNfSi which was then further assessed in terms of topological and electrical characteristics. Figure 5.6 depicts relative true scale representation of various leading values and theoretical laser spot size for further comprehension of nature of the process. As it can be seen in Figure 5.6(I) (i.e. Laser spot A and B), with the shortest leading value of 0.0125 mm, multiple processing of the same surface would take place because of the overlap of laser beam over the same surface in short period of time. However,

when the leading value was increased to 0.025 mm, overlap of the laser spot was almost vanished as shown in Figure 5.6(II) (i.e. Laser spot B and C). Furthermore, as depicted in Figure 5.6(III) (i.e. Laser spot C and D), to comprehend effect of partially laser processed surface with higher leading value, the L value of 0.05 mm was employed.

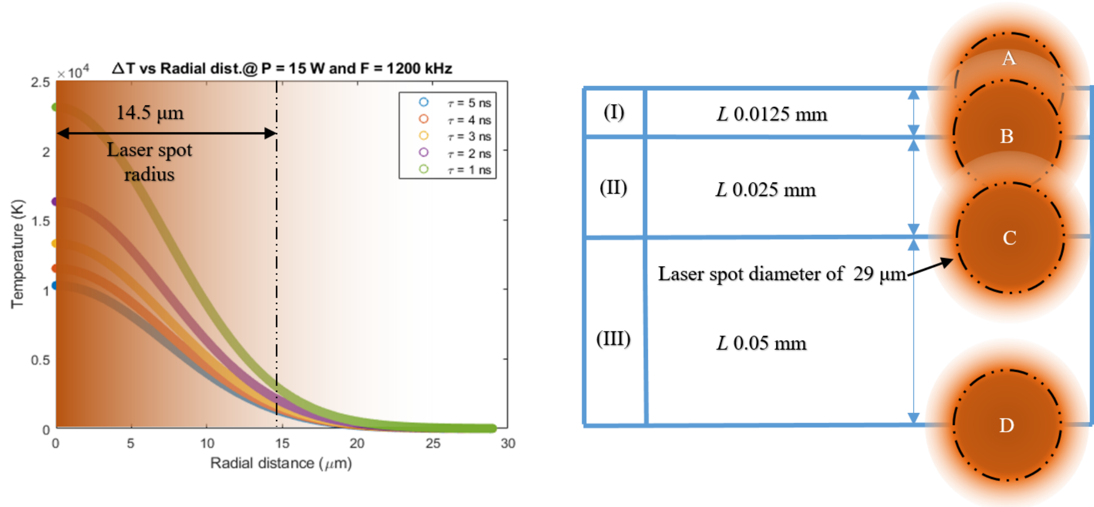

Figure 5.6: Gaussian profile of laser spot with its theoretical radius and three scenarios of laser plasma processing with change in leading values *(L)* of (I) 0.0125 mm, (II) 0.025 mm and (III) 0.05 mm.

To understand the thickness variation with change in leading, optical microscopy was used to capture the cross section as discussed before. As mentioned, with smallest leading value, overlap of material processing takes place. Once processed surface already have a porous structure as discussed in previous section which offers immense surface area with already formed geometry consisting nano entities like nano fibers and nano particles. However, considering significantly short time between consecutive silicon processing which might not be enough for intense oxidation of newly formed HNfSi, successive plasma processing of already processed area can be quite different considering enhanced surface exposure. Naturally, with enhanced surface area, absorption of laser energy should increase which could enable intense plasma processing of already processed surface resulting in a relatively thick HNfSi. In addition, with increase in leading value, the overlap of laser processing vanishes which could be a hindrance in complete plasma ionization

of processed surface resulting in a relatively thin HNfSi.

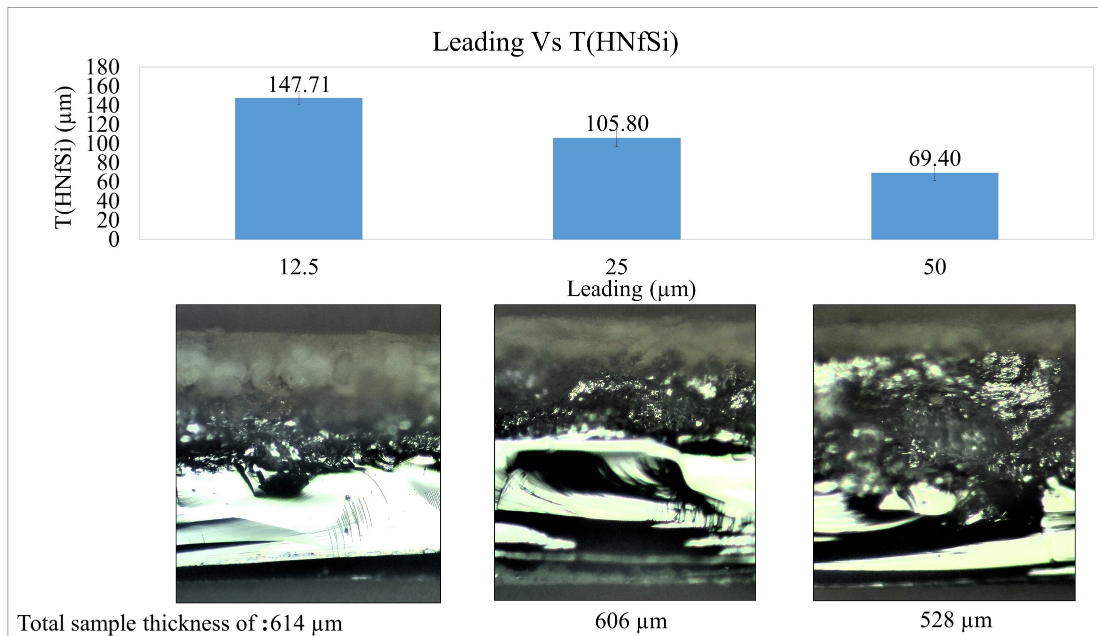

Figure 5.7: Variation in HNfSi thickness i.e T(HNfSi) with change in leading along with cross section image of respective HNfSi.

Figure 5.7 depicts HNfSi thickness analysis for samples prepared with varying leading. From the Figure 5.7, it was noticed that highest thickness of formed HNfSi (i.e. $\approx$ 0.148 mm) was achieved with shortest leading of 0.0125 mm. However, when leading was increased to 0.025 mm, resulting HNfSi held reduced thickness of $\approx$ 0.106 mm. In addition, HNfSi with thickness $\approx$ 0.069 mm was achieved when leading was raised to highest value of 0.05 mm. Such increase in thickness of the formed HNfSi with decrease in leading confirms the extent of laser plasma processing achieved with presence of overlap and importance of extent of area covered while the processing. Furthermore, parallel plate electrode configuration was employed to understand the resistive behavior offered with change in leading. If the material available with HNfSi fabricated using all three leading variants assumed to be same then the resistance offered should increase linearly with raise in HNfSi thickness.

In resistance test, it was found that the thickest HNfSi fabricated using relatively shortest leading did not allow any current to flow through. Higher thickness

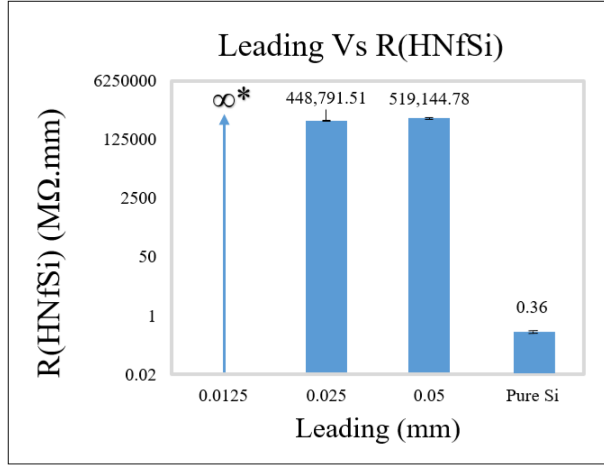

Figure 5.8: Resistivity offered by HNfSi i.e R(HNfSi) when prepared using laser plasma processing with various values of leading. For employed resistivity measuring setup , ∞^* represents highly resistive nature of HNfSi approaching to non-measurable resistivity values when processed with leading value of 0.0125 mm.

of the HNfSi along with presence of available material content might be a cause of immense resistance offered through such thin film. However, as shown in Figure 5.8, with leading of 0.025 mm, fabricated HNfSi was able to let through strong enough electrical signal to measure available resistance. Although, major change in resistance offered by each samples was noticed, when leading was further increased to 0.05 mm, resistivity of HNfSi stayed almost the same. Such behavior indicates the possibility of core structure contributing to the fibrous topology being almost similar. In addition, identical structure could also possess alike optical and topological characteristics. As discussed before in previous section, laser plasma processing being held in ambient conditions could cause oxidation of produced HNfSi up to some extent. In addition, surface area and porosity gained with various HNfSi also affects the resistance offered per unit thickness. Hence, in this case of similar resistive behavior offered by HNfSi when altering leading, thin film topology and oxidation level associated with it might be less distinctive.

As discussed earlier, SEM images of HNfSi were captured to advance understanding on topological characteristics of HNfSi. Figure 5.9(I) depicts SEM images of all three samples prepared with various leading and Figure 5.9(II) concludes topological assessment done using ImageJ analysis for available diameter range and

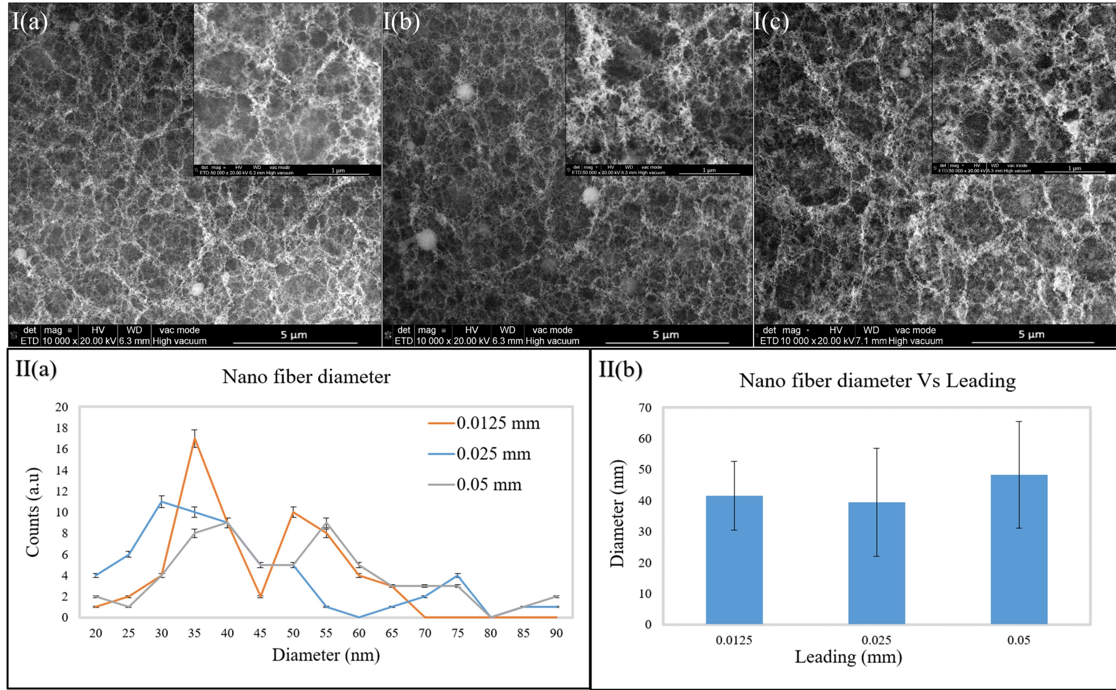

Figure 5.9: (I) SEM images (resolution of 10,000X and 50,000X) of laser plasma processed silicon surface with leading of (a) 0.0125 mm (b) 0.025 mm and (c) 0.05 mm. (II) (a) Analysis of nanofibers with available diameter range (b) Change in mean diameter of nanofibers with change in leading.

mean diameter of nano fibers existing on various HNfSi in interest. From careful analysis of derived data from SEM images, it was found that there is insignificant difference available in terms of achieved mean diameter in all three cases. As we noticed in previous section, topological structure was dominantly affected by change in pulsation width. However, in case of variation in leading, the pulsation width of 1 ns were kept constant. Hence, the laser plasma temperature achieved throughout the surface processing were similar in all three cases which could be a reason for fabrication of similar fibrous topology for all three values of leading.

Furthermore, with the help of ImageJ analysis, the area covered with the fibrous structure on 2D cross section was found to be $\approx$ 70%, 68% and 64% for leading of, in order, 0.0125 mm, 0.025 mm and 0.05 mm. However, the difference for fiber density for leading of 0.0125 mm and 0.025 mm might not be considered as significant as the measurements are purely qualitative. In addition, the trivial difference in fiber density with those two leading instead of relatively larger differ-

ence of the same with case of 0.025 mm and 0.05 mm could be caused because of existence of overlap of plasma processing with leading of 0.0125 mm and 0.025 mm which doesn't exist with leading of 0.05 mm as shown in Figure 5.6. In addition, as discussed before, the same could be the reason for relatively higher thickness achieved in case of shorter leadings and fabrication of thinner HNfSi with relatively larger leading values. Overall, considering topological diversity in terms of present nano fibers and nano particles on HNfSi, effect of variation in leading is not as dominating as the alteration of pulsation width as discussed in previous section. However, effect of leading is significant in terms of variation in thickness achieved by HNfSi with diverse leading values. Considering relatively less intense change in topological structure of HNfSi except achieved thickness, it is important to analyze if there is a significant difference present in terms of achieved oxidation level with variation in leading which could affect the unit thickness based resistance offered by HNfSi.

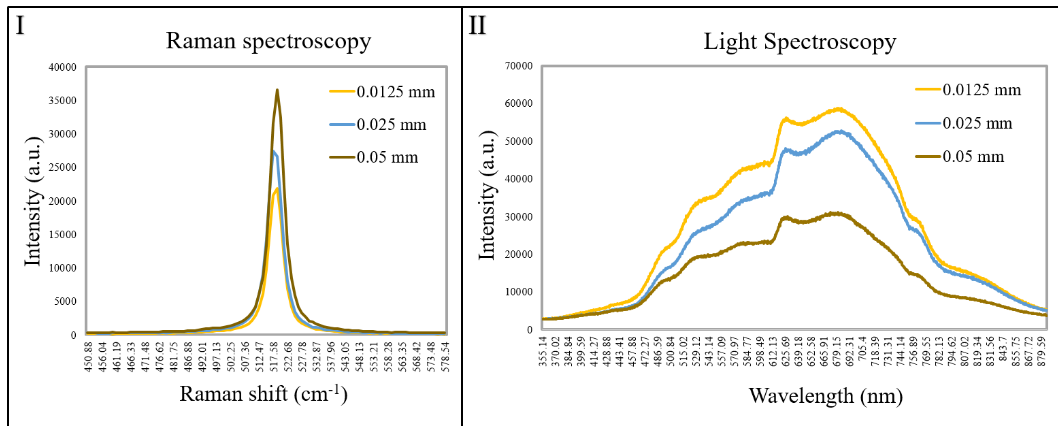

Figure 5.10: (I) Raman spectroscopy and (II) Light spectroscopy results for samples processed with leading values of 0.0125 mm, 0.025 mm and 0.05 mm.

As discussed in previous section, from Raman spectroscopy results and with Raman shift at $\approx 519\ cm^{-1}$, relative content of silicon can be analyzed. Figure 5.10(I) depicts available relative silicon content in all three HNfSi processed with various leading values. Silicon content present on the HNfSi contributes to the ease of resistance offered and also reflective nature of the same. As mentioned earlier, plasma processing being done in ambient conditions, with higher plasma

temperature there could be a possibility of oxidation with enhanced surface area available with nano fibers present on HNfSi. Presence of partially oxidized nano fibers containing SiO_X could be more electrically insulating considering isolating characteristics of SiO_X. Hence, as shown in Figure 5.10(I), relatively lower silicon content with thicker HNfSi achieved with lower leading values confirms existence of higher oxygen content present on the sample due to thicker fibrous layer. Hence, if the similar oxidation level is present on all samples, then oxidized silicon content would deteriorate with decrease in fiber layer thickness causing dominating relative silicon presence on samples; which could be confirmed by Figure 5.10(I) with higher leading values.

In addition, as shown in Figure 5.10(II), light spectroscopy results depicts highly reflective nature of HNfSi processed with relatively lower leading values. As discussed earlier, with insignificant difference available with similar fiber density and fiber diameter, reflectivity offered by HNfSi should be similar. However, results shown in Figure 5.10(II) contradicts the analogy. Considering the difference between absorption coefficient of silicon and SiO_X for visible range of light as discussed in previous section, characteristics of reflectiveness achieved with similar fibrous topology confirms the difference in present content of oxidized silicon in each case with variation in leading values as the thickness of HNfSi varies. Hence, the results achieved with light spectroscopy confirms the increase in oxidized silicon content having similar oxidation level with decrease in leading values enabling HNfSi to attain similar insulating behavior along with increased thin film thickness. Overall, for specific pulsation width, decrease in leading values for plasma processing of silicon surface contributes to fabrication of HNfSi with almost similar fibrous topology with significant variation in T(HNfSi) values along with elevated oxidized silicon enabling highly resistive nature of the fabricated HNfSi.

Chapter 6

Research summary and future work

Overall, with studies done for this project, formation of hybrid nano fibrous structure with several variants were made possible. Also, this study established laser ablation process as an inexpensive and efficient approach for synthesis of nano particle and nano fibrous structure with enough room for variation achieved by changing number of available laser parameters along with resulting fibrous structure itself. Furthermore, literature review done for the project provided significant information on importance of nano structures for sensing applications and how it can affect performance of any given sensor. In addition, it also suggested the possibility of using other nano synthesis methods in combination with laser ablation for further improvements.

To accomplish the goal of employing such structure for the sensing and other electrical applications, it was evident to study the resistive behavior along with surface characterization. Laser parameters used for such study can be segregated in two basic types namely, laser-beam (processing) and scanning parameters. Processing parameters like frequency, power and pulsation width affects the way energy is delivered to the surface along with significant effect on ablation temper-

ature. However, scanning parameters mainly controls the rate of energy delivery along with the extent of process overlap. Our interest to analyze resistive characteristics of HNfSi as a bulk and per unit thickness encouraged us to employ two different measurement setup as described earlier. Overall, most of the laser parameter affected significantly one or other HNfSi characteristics. Identification of intensity of effect on such attributes can be classified within main two HNfSi traits; Surface topology and resistivity.

6.1 Effects on surface topology

There are number of observations can be carried out from the table 6.1.

- Laser parameters like frequency, power and pulsation width affects the topological properties of HNfSi quite significantly than the processing parameters like number of loop and leading.
- In order to change the entity type, that makes up HNfSi, from nano particles to nano fibrous structure, variation in laser parameter can be relatively much more useful.
- At given condition, variation in number of loop can be quite effective to gain denser fibrous structure without much affecting the fiber diameter.
- As noticed, thickness of the fibrous layer is depends more on the scanning parameters than laser parameters. Meaning, variation in ablation conditions and temperature contributes significantly for change in the topological structures rather than the fibrous layer thickness which is affected more by scanning parameters.
- Change in fiber layer thickness without much alteration in fiber density can be achieved by variation in leading values.

Frequency (kHz)	**600**	**800**	**1200**
Structural topology	Nano particles	Hint of fibers with dominating nano particles	Fibrous layer on top of nano particles
≈ *Particle range (nm)*	175-725	175-675	225-975
≈ *Fiber Dia. (nm)*	-	34.7	15.5
≈ *Fiber density(%)*	-	17	42
Power (W)	**10**	**15**	**20**
Structural topology	Nano particles	Fibrous layer on top of nano particles	Fully fibrous
≈ *Particle range (nm)*	175-575	225-975	-
≈ *Fiber Dia. (nm)*	-	15.5	29.2
≈ *Fiber density(%)*	-	42	59
Loop (No.)	**1**	**2**	**3**
Structural topology	Nano fibrous layer on top of nano particles	Segregated fibrous groups	Defined fibers
≈ *Particle range (nm)*	225-975	-	-
≈ *Fiber Dia. (nm)*	15.5	30.2	25.7
≈ *Fiber density(%)*	42	57	61
Pulsation width (ns)	**1**	**2**	**5**
Structural topology	Fully defined fibers	Relatively less denser fibers	Nano particles
≈ *Particle range (nm)*	-	-	320-580
≈ *Fiber Dia. (nm)*	48	40	-
≈ *Fiber density(%)*	76	56	-
≈ *T(HNfSi) μm*	69.4	60.3	45
Leading (mm)	**0.0125**	**0.025**	**0.05**
Structural topology	Fully defined fibers	Fully defined fibers	Fully defined fibers
≈ *Fiber Dia. (nm)*	41.51	39.38	48.26
≈ *Fiber density(%)*	70	68	64
≈ *T(HNfSi) μm*	147.71	105.8	69.4

Table 6.1: Topological characterization of HNfSi with variation of various processing and laser parameters.

6.2 Effects on resistivity

Frequency (kHz)	**Bulk Resistance (kΩ)**
600	1
800	5
1200	37.89
Power (W)	**Bulk Resistance (kΩ)**
10	2
15	37.89
20	74.74
Loops (No.)	**Bulk Resistance (kΩ)**
1	37.89
2	51.44
3	108.11
Pulsation width (ns)	**Resistivity (MΩ.mm)**
1	519144.58
2	260850.66
5	18005.96
Leading (mm)	**Resistivity (MΩ.mm)**
0.0125	∞
0.025	448791.51
0.05	519144.58

Table 6.2: Topological characterization of HNfSi with variation of various processing and laser parameters.

Notable observation made from the achieved results mentioned in table 6.2 are listed below,

- Pulsation width affects the bulk resistance of a formed structure because of change in topology and other potential reasons discussed in previous section. It indicates significance of a formed topology for altering resistive behavior of HNfSi.
- Same as pulsation width, changing of frequency alters the way of energy delivered to the surface causing major change in topological conditions of formed HNfSi, which also contributes to the significant change in bulk resis-

tance of such structure.

- Similar to other laser parameters changing a power affects the ablation temperature significantly causing a major change in a resulting structure, hence contributing to variation in resistive nature of HNfSi.
- Multiple numbers of processing loop can cause significant change in bulk resistance of the structure. Such processing changes the way optical energy is absorbed on the surface after each loop. Resulting structure having a different level of oxidations, even with similar fibrous structure; it provides significantly different resistive behavior with each increased processing loop.
- With increase in HNfSi thickness, variation in leadings contributes to almost similar fibrous structure. Hence, scanning parameter of leading, controlling the extent of process overlap, contributes to significant change in HNfSi thickness without major change in its resistivity.

Overall, from observations of table 6.1 and 6.2, type of surface constituents of generated fibrous structure along with the level of oxidation can be affected significantly by changing the laser parameters like power, frequency and pulsation width. In addition, scanning parameter like leading and leading distance does have relatively minor affect on fibrous topology. However, it can also alter the bulk resistance of the HNfSi significantly depending on the available oxidation level. Also, with respect to change in ablation temperature, process overlap affects the HNfSi thickness quite significantly.

6.3 Future work[4]

As discussed in chapter 6.1 and 6.2, change in resistivity can be caused mainly due to variation in topological properties and oxidation level present on the HNfSi

[4]portion of section 6.3 has been published as conference paper titled 'Synthesis of Graphite Embedded SiO_2 Nanofibers with Controlled Conductivity' in 2018 Photonics North (PN), IEEE https://ieeexplore.ieee.org/document/8438828/.

structure. In different words, using just a laser or scanning parameters, one can not change resistivity of formed HNfSi structure without affecting HNfSi topology and associated oxidation level. In order to change resistive behavior of HNfSi without changing fibrous structure achieved with primary laser processing, inclusion of conductive material is essential. As discussed in chapter 1, methods like ALD and sputtering can be quite useful in terms of irregular or regular deposition of conductive materials like Gold and Graphene on HNfSi.

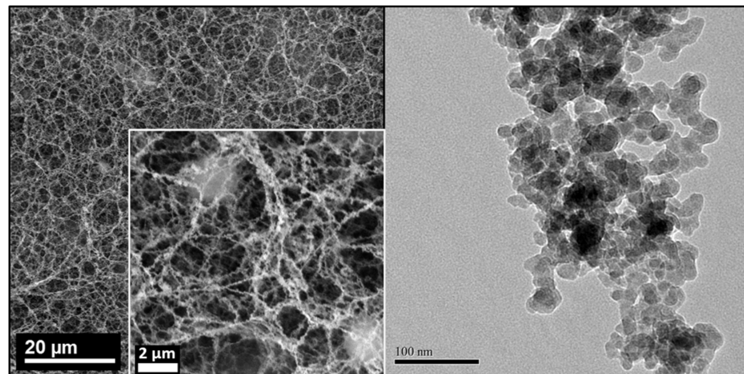

Figure 6.1: SEM and TEM image of HNfSi with Graphite nano particles embedded on it.

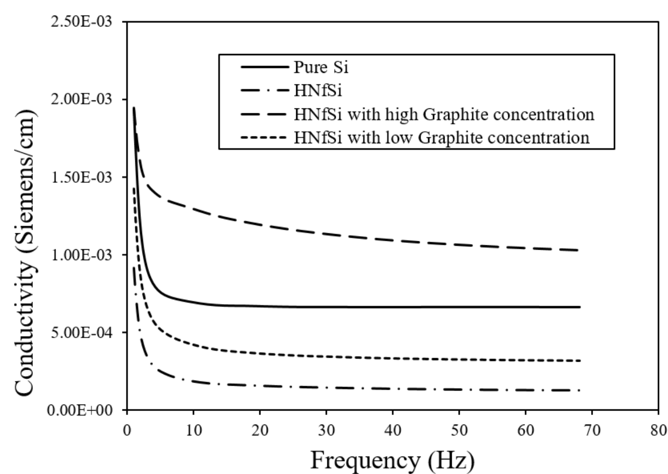

Figure 6.2: Conductivity of Silicon and HNfSi with various concentration of Graphite embedded on it.

Just to confirm the feasibility of such concept, using ND:YAG nano second laser with frequency of 100 kHz and power of 9 W to generate HNfSi, the initial experiment was done where graphite particles was sputtered with same rate for

$\approx$ 4 and 8 minutes on the generated HNfSi structure. SEM and TEM images for such topology with graphite embedded on it can be seen in Figure6.1. As per the observations done before, resistivity of pure HNfSi is quite higher than that of pure Silicon. Hence, inclusion of graphite nano particles should ease the resistive behavior with its higher concentration. Such samples were analyzed using AC impedance spectroscopy in order to determine its relative resistivity. Figure 6.2 depicts successful manipulation of conductivity of a given HNfSi by fusing conductive materials like Graphite.

In addition to potential of HNfSi as a sensing surface, according to our initial results, dense surface area and availability of intense oxidation level with HNfSi can facilitate insulating behavior over large area which can be useful for various photonics devices like optical sensors and emitters. Considering vertical growth in cellular technology and miniaturized devices along with its dependency on effective photonic sensors and receivers, such HNfSi can provide significant advantage to manufacturers in terms of reduced complexity and ease in miniaturization for next generation of surveillance and gesture based cellular devices.

Overall, employing methods like ALD and sputtering, future work can be done to understand effect of inclusion of various conductive nano materials like Gold and Graphene on bulk resistance and resistivity offered by modified HNfSi. Also, potential of such structure can be explored as a sensing surface for numerous applications.

Bibliography

[1] J. Fraden, Handbook of modern sensors: physics, designs, and applications (pp.1-10), Springer Science & Business Media, 2004.

[2] S. Aung, R. Ngim, S. Lee, Evaluation of the laser scanner as a surface measuring tool and its accuracy compared with direct facial anthropometric measurements, British journal of plastic surgery 48 (8) (1995) 551–558.

[3] C. H. Kau, S. Richmond, A. I. Zhurov, J. Knox, I. Chestnutt, F. Hartles, R. Playle, Reliability of measuring facial morphology with a 3-dimensional laser scanning system, American Journal of Orthodontics and Dentofacial Orthopedics 128 (4) (2005) 424–430.

[4] J. Li, J. Liang, L. Li, F. Ren, W. Hu, J. Li, S. Qi, Q. Pei, Healable capacitive touch screen sensors based on transparent composite electrodes comprising silver nanowires and a furan/maleimide diels–alder cycloaddition polymer, ACS nano 8 (12) (2014) 12874–12882.

[5] T. Mochizuki, Y. Takigami, T. Kondo, H. Okuzaki, Fabrication of flexible transparent electrodes using pedot: Pss and application to resistive touch screen panels, Journal of Applied Polymer Science 135 (10) (2018) 45972.

[6] K. Bethe, The scope of the strain gage principle, in: CompEuro'89.,'VLSI and Computer Peripherals. VLSI and Microelectronic Applications in Intelligent Peripherals and their Interconnection Networks', Proceedings., IEEE, 1989, pp. 3–31.

[7] B. Noroozi, B. I. Morshed, Psc optimization of 13.56-mhz resistive wireless analog passive sensors, IEEE Transactions on Microwave Theory and Techniques.

[8] D.-I. E. G. Gautschi, Piezoelectric sensors, in: Piezoelectric Sensorics, Springer, 2002, pp. 73–91.

[9] V. Baier, R. Födisch, A. Ihring, E. Kessler, J. Lerchner, G. Wolf, J. Köhler, M. Nietzsch, M. Krügel, Highly sensitive thermopile heat power sensor for micro-fluid calorimetry of biochemical processes, Sensors and Actuators A: Physical 123 (2005) 354–359.

[10] L. Lescouzeres, A. Lorenzo, E. Scheid, Semiconductor chemical sensor device and method of forming a thermocouple for a semiconductor chemical sensor device, uS Patent 5,879,630 (Mar. 9 1999).

[11] J. Wrachtrup, A. Finkler, Applied physics: Hybrid sensors ring the changes, Nature 512 (7515) (2014) 380–381.

[12] W. J. Fleming, Overview of automotive sensors, IEEE sensors journal 1 (4) (2001) 296–308.

[13] W. P. Eaton, J. H. Smith, Micromachined pressure sensors: review and recent developments, Smart Materials and Structures 6 (5) (1997) 530.

[14] D. Ding, R. A. Cooper, P. F. Pasquina, L. Fici-Pasquina, Sensor technology for smart homes, Maturitas 69 (2) (2011) 131–136.

[15] F.-C. Huang, Y.-Y. Chen, T.-T. Wu, A room temperature surface acoustic wave hydrogen sensor with pt coated zno nanorods, Nanotechnology 20 (6) (2009) 065501.

[16] X. Huang, D. Zhang, A high sensitivity and high linearity pressure sensor based on a peninsula-structured diaphragm for low-pressure ranges, Sensors and Actuators A: Physical 216 (2014) 176–189.

[17] S. Marco, J. Samitier, O. Ruiz, J. Morante, J. Esteve, High-performance piezoresistive pressure sensors for biomedical applications using very thin structured membranes, Measurement science and technology 7 (9) (1996) 1195.

[18] S. Aravamudhan, S. Bhansali, Reinforced piezoresistive pressure sensor for ocean depth measurements, Sensors and Actuators A: Physical 142 (1) (2008) 111–117.

[19] Y. Zhang, K. Yu, D. Jiang, Z. Zhu, H. Geng, L. Luo, Zinc oxide nanorod and nanowire for humidity sensor, Applied Surface Science 242 (1) (2005) 212–217.

[20] P.-G. Su, W.-Y. Tsai, Humidity sensing and electrical properties of a composite material of nano-sized sio 2 and poly (2-acrylamido-2-methylpropane sulfonate), Sensors and Actuators B: Chemical 100 (3) (2004) 417–422.

[21] X. Wang, B. Ding, J. Yu, M. Wang, F. Pan, A highly sensitive humidity sensor based on a nanofibrous membrane coated quartz crystal microbalance, Nanotechnology 21 (5) (2009) 055502.

[22] Y. Sakai, Y. Sadaoka, M. Matsuguchi, Humidity sensors based on polymer thin films, Sensors and Actuators B: Chemical 35 (1-3) (1996) 85–90.

[23] Y. Paska, H. Haick, Interactive effect of hysteresis and surface chemistry on gated silicon nanowire gas sensors, ACS applied materials & interfaces 4 (5) (2012) 2604–2617.

[24] W. Geng, Q. Yuan, X. Jiang, J. Tu, L. Duan, J. Gu, Q. Zhang, Humidity sensing mechanism of mesoporous mgo/kcl–sio 2 composites analyzed by complex impedance spectra and bode diagrams, Sensors and Actuators B: Chemical 174 (2012) 513–520.

[25] R.-J. Wu, Y.-L. Sun, C.-C. Lin, H.-W. Chen, M. Chavali, Composite of tio 2 nanowires and nafion as humidity sensor material, Sensors and Actuators B: Chemical 115 (1) (2006) 198–204.

[26] T. Helbling, C. Hierold, L. Durrer, C. Roman, R. Pohle, M. Fleischer, Suspended and non-suspended carbon nanotube transistors for no2 sensing–a qualitative comparison, physica status solidi (b) 245 (10) (2008) 2326–2330.

[27] J. Nygård, D. H. Cobden, Quantum dots in suspended single-wall carbon nanotubes, Applied Physics Letters 79 (25) (2001) 4216–4218.

[28] J. Cao, Q. Wang, D. Wang, H. Dai, Suspended carbon nanotube quantum wires with two gates, Small 1 (1) (2005) 138–141.

[29] M. Muoth, T. Helbling, L. Durrer, S.-W. Lee, C. Roman, C. Hierold, Hysteresis-free operation of suspended carbon nanotube transistors, Nature Nanotechnology 5 (8) (2010) 589–592.

[30] S. Kim, T. Nam, S. Park, Measurement of flow direction and velocity using a micromachined flow sensor, Sensors and Actuators A: Physical 114 (2) (2004) 312–318.

[31] Y.-H. Wang, C.-Y. Lee, C.-M. Chiang, A mems-based air flow sensor with a free-standing micro-cantilever structure, Sensors 7 (10) (2007) 2389–2401.

[32] A. S. Cubukcu, E. Zernickel, U. Buerklin, G. A. Urban, A 2d thermal flow sensor with sub-mw power consumption, Sensors and Actuators A: Physical 163 (2) (2010) 449–456.

[33] A. Gao, N. Zou, P. Dai, N. Lu, T. Li, Y. Wang, J. Zhao, H. Mao, Signal-to-noise ratio enhancement of silicon nanowires biosensor with rolling circle amplification, Nano letters 13 (9) (2013) 4123–4130.

[34] M. David-Pur, L. Bareket-Keren, G. Beit-Yaakov, D. Raz-Prag, Y. Hanein, All-carbon-nanotube flexible multi-electrode array for neuronal recording and stimulation, Biomedical microdevices 16 (1) (2014) 43–53.

[35] V. Valev, A. Silhanek, N. Verellen, W. Gillijns, P. Van Dorpe, O. Aktsipetrov, G. Vandenbosch, V. Moshchalkov, T. Verbiest, Asymmetric optical second-harmonic generation from chiral g-shaped gold nanostructures, Physical review letters 104 (12) (2010) 127401.

[36] G. Baranauskas, E. Maggiolini, E. Castagnola, A. Ansaldo, A. Mazzoni, G. N. Angotzi, A. Vato, D. Ricci, S. Panzeri, L. Fadiga, Carbon nanotube composite coating of neural microelectrodes preferentially improves the multiunit signal-to-noise ratio, Journal of neural engineering 8 (6) (2011) 066013.

[37] Y. Mu, D. Jia, Y. He, Y. Miao, H.-L. Wu, Nano nickel oxide modified nonenzymatic glucose sensors with enhanced sensitivity through an electrochemical process strategy at high potential, Biosensors and Bioelectronics 26 (6) (2011) 2948–2952.

[38] K. Chikkadi, M. Muoth, W. Liu, V. Maiwald, C. Hierold, Enhanced signal-to-noise ratio in pristine, suspended carbon nanotube gas sensors, Sensors and Actuators B: Chemical 196 (2014) 682–690.

[39] J. Jiang, T. Liu, K. Liu, S. Wang, J. Yin, B. Zhao, J. Zhang, L. Song, P. Zhao, F. Wu, et al., Development of optical fiber sensing instrument for aviation and aerospace application, in: 2013 International Conference on Optical Instruments and Technology: Optical Sensors and Applications, Vol. 9044, International Society for Optics and Photonics, 2013, p. 90440K.

[40] M. de Vries, V. Arya, S. Meller, S. F. Masri, R. O. Claus, Implementation of efpi-based optical-fiber sensor instrumentation for the nde of concrete structures, Cement and concrete composites 19 (1) (1997) 69–79.

[41] R. Fan, M. Ebrahimi, H. Quitmann, P. Czermak, Lactic acid production in a membrane bioctor system with thermophilic bacillus coagulans: Fouling analysis of the used ceramic membranes, Separation Science and Technology 50 (14) (2015) 2177–2189.

[42] J. Haus, Optical Sensors (pp.1-18), Wiley Online Library, 2010.

[43] J. M. Bedlek-Anslow, J. P. Hubner, B. F. Carroll, K. S. Schanze, Micro-heterogeneous oxygen response in luminescence sensor films, Langmuir 16 (24) (2000) 9137–9141.

[44] Y. Mao, Y. Gao, S. Wu, S. Wu, J. Shi, B. Zhou, Y. Tian, Highly enhanced sensitivity of optical oxygen sensors using microstructured pttfpp/pdms-pillar arrays sensing layer, Sensors and Actuators B: Chemical 251 (2017) 495–502.

[45] R. Xue, C. Ge, K. Richardson, A. Palmer, M. Viapiano, J. J. Lannutti, Microscale sensing of oxygen via encapsulated porphyrin nanofibers: Effect of indicator and polymer core permeability, ACS applied materials & interfaces 7 (16) (2015) 8606–8614.

[46] R. Verma, B. D. Gupta, Detection of heavy metal ions in contaminated water by surface plasmon resonance based optical fibre sensor using conducting polymer and chitosan, Food chemistry 166 (2015) 568–575.

[47] T. Balaji, S. A. El-Safty, H. Matsunaga, T. Hanaoka, F. Mizukami, Optical sensors based on nanostructured cage materials for the detection of toxic metal ions, Angewandte Chemie 118 (43) (2006) 7360–7366.

[48] P. Gründler, Chemical sensors: an introduction for scientists and engineers (pp.1-12), Springer Science & Business Media, 2007.

[49] D. James, S. M. Scott, Z. Ali, W. T. Ohare, Chemical sensors for electronic nose systems, Microchimica Acta 149 (1) (2005) 1–17.

[50] C. K. Ho, M. T. Itamura, M. Kelley, R. C. Hughes, et al., Review of chemical sensors for in-situ monitoring of volatile contaminants, Sandia Report SAND2001-0643, Sandia National Laboratories (2001) 1–27.

[51] F. Schedin, A. Geim, S. Morozov, E. Hill, P. Blake, M. Katsnelson, K. Novoselov, Detection of individual gas molecules adsorbed on graphene, Nature materials 6 (9) (2007) 652.

[52] G. F. Fine, L. M. Cavanagh, A. Afonja, R. Binions, Metal oxide semiconductor gas sensors in environmental monitoring, Sensors 10 (6) (2010) 5469–5502.

[53] J. Müller, S. Weissenrieder, Zno-thin film chemical sensors, Fresenius' journal of analytical chemistry 349 (5) (1994) 380–384.

[54] T. Krishnakumar, R. Jayaprakash, N. Pinna, N. Donato, A. Bonavita, G. Micali, G. Neri, Co gas sensing of zno nanostructures synthesized by an assisted microwave wet chemical route, Sensors and Actuators B: Chemical 143 (1) (2009) 198–204.

[55] C.-Y. Liu, C.-F. Chen, J.-P. Leu, Fabrication and co sensing properties of mesostructured zno gas sensors, Journal of The Electrochemical Society 156 (1) (2009) J16–J19.

[56] J. Wang, X. Sun, H. Huang, Y. Lee, O. Tan, M. Yu, G. Lo, D. Kwong, A two-step hydrothermally grown zno microtube array for co gas sensing., Applied Physics A: Materials Science & Processing 88 (4).

[57] A. Tamvakos, D. Calestani, D. Tamvakos, D. Pullini, M. Sgroi, A. Pruna, Low concentration co gas sensing properties of hybrid zno architecture, Microelectronic Engineering 160 (2016) 12–17.

[58] J. Xu, Q. Pan, Z. Tian, et al., Grain size control and gas sensing properties of zno gas sensor, Sensors and Actuators B: Chemical 66 (1-3) (2000) 277–279.

[59] S. Arunkumar, T. Hou, Y.-B. Kim, B. Choi, S. H. Park, S. Jung, D.-W. Lee, Au decorated zno hierarchical architectures: Facile synthesis, tunable morphology and enhanced co detection at room temperature, Sensors and Actuators B: Chemical 243 (2017) 990–1001.

[60] S.-J. Chang, T.-J. Hsueh, I.-C. Chen, B.-R. Huang, Highly sensitive zno nanowire co sensors with the adsorption of au nanoparticles, Nanotechnology 19 (17) (2008) 175502.

[61] M. Hjiri, R. Dhahri, L. El Mir, A. Bonavita, N. Donato, S. Leonardi, G. Neri, Co sensing properties of ga-doped zno prepared by sol–gel route, Journal of Alloys and Compounds 634 (2015) 187–192.

[62] N. Le Hung, H. Kim, S.-K. Hong, D. Kim, Enhancement of co gas sensing properties in zno thin films deposited on self-assembled au nanodots, Sensors and Actuators B: Chemical 151 (1) (2010) 127–132.

[63] S.-W. Choi, S. S. Kim, Room temperature co sensing of selectively grown networked zno nanowires by pd nanodot functionalization, Sensors and Actuators B: Chemical 168 (2012) 8–13.

[64] H. Gong, J. Hu, J. Wang, C. Ong, F. Zhu, Nano-crystalline cu-doped zno thin film gas sensor for co, Sensors and Actuators B: Chemical 115 (1) (2006) 247–251.

[65] T. Tagawa, T. Tamura, P. A. Oberg, Biomedical sensors and instruments (pp.1-17,283).

[66] M. Engin, A. Demirel, E. Z. Engin, M. Fedakar, Recent developments and trends in biomedical sensors, Measurement 37 (2) (2005) 173–188.

[67] A. Yakovlev, S. Kim, A. Poon, Implantable biomedical devices: Wireless powering and communication, IEEE Communications Magazine 50 (4).

[68] T. A. Rocha-Santos, Sensors and biosensors based on magnetic nanoparticles, TrAC Trends in Analytical Chemistry 62 (2014) 28–36.

[69] J. Llandro, J. Palfreyman, A. Ionescu, C. Barnes, Magnetic biosensor technologies for medical applications: a review, Medical & biological engineering & computing 48 (10) (2010) 977–998.

[70] J. Ponmozhi, C. Frias, T. Marques, O. Frazão, Smart sensors/actuators for biomedical applications, Measurement 45 (7) (2012) 1675–1688.

[71] J. A. Garrido-Cardenas, F. Garcia-Maroto, J. A. Alvarez-Bermejo, F. Manzano-Agugliaro, Dna sequencing sensors: an overview, Sensors 17 (3) (2017) 588.

[72] P. Xie, Q. Xiong, Y. Fang, Q. Qing, C. M. Lieber, Local electrical potential detection of dna by nanowire-nanopore sensors, Nature nanotechnology 7 (2) (2012) 119–125.

[73] G. F. Schneider, S. W. Kowalczyk, V. E. Calado, G. Pandraud, H. W. Zandbergen, L. M. Vandersypen, C. Dekker, Dna translocation through graphene nanopores, Nano letters 10 (8) (2010) 3163–3167.

[74] J. Lagerqvist, M. Zwolak, M. Di Ventra, Fast dna sequencing via transverse electronic transport, Nano letters 6 (4) (2006) 779–782.

[75] J.-i. Hahm, C. M. Lieber, Direct ultrasensitive electrical detection of dna and dna sequence variations using nanowire nanosensors, Nano letters 4 (1) (2004) 51–54.

[76] I. M. Derrington, T. Z. Butler, M. D. Collins, E. Manrao, M. Pavlenok, M. Niederweis, J. H. Gundlach, Nanopore dna sequencing with mspa, Proceedings of the National Academy of Sciences 107 (37) (2010) 16060–16065.

[77] O. Syshchyk, V. A. Skryshevsky, O. O. Soldatkin, A. P. Soldatkin, Enzyme biosensor systems based on porous silicon photoluminescence for detection

of glucose, urea and heavy metals, Biosensors and Bioelectronics 66 (2015) 89–94.

[78] M. Pumera, S. Sanchez, I. Ichinose, J. Tang, Electrochemical nanobiosensors, Sensors and Actuators B: Chemical 123 (2) (2007) 1195–1205.

[79] Y. Zhou, L. Tang, G. Zeng, C. Zhang, Y. Zhang, X. Xie, Current progress in biosensors for heavy metal ions based on dnazymes/dna molecules functionalized nanostructures: A review, Sensors and Actuators B: Chemical 223 (2016) 280–294.

[80] B. Munge, G. Liu, G. Collins, J. Wang, Multiple enzyme layers on carbon nanotubes for electrochemical detection down to 80 dna copies, Analytical chemistry 77 (14) (2005) 4662–4666.

[81] K.-I. Chen, B.-R. Li, Y.-T. Chen, Silicon nanowire field-effect transistor-based biosensors for biomedical diagnosis and cellular recording investigation, Nano Today 6 (2) (2011) 131–154.

[82] K. Xu, J. Huang, Z. Ye, Y. Ying, Y. Li, Recent development of nano-materials used in dna biosensors, Sensors 9 (7) (2009) 5534–5557.

[83] J. Maze, P. Stanwix, J. Hodges, S. Hong, J. Taylor, P. Cappellaro, L. Jiang, M. G. Dutt, E. Togan, A. Zibrov, et al., Nanoscale magnetic sensing with an individual electronic spin in diamond, Nature 455 (7213) (2008) 644–647.

[84] I. Heller, J. Mannik, S. G. Lemay, C. Dekker, Optimizing the signal-to-noise ratio for biosensing with carbon nanotube transistors, Nano letters 9 (1) (2008) 377–382.

[85] N.-C. Tsai, C.-Y. Sue, Review of mems-based drug delivery and dosing systems, Sensors and Actuators A: Physical 134 (2) (2007) 555–564.

[86] H.-J. Kim, S.-S. Yoo, D.-E. Kim, Nano-scale wear: a review, International Journal of Precision Engineering and Manufacturing 13 (9) (2012) 1709–1718.

[87] S. H. Kim, D. B. Asay, M. T. Dugger, Nanotribology and mems, Nano today 2 (5) (2007) 22–29.

[88] F.-C. Huang, Y.-Y. Chen, T.-T. Wu, A room temperature surface acoustic wave hydrogen sensor with pt coated zno nanorods, Nanotechnology 20 (6) (2009) 065501.

[89] G. Zhang, Nanostructure-enhanced surface acoustic waves biosensor and its computational modeling, journal of Sensors 2009.

[90] C. Pramanik, H. Saha, Piezoresistive pressure sensing by porous silicon membrane, IEEE Sensors Journal 6 (2) (2006) 301–309.

[91] S. Hamza, A. Kiani, A rapid and easy procedure of conductive 3d nanofibrous structure induced by nanosecond laser processing of si wafer coated by au thin-film, Sensing and Bio-Sensing Research 16 (2017) 6–11.

[92] S. Hamza, A. Ignaszak, A. Kiani, Synthesis of electrical conductive silica nanofiber/gold nanoparticle composite by laser pulses and sputtering technique, Nanoscale research letters 12 (1) (2017) 432.

[93] M. Ramuz, B. C.-K. Tee, J. B.-H. Tok, Z. Bao, Transparent, optical, pressure-sensitive artificial skin for large-area stretchable electronics, Advanced Materials 24 (24) (2012) 3223–3227.

[94] S. Nanot, A. W. Cummings, C. L. Pint, A. Ikeuchi, T. Akiho, K. Sueoka, R. H. Hauge, F. Léonard, J. Kono, Broadband, polarization-sensitive photodetector based on optically-thick films of macroscopically long, dense, and aligned carbon nanotubes, Scientific reports 3.

[95] B. C. St-Antoine, D. Ménard, R. Martel, Single-walled carbon nanotube thermopile for broadband light detection, Nano letters 11 (2) (2010) 609–613.

[96] Z. Zhong, N. M. Gabor, J. E. Sharping, A. L. Gaeta, P. L. McEuen, Terahertz time-domain measurement of ballistic electron resonance in a single-walled carbon nanotube, Nature nanotechnology 3 (4) (2008) 201–205.

[97] L. Prechtel, L. Song, S. Manus, D. Schuh, W. Wegscheider, A. W. Holleitner, Time-resolved picosecond photocurrents in contacted carbon nanotubes, Nano letters 11 (1) (2010) 269–272.

[98] A. Pimpin, W. Srituravanich, Review on micro-and nanolithography techniques and their applications, Engineering Journal 16 (1) (2012) 37.

[99] R. Maeda, M. Takahashi, S. Sasaki, Commercialization of mems and nano manufacturing, in: Polymers and Adhesives in Microelectronics and Photonics, 2007. Polytronic 2007. 6th International Conference on, IEEE, 2007, pp. 20–23.

[100] D. W. Hobson, Commercialization of nanotechnology, Wiley Interdisciplinary Reviews: Nanomedicine and Nanobiotechnology 1 (2) (2009) 189–202.

[101] M. Stepanova, S. Dew, Nanofabrication: techniques and principles (pp.3-7), Springer Science & Business Media, 2011.

[102] A. m Hind, A history of engraving and etching (p.7), Constable, 1923.

[103] O. Çakır, Chemical etching of aluminium, Journal of materials processing technology 199 (1) (2008) 337–340.

[104] H. Zhu, M. Holl, T. Ray, S. Bhushan, D. R. Meldrum, Characterization of deep wet etching of fused silica glass for single cell and optical sensor

deposition, Journal of Micromechanics and Microengineering 19 (6) (2009) 065013.

[105] D. C. Abeysinghe, S. Dasgupta, J. T. Boyd, H. E. Jackson, A novel mems pressure sensor fabricated on an optical fiber, IEEE Photonics Technology Letters 13 (9) (2001) 993–995.

[106] M.-H. Tsai, C.-M. Sun, Y.-C. Liu, C. Wang, W. Fang, Design and application of a metal wet-etching post-process for the improvement of cmos-mems capacitive sensors, Journal of Micromechanics and Microengineering 19 (10) (2009) 105017.

[107] J. Fields, C. Asawa, O. Ramer, M. Barnoski, Fiber optic pressure sensor, The Journal of the Acoustical Society of America 67 (3) (1980) 816–818.

[108] J. P. Ingold, M. H. Sun, R. N. Bigelow, Fiber optic pressure sensor, in: Specialty Fiber Optic Systems for Mobile Platforms, Vol. 1589, International Society for Optics and Photonics, 1991, pp. 83–90.

[109] D. C. Abeysinghe, S. Dasgupta, J. T. Boyd, H. E. Jackson, A novel mems pressure sensor fabricated on an optical fiber, IEEE Photonics Technology Letters 13 (9) (2001) 993–995.

[110] Y. Zhu, A. Wang, Miniature fiber-optic pressure sensor, IEEE Photonics Technology Letters 17 (2) (2005) 447–449.

[111] Z. Li, C. Liao, Y. Wang, L. Xu, D. Wang, X. Dong, S. Liu, Q. Wang, K. Yang, J. Zhou, Highly-sensitive gas pressure sensor using twin-core fiber based in-line mach-zehnder interferometer, Optics express 23 (5) (2015) 6673–6678.

[112] S. Liu, Y. Wang, C. Liao, Y. Wang, J. He, C. Fu, K. Yang, Z. Bai, F. Zhang, Nano silica diaphragm in-fiber cavity for gas pressure measurement, Scientific Reports 7 (1) (2017) 787.

[113] N. A. Smith, J. E. Evans, D. R. Jones, A. M. Lord, S. Wilks, Growth of zno nanowire arrays directly onto si via substrate topographical adjustments using both wet chemical and dry etching methods, Materials Science and Engineering: B 193 (2015) 41–48.

[114] S. J. Pearton, D. P. Norton, Dry etching of electronic oxides, polymers, and semiconductors, Plasma Processes and Polymers 2 (1) (2005) 16–37.

[115] M. Takahashi, K. Sugimoto, R. Maeda, Nanoimprint of glass materials with glassy carbon molds fabricated by focused-ion-beam etching, Japanese Journal of Applied Physics 44 (7S) (2005) 5600.

[116] M.-F. Chen, Y.-P. Chen, W.-T. Hsiao, Z.-P. Gu, Laser direct write patterning technique of indium tin oxide film, Thin Solid Films 515 (24) (2007) 8515–8518.

[117] J. C. Cheng, A. P. Pisano, Photolithographic process for integration of the biopolymer chitosan into micro/nanostructures, Journal of Microelectromechanical Systems 17 (2) (2008) 402–409.

[118] C. Zamponi, H. Rumpf, C. Schmutz, E. Quandt, Structuring of sputtered superelastic niti thin films by photolithography and etching, Materials Science and Engineering: A 481 (2008) 623–625.

[119] N. Lucas, S. Demming, A. Jordan, P. Sichler, S. Büttgenbach, An improved method for double-sided moulding of pdms, Journal of Micromechanics and Microengineering 18 (7) (2008) 075037.

[120] C. Iliescu, K. L. Tan, F. E. Tay, J. Miao, Deep wet and dry etching of pyrex glass: A review, in: Proceedings of the International Conference on Materials for Advanced Technologies (ICMAT), Singapore, 2005, pp. 3–7.

[121] C. Iliescu, J. Miao, F. E. Tay, Stress control in masking layers for deep wet micromachining of pyrex glass, Sensors and Actuators A: Physical 117 (2) (2005) 286–292.

[122] B. Wu, A. Kumar, S. Pamarthy, High aspect ratio silicon etch: A review, Journal of applied physics 108 (5) (2010) 9.

[123] W.-T. Tsai, H.-P. Chen, W.-Y. Hsien, A review of uses, environmental hazards and recovery/recycle technologies of perfluorocarbons (pfcs) emissions from the semiconductor manufacturing processes, Journal of Loss Prevention in the Process Industries 15 (2) (2002) 65–75.

[124] L. Francioso, A. Taurino, A. Forleo, P. Siciliano, Tio 2 nanowires array fabrication and gas sensing properties, Sensors and Actuators B: Chemical 130 (1) (2008) 70–76.

[125] M. Epifani, A. Helwig, J. Arbiol, R. Díaz, L. Francioso, P. Siciliano, G. Mueller, J. R. Morante, Tio 2 thin films from titanium butoxide: synthesis, pt addition, structural stability, microelectronic processing and gas-sensing properties, Sensors and Actuators B: Chemical 130 (2) (2008) 599–608.

[126] C.-C. Lu, Y.-S. Huang, J.-W. Huang, C.-K. Chang, S.-P. Wu, A macroporous tio2 oxygen sensor fabricated using anodic aluminium oxide as an etching mask, Sensors 10 (1) (2010) 670–683.

[127] C. Lee, S. Y. Bae, S. Mobasser, H. Manohara, A novel silicon nanotips antireflection surface for the micro sun sensor, Nano letters 5 (12) (2005) 2438–2442.

[128] Y. P. Zhang, D. Liu, Antenna-on-chip and antenna-in-package solutions to highly integrated millimeter-wave devices for wireless communications, IEEE Transactions on Antennas and Propagation 57 (10) (2009) 2830–2841.

[129] W.-C. Tian, J. Weigold, S. Pang, Comparison of cl 2 and f-based dry etching for high aspect ratio si microstructures etched with an inductively coupled plasma source, Journal of Vacuum Science & Technology B: Microelectronics

and Nanometer Structures Processing, Measurement, and Phenomena 18 (4) (2000) 1890–1896.

[130] M. Alavi, S. Büttgenbach, A. Schumacher, H.-J. Wagner, Fabrication of microchannels by laser machining and anisotropic etching of silicon, Sensors and Actuators A: Physical 32 (1-3) (1992) 299–302.

[131] Y. Zhou, Q. Bao, B. Varghese, L. A. L. Tang, C. K. Tan, C.-H. Sow, K. P. Loh, Microstructuring of graphene oxide nanosheets using direct laser writing, Advanced Materials 22 (1) (2010) 67–71.

[132] N. Marrero, R. Guerrero-Lemus, B. González-Díaz, D. Borchert, Effect of porous silicon stain etched on large area alkaline textured crystalline silicon solar cells, Thin solid films 517 (8) (2009) 2648–2650.

[133] A. V. Sapelkin, S. C. Bayliss, B. Unal, A. Charalambou, Interaction of b50 rat hippocampal cells with stain-etched porous silicon, Biomaterials 27 (6) (2006) 842–846.

[134] M. Frost, M. E. Meyerhoff, In vivo chemical sensors: tackling biocompatibility (2006).

[135] C. R. Becker, S. Apperson, C. J. Morris, S. Gangopadhyay, L. J. Currano, W. A. Churaman, C. R. Stoldt, Galvanic porous silicon composites for high-velocity nanoenergetics, Nano letters 11 (2) (2010) 803–807.

[136] J. Yoo, G. Yu, J. Yi, Large-area multicrystalline silicon solar cell fabrication using reactive ion etching (rie), Solar Energy Materials and Solar Cells 95 (1) (2011) 2–6.

[137] P. Papet, O. Nichiporuk, A. Kaminski, Y. Rozier, J. Kraiem, J.-F. Lelievre, A. Chaumartin, A. Fave, M. Lemiti, Pyramidal texturing of silicon solar cell with tmah chemical anisotropic etching, Solar Energy Materials and Solar Cells 90 (15) (2006) 2319–2328.

[138] D. Z. Dimitrov, C.-H. Du, Crystalline silicon solar cells with micro/nano texture, Applied Surface Science 266 (2013) 1–4.

[139] F. Rustamov, N. Darvishov, V. Bagiev, M. Mamedov, E. Bobrova, H. Qafarova, Influence of final treatment on the incubation period and antireflection properties of stain-etched porous silicon, physica status solidi (a) 210 (10) (2013) 2174–2177.

[140] R. Chaoui, B. Mahmoudi, Y. Si Ahmed, Porous silicon antireflection layer for solar cells using metal-assisted chemical etching, physica status solidi (a) 205 (7) (2008) 1724–1728.

[141] S. P. Scheeler, S. Ullrich, S. Kudera, C. Pacholski, Fabrication of porous silicon by metal-assisted etching using highly ordered gold nanoparticle arrays, Nanoscale research letters 7 (1) (2012) 450.

[142] A. Kiani, K. Venkatakrishnan, B. Tan, Micro/nano scale amorphization of silicon by femtosecond laser irradiation, Optics express 17 (19) (2009) 16518–16526.

[143] A. Kiani, K. Venkatakrishnan, B. Tan, Direct laser writing of amorphous silicon on si-substrate induced by high repetition femtosecond pulses, Journal of Applied Physics 108 (7) (2010) 074907.

[144] A. Kiani, K. Venkatakrishnan, B. Tan, Direct patterning of silicon oxide on si-substrate induced by femtosecond laser, Optics express 18 (3) (2010) 1872–1878.

[145] G. Sberveglieri, G. Faglia, S. Groppelli, P. Nelli, A. Taroni, A novel pvd technique for the preparation of sno 2 thin films as c 2 h 5 oh sensors, Sensors and Actuators B: Chemical 7 (1) (1992) 721–726.

[146] S. Ansari, Z. Ansari, H.-K. Seo, G.-S. Kim, Y.-S. Kim, G. Khang, H.-S. Shin, Urea sensor based on tin oxide thin films prepared by modified plasma enhanced cvd, Sensors and Actuators B: Chemical 132 (1) (2008) 265–271.

[147] J. Elam, M. Groner, S. George, Viscous flow reactor with quartz crystal microbalance for thin film growth by atomic layer deposition, Review of Scientific Instruments 73 (8) (2002) 2981–2987.

[148] C. Guan, X. Wang, Q. Zhang, Z. Fan, H. Zhang, H. J. Fan, Highly stable and reversible lithium storage in sno2 nanowires surface coated with a uniform hollow shell by atomic layer deposition, Nano letters 14 (8) (2014) 4852–4858.

[149] Y. S. Jung, A. S. Cavanagh, L. A. Riley, S.-H. Kang, A. C. Dillon, M. D. Groner, S. M. George, S.-H. Lee, Ultrathin direct atomic layer deposition on composite electrodes for highly durable and safe li-ion batteries, Advanced Materials 22 (19) (2010) 2172–2176.

[150] L. Schwiebert, S. K. Gupta, J. Weinmann, Research challenges in wireless networks of biomedical sensors, in: Proceedings of the 7th annual international conference on Mobile computing and networking, ACM, 2001, pp. 151–165.

[151] R. Kamal, M. O. Rahman, C. S. Hong, A lightweight temperature scheduling routing algorithm for an implanted sensor network, in: ICT Convergence (ICTC), 2011 International Conference on, IEEE, 2011, pp. 396–400.

[152] A. Kiani, N. B. Patel, B. Tan, K. Venkatakrishnan, Leaf-like nanotips synthesized on femtosecond laser-irradiated dielectric material, Journal of Applied Physics 117 (7) (2015) 074306.

[153] B. R. Tull, J. E. Carey, E. Mazur, J. P. McDonald, S. M. Yalisove, Silicon surface morphologies after femtosecond laser irradiation, Mrs Bulletin 31 (8) (2006) 626–633.

[154] S. Choopun, N. Hongsith, P. Mangkorntong, N. Mangkorntong, Zinc oxide nanobelts by rf sputtering for ethanol sensor, Physica E: Low-dimensional Systems and Nanostructures 39 (1) (2007) 53–56.

[155] G. Sberveglieri, L. Depero, S. Groppelli, P. Nelli, Wo3 sputtered thin films for nox monitoring, Sensors and Actuators B: Chemical 26 (1-3) (1995) 89–92.

[156] T. S. Kim, Y. B. Kim, K. S. Yoo, G. S. Sung, H. J. Jung, Sensing characteristics of dc reactive sputtered wo 3 thin films as an no x gas sensor, Sensors and Actuators B: Chemical 62 (2) (2000) 102–108.

[157] J. Zeng, M. Hu, W. Wang, H. Chen, Y. Qin, No 2-sensing properties of porous wo 3 gas sensor based on anodized sputtered tungsten thin film, Sensors and Actuators B: Chemical 161 (1) (2012) 447–452.

[158] C.-J. Jin, T. Yamazaki, Y. Shirai, T. Yoshizawa, T. Kikuta, N. Nakatani, H. Takeda, Dependence of no 2 gas sensitivity of wo 3 sputtered films on film density, Thin Solid Films 474 (1) (2005) 255–260.

[159] Y. Shen, T. Yamazaki, Z. Liu, D. Meng, T. Kikuta, N. Nakatani, Influence of effective surface area on gas sensing properties of wo 3 sputtered thin films, Thin Solid Films 517 (6) (2009) 2069–2072.

[160] M. Stankova, X. Vilanova, E. Llobet, J. Calderer, C. Bittencourt, J. Pireaux, X. Correig, Influence of the annealing and operating temperatures on the gas-sensing properties of rf sputtered wo 3 thin-film sensors, Sensors and Actuators B: Chemical 105 (2) (2005) 271–277.

[161] G. Bräuer, B. Szyszka, M. Vergöhl, R. Bandorf, Magnetron sputtering–milestones of 30 years, Vacuum 84 (12) (2010) 1354–1359.

[162] J.-H. Lee, D.-J. Lee, Effects of cdcl 2 treatment on the properties of cds films prepared by rf magnetron sputtering, Thin Solid Films 515 (15) (2007) 6055–6059.

[163] R. M. Fleming, M. L. Steigerwald, Y.-H. Wong, S. M. Zahurak, Sputtering method for forming dielectric films, uS Patent 6,290,822 (Sep. 18 2001).

[164] R. Scholl, Power systems for reactive sputtering of insulating films, Surface and Coatings Technology 93 (1) (1997) 7–13.

[165] S. Bruns, M. Vergöhl, O. Werner, T. Wallendorf, High rate deposition of mixed oxides by controlled reactive magnetron-sputtering from metallic targets, Thin Solid Films 520 (12) (2012) 4122–4126.

[166] F. Mafuné, J.-y. Kohno, Y. Takeda, T. Kondow, H. Sawabe, Formation and size control of silver nanoparticles by laser ablation in aqueous solution, The Journal of Physical Chemistry B 104 (39) (2000) 9111–9117.

[167] B. N. Chichkov, C. Momma, S. Nolte, F. Von Alvensleben, A. Tünnermann, Femtosecond, picosecond and nanosecond laser ablation of solids, Applied Physics A 63 (2) (1996) 109–115.

[168] A. Wisitsoraat, A. Tuantranont, C. Thanachayanont, V. Patthanasettakul, P. Singjai, Electron beam evaporated carbon nanotube dispersed sno 2 thin film gas sensor, Journal of electroceramics 17 (1) (2006) 45–49.

[169] A. Star, V. Joshi, S. Skarupo, D. Thomas, J.-C. P. Gabriel, Gas sensor array based on metal-decorated carbon nanotubes, The Journal of Physical Chemistry B 110 (42) (2006) 21014–21020.

[170] A. Irrera, E. Pecora, F. Priolo, Control of growth mechanisms and orientation in epitaxial si nanowires grown by electron beam evaporation, Nanotechnology 20 (13) (2009) 135601.

[171] E. F. Pecora, A. Irrera, P. Artoni, S. Boninelli, C. Bongiorno, C. Spinella, F. Priolo, Heteroepitaxial growth and faceting of ge nanowires on si (111) by electron-beam evaporation, Electrochemical and Solid-State Letters 13 (5) (2010) K53–K55.

[172] A. Kolmakov, D. Klenov, Y. Lilach, S. Stemmer, M. Moskovits, Enhanced gas sensing by individual sno2 nanowires and nanobelts functionalized with pd catalyst particles, Nano Letters 5 (4) (2005) 667–673.

[173] S. Durrani, E. Khawaja, M. Al-Kuhaili, Co-sensing properties of undoped and doped tin oxide thin films prepared by electron beam evaporation, Talanta 65 (5) (2005) 1162–1167.

[174] M. C. McAlpine, H. Ahmad, D. Wang, J. R. Heath, Highly ordered nanowire arrays on plastic substrates for ultrasensitive flexible chemical sensors, Nature materials 6 (5) (2007) 379–384.

[175] V. Logeeswaran, N. P. Kobayashi, M. S. Islam, W. Wu, P. Chaturvedi, N. X. Fang, S. Y. Wang, R. S. Williams, Ultrasmooth silver thin films deposited with a germanium nucleation layer, Nano letters 9 (1) (2008) 178–182.

[176] Y.-S. Shim, D. H. Kim, H. Y. Jeong, Y. H. Kim, S. H. Nahm, C.-Y. Kang, J.-S. Kim, W. Lee, H. W. Jang, Utilization of both-side metal decoration in close-packed sno 2 nanodome arrays for ultrasensitive gas sensing, Sensors and Actuators B: Chemical 213 (2015) 314–321.

[177] I.-S. Hwang, E.-B. Lee, S.-J. Kim, J.-K. Choi, J.-H. Cha, H.-J. Lee, B.-K. Ju, J.-H. Lee, Gas sensing properties of sno 2 nanowires on micro-heater, Sensors and Actuators B: Chemical 154 (2) (2011) 295–300.

[178] I.-S. Hwang, J.-K. Choi, H.-S. Woo, S.-J. Kim, S.-Y. Jung, T.-Y. Seong, I.-D. Kim, J.-H. Lee, Facile control of c2h5oh sensing characteristics by decorating discrete ag nanoclusters on sno2 nanowire networks, ACS applied materials & interfaces 3 (8) (2011) 3140–3145.

[179] Y. Zhuang, Challenges of electro-osmotic consolidation in large scale application, Geosynthetics 2015 (2015) 447–449.

[180] M. J. Lombardi, G. J. Reynolds, R. F. Foster, R. C. Rowan Jr, F. T. Turner, Vacuum-processing chamber-shield and multi-chamber pumping method, uS Patent 7,001,491 (Feb. 21 2006).

[181] D. M. Mattox, Physical vapor deposition (pvd) processes, Metal Finishing 100 (2002) 394–408.

[182] M. Matsumoto, N. Yamaguchi, H. Matsubara, Low thermal conductivity and high temperature stability of zro 2–y 2 o 3–la 2 o 3 coatings produced by electron beam pvd, Scripta Materialia 50 (6) (2004) 867–871.

[183] Q. Bao, C. Chen, D. Wang, Q. Ji, T. Lei, Pulsed laser deposition and its current research status in preparing hydroxyapatite thin films, Applied Surface Science 252 (5) (2005) 1538–1544.

[184] D. Crippa, G. L. Valente, A. Ruggiero, L. Neri, R. Reitano, L. Calcagno, G. Foti, M. Mauceri, S. Leone, G. Pistone, et al., New achievements on cvd based methods for sic epitaxial growth, in: Materials Science Forum, Vol. 483, Trans Tech Publ, 2005, pp. 67–72.

[185] J. Zimmer, K. Ravi, Aspects of scaling cvd diamond reactors, Diamond and related materials 15 (2) (2006) 229–233.

[186] C. A. R. Carvalho, T. C. Fagundes, V. J. Trava-airoldi, M. F. L. Navarro, et al., The use of cvd diamond burs for ultraconservative cavity preparations: a report of two cases, Journal of Esthetic and Restorative Dentistry 19 (1) (2007) 19–29.

[187] B. S. Harrison, A. Atala, Carbon nanotube applications for tissue engineering, Biomaterials 28 (2) (2007) 344–353.

[188] A. Ghosh, S. Basu, Spray/cvd deposition and characterisation of surface modified zinc oxide thick films for gas sensor, Materials Chemistry and Physics 27 (1) (1991) 45–54.

[189] S. Roy, S. Basu, Improved zinc oxide film for gas sensor applications, Bulletin of Materials Science 25 (6) (2002) 513–515.

[190] D. Barreca, D. Bekermann, E. Comini, A. Devi, R. A. Fischer, A. Gasparotto, C. Maccato, G. Sberveglieri, E. Tondello, 1d zno nano-assemblies by plasma-cvd as chemical sensors for flammable and toxic gases, Sensors and Actuators B: Chemical 149 (1) (2010) 1–7.

[191] L. Wang, Y. Kang, X. Liu, S. Zhang, W. Huang, S. Wang, Zno nanorod gas sensor for ethanol detection, Sensors and Actuators B: Chemical 162 (1) (2012) 237–243.

[192] Q. Lin, Y. Li, M. Yang, Highly sensitive and ultrafast response surface acoustic wave humidity sensor based on electrospun polyaniline/poly (vinyl butyral) nanofibers, Analytica chimica acta 748 (2012) 73–80.

[193] P. Jiang, J. Jie, Y. Yu, Z. Wang, C. Xie, X. Zhang, C. Wu, L. Wang, Z. Zhu, L. Luo, Aluminium-doped n-type zns nanowires as high-performance uv and humidity sensors, Journal of Materials Chemistry 22 (14) (2012) 6856–6861.

[194] M. Yin, F. Yang, Z. Wang, M. Zhu, M. Liu, X. Xu, Z. Li, A fast humidity sensor based on li+-doped sno2 one-dimensional porous nanofibers, Materials 10 (5) (2017) 535.

[195] S. Borini, R. White, D. Wei, M. Astley, S. Haque, E. Spigone, N. Harris, J. Kivioja, T. Ryhanen, Ultrafast graphene oxide humidity sensors, ACS nano 7 (12) (2013) 11166–11173.

[196] Y. H. Kwak, D. S. Choi, Y. N. Kim, H. Kim, D. H. Yoon, S.-S. Ahn, J.-W. Yang, W. S. Yang, S. Seo, Flexible glucose sensor using cvd-grown graphene-based field effect transistor, Biosensors and Bioelectronics 37 (1) (2012) 82–87.

[197] S. Xu, S. Jiang, C. Zhang, W. Yue, Y. Zou, G. Wang, H. Liu, X. Zhang, M. Li, Z. Zhu, et al., Ultrasensitive label-free detection of dna hybridization by sapphire-based graphene field-effect transistor biosensor, Applied Surface Science 427 (2018) 1114–1119.

[198] Y. Wang, L. Wang, T. Yang, X. Li, X. Zang, M. Zhu, K. Wang, D. Wu, H. Zhu, Wearable and highly sensitive graphene strain sensors for human motion monitoring, Advanced Functional Materials 24 (29) (2014) 4666–4670.

[199] A. Smith, F. Niklaus, A. Paussa, S. Vaziri, A. C. Fischer, M. Sterner, F. Forsberg, A. Delin, D. Esseni, P. Palestri, et al., Electromechanical piezoresistive sensing in suspended graphene membranes, Nano letters 13 (7) (2013) 3237–3242.

[200] N. Liao, Y. Li, S. Jin, G. Liu, Q. Wan, S. Sang, D. Su, Effects of catalysts state on the synthesis of mwcnts modified expanded graphite through microwave-assisted pyrolysis of ethanol, Journal of Materials Science 52 (19) (2017) 11442–11452.

[201] M. Iannazzo, E. Alarcon, H. Pandey, V. Passi, M. C. Lemme, Cvd graphene-fet based cascode circuits: A design exploration and fabrication towards intrinsic gain enhancement, in: Solid-State Device Research Conference (ESSDERC), 2016 46th European, IEEE, 2016, pp. 244–247.

[202] X. Zeng, H. Hirwa, M. Ortel, H. C. Nerl, V. Nicolosi, V. Wagner, Growth of large sized two-dimensional mos 2 flakes in aqueous solution, Nanoscale 9 (19) (2017) 6575–6580.

[203] J. Creighton, P. Ho, Introduction to chemical vapor deposition (cvd), Chemical vapor deposition 2 (2001) 1–22.

[204] Y. Hamedani, P. Macha, T. J. Bunning, R. R. Naik, M. C. Vasudev, Plasma-enhanced chemical vapor deposition: Where we are and the outlook for the future, in: Chemical Vapor Deposition-Recent Advances and Applications in Optical, Solar Cells and Solid State Devices, InTech, 2016.

[205] R. Ye, Y. Chyan, J. Zhang, Y. Li, X. Han, C. Kittrell, J. M. Tour, Laser-induced graphene formation on wood, Advanced Materials 29 (37).

[206] A. Saenger, B. Sell, H. Seidl, T. Hecht, M. Gutsche, Method and device for depositing thin layers via ald/cvd processes in combination with rapid thermal processes, uS Patent 6,835,417 (Dec. 28 2004).

[207] E. Granneman, P. Fischer, D. Pierreux, H. Terhorst, P. Zagwijn, Batch ald: Characteristics, comparison with single wafer ald, and examples, Surface and coatings technology 201 (22) (2007) 8899–8907.

[208] R. G. Gordon, Ald precursors and reaction mechanisms, in: Atomic Layer Deposition for Semiconductors, Springer, 2014, pp. 15–46.

[209] B. Abendroth, T. Moebus, S. Rentrop, R. Strohmeyer, M. Vinnichenko, T. Weling, H. Stöcker, D. C. Meyer, Atomic layer deposition of tio 2 from tetrakis (dimethylamino) titanium and h 2 o, Thin Solid Films 545 (2013) 176–182.

[210] H. Kim, C. Detavenier, O. Van der Straten, S. Rossnagel, A. Kellock, D.-G. Park, Robust ta n x diffusion barrier for cu-interconnect technology with subnanometer thickness by metal-organic plasma-enhanced atomic layer deposition, Journal of applied physics 98 (1) (2005) 014308.

[211] K. Endo, T. Tatsumi, Metal organic atomic layer deposition of high-k gate dielectrics using plasma oxidation, Japanese Journal of Applied Physics 42 (6B) (2003) L685.

[212] S. M. George, Atomic layer deposition: an overview, Chemical reviews 110 (1) (2009) 111–131.

[213] M. Ritala, K. Kukli, A. Rahtu, P. I. Räisänen, M. Leskelä, T. Sajavaara, J. Keinonen, Atomic layer deposition of oxide thin films with metal alkoxides as oxygen sources, Science 288 (5464) (2000) 319–321.

[214] M. Ritala, J. Niinistö, Atomic layer deposition, Chemical Vapor Deposition: Precursors, Processes and Application (2009) 158–206.

[215] A. A. Chaaya, M. Bechelany, S. Balme, P. Miele, Zno 1d nanostructures designed by combining atomic layer deposition and electrospinning for uv sensor applications, Journal of Materials Chemistry A 2 (48) (2014) 20650–20658.

[216] C.-Y. Chang, K.-T. Lee, W.-K. Huang, H.-Y. Siao, Y.-C. Chang, High-performance, air-stable, low-temperature processed semitransparent perovskite solar cells enabled by atomic layer deposition, Chemistry of Materials 27 (14) (2015) 5122–5130.

[217] T. Choi, S. H. Kim, C. W. Lee, H. Kim, S.-K. Choi, S.-H. Kim, E. Kim, J. Park, H. Kim, Synthesis of carbon nanotube–nickel nanocomposites using atomic layer deposition for high-performance non-enzymatic glucose sensing, Biosensors and Bioelectronics 63 (2015) 325–330.

[218] E. M. Lotfabad, P. Kalisvaart, K. Cui, A. Kohandehghan, M. Kupsta, B. Olsen, D. Mitlin, Ald tio 2 coated silicon nanowires for lithium ion battery anodes with enhanced cycling stability and coulombic efficiency, Physical Chemistry Chemical Physics 15 (32) (2013) 13646–13657.

[219] H. Feng, J. Lu, P. C. Stair, J. W. Elam, Alumina over-coating on pd nanoparticle catalysts by atomic layer deposition: Enhanced stability and reactivity, Catalysis letters 141 (4) (2011) 512–517.

[220] R. Liu, Z. Zheng, J. Spurgeon, X. Yang, Enhanced photoelectrochemical water-splitting performance of semiconductors by surface passivation layers, Energy & Environmental Science 7 (8) (2014) 2504–2517.

[221] A. M. Morales, C. M. Lieber, A laser ablation method for the synthesis of crystalline semiconductor nanowires, Science 279 (5348) (1998) 208–211.

[222] W. Xue, B. V. Krishna, A. Bandyopadhyay, S. Bose, Processing and biocompatibility evaluation of laser processed porous titanium, Acta biomaterialia 3 (6) (2007) 1007–1018.

[223] D. Ashkenasi, A. Rosenfeld, H. Varel, M. Wähmer, E. Campbell, Laser processing of sapphire with picosecond and sub-picosecond pulses, Applied Surface Science 120 (1) (1997) 65–80.

[224] V. K. Balla, S. Bodhak, S. Bose, A. Bandyopadhyay, Porous tantalum structures for bone implants: fabrication, mechanical and in vitro biological properties, Acta biomaterialia 6 (8) (2010) 3349–3359.

[225] Z. Shen, J. J. Thomas, C. Averbuj, K. M. Broo, M. Engelhard, J. E. Crowell, M. Finn, G. Siuzdak, Porous silicon as a versatile platform for laser desorption/ionization mass spectrometry, Analytical Chemistry 73 (3) (2001) 612–619.

[226] K. Leong, K. Phua, C. Chua, Z. Du, K. Teo, Fabrication of porous polymeric matrix drug delivery devices using the selective laser sintering technique, Proceedings of the Institution of Mechanical Engineers, Part H: Journal of Engineering in Medicine 215 (2) (2001) 191–192.

[227] J. Gao, T. Gao, M. J. Sailor, Porous-silicon vapor sensor based on laser interferometry, Applied Physics Letters 77 (6) (2000) 901–903.

[228] L. De Stefano, I. Rendina, L. Moretti, S. Tundo, A. M. Rossi, Smart optical sensors for chemical substances based on porous silicon technology, Applied Optics 43 (1) (2004) 167–172.

[229] M. Chen, Z. Wang, D. Han, F. Gu, G. Guo, Porous zno polygonal nanoflakes: synthesis, use in high-sensitivity no2 gas sensor, and proposed mechanism of gas sensing, The Journal of Physical Chemistry C 115 (26) (2011) 12763–12773.

[230] Y.-C. Yeh, T.-Y. Tseng, D.-A. Chang, Electrical properties of tio2-k2ti6o13 porous ceramic humidity sensor, Journal of the American Ceramic Society 73 (7) (1990) 1992–1998.

[231] W. Xue, B. V. Krishna, A. Bandyopadhyay, S. Bose, Processing and biocompatibility evaluation of laser processed porous titanium, Acta biomaterialia 3 (6) (2007) 1007–1018.

[232] P. H. Warnke, T. Douglas, P. Wollny, E. Sherry, M. Steiner, S. Galonska, S. T. Becker, I. N. Springer, J. Wiltfang, S. Sivananthan, Rapid prototyping: porous titanium alloy scaffolds produced by selective laser melting for bone tissue engineering, Tissue engineering part c: Methods 15 (2) (2008) 115–124.

[233] L.-j. Chen, L. Ting, Y.-M. Li, H. Hao, Y.-H. Hu, Porous titanium implants fabricated by metal injection molding, Transactions of Nonferrous Metals Society of China 19 (5) (2009) 1174–1179.

[234] Y. Chen, B. Feng, Y. Zhu, J. Weng, J. Wang, X. Lu, Fabrication of porous titanium implants with biomechanical compatibility, Materials Letters 63 (30) (2009) 2659–2661.

[235] H. W. Tom, G. Aumiller, C. Brito-Cruz, Time-resolved study of laser-induced disorder of si surfaces, Physical review letters 60 (14) (1988) 1438.

[236] P. Stampfli, K. Bennemann, Theory for the instability of the diamond structure of si, ge, and c induced by a dense electron-hole plasma, Physical Review B 42 (11) (1990) 7163.

[237] P. Stampfli, K. Bennemann, Dynamical theory of the laser-induced lattice instability of silicon, Physical Review B 46 (17) (1992) 10686.

[238] M. Muniz-Miranda, C. Gellini, E. Giorgetti, Surface-enhanced raman scattering from copper nanoparticles obtained by laser ablation, The Journal of Physical Chemistry C 115 (12) (2011) 5021–5027.

[239] E. Giorgetti, M. Muniz-Miranda, P. Marsili, D. Scarpellini, F. Giammanco, Stable gold nanoparticles obtained in pure acetone by laser ablation with different wavelengths, Journal of Nanoparticle Research 14 (1) (2012) 648.

[240] J. Reif, Basic physics of femtosecond laser ablation, Laser Surface Interactions for New Materials Production 130 (2010) 19–41.

[241] R. Fabbro, J. Fournier, P. Ballard, D. Devaux, J. Virmont, Physical study of laser-produced plasma in confined geometry, Journal of applied physics 68 (2) (1990) 775–784.

[242] D. Devaux, R. Fabbro, L. Tollier, E. Bartnicki, Generation of shock waves by laser-induced plasma in confined geometry, Journal of Applied Physics 74 (4) (1993) 2268–2273.

[243] F. Sima, C. Ristoscu, D. Caiteanu, C. N. Mihailescu, N. Stefan, I. N. Mihailescu, G. Prodan, V. Ciupina, E. Palcevskis, J. Krastins, et al., Biocompatibility and bioactivity enhancement of ce stabilized zro2 doped ha coatings by controlled porosity change of al2o3 substrates, Journal of Biomedical Materials Research Part B: Applied Biomaterials 96 (2) (2011) 218–224.

[244] B. Tan, K. Venkatakrishnan, Synthesis of fibrous nanoparticle aggregates by femtosecond laser ablation in air, Optics express 17 (2) (2009) 1064–1069.

[245] C. Colpitis, A. Kiani, Synthesis of bioactive three-dimensional silicon-oxide nanofibrous structures on the silicon substrate for bionic devices' fabrication, Nanomaterials and Nanotechnology 6 (2016) 8.

[246] V. Švrček, D. Mariotti, M. Kondo, Ambient-stable blue luminescent silicon nanocrystals prepared by nanosecond-pulsed laser ablation in water, Optics express 17 (2) (2009) 520–527.

[247] Y.-L. Khung, S. D. Graney, N. H. Voelcker, Micropatterning of porous silicon films by direct laser writing, Biotechnology progress 22 (5) (2006) 1388–1393.

[248] M. Ball, S. Downes, C. Scotchford, E. Antonov, V. Bagratashvili, V. Popov, W.-J. Lo, D. Grant, S. Howdle, Osteoblast growth on titanium foils coated with hydroxyapatite by pulsed laser ablation, Biomaterials 22 (4) (2001) 337–347.

[249] P. G. Kuzmin, G. A. Shafeev, V. V. Bukin, S. V. Garnov, C. Farcau, R. Carles, B. Warot-Fontrose, V. Guieu, G. Viau, Silicon nanoparticles produced

by femtosecond laser ablation in ethanol: size control, structural characterization, and optical properties, The Journal of Physical Chemistry C 114 (36) (2010) 15266–15273.

[250] J. A. Powell, K. Venkatakrishnan, B. Tan, Programmable sers active substrates for chemical and biosensing applications using amorphous/crystalline hybrid silicon nanomaterial, Scientific reports 6 (2016) 19663.

[251] J. A. Powell, K. Venkatakrishnan, B. Tan, Hybridized enhancement of the sers detection of chemical and bio-marker molecules through au nanosphere ornamentation of hybrid amorphous/crystalline si nanoweb nanostructure biochip devices, Journal of Materials Chemistry B 4 (34) (2016) 5713–5728.

[252] J. A. Powell, K. Venkatakrishnan, B. Tan, A primary sers-active interconnected si-nanocore network for biomolecule detection with plasmonic nanosatellites as a secondary boosting mechanism, RSC Advances 7 (53) (2017) 33688–33700.

[253] I. Makra, A. Brajnovits, G. Jágerszki, P. Fürjes, R. E. Gyurcsányi, Potentiometric sensing of nucleic acids using chemically modified nanopores, Nanoscale 9 (2) (2017) 739–747.

[254] H. Carslaw, J. Jaeger, Conduction of heat in solids: Oxford Science Publications, ch 10, Oxford, England, 1959.

[255] J. Ready, Effects of high-power laser radiation, ch 3, Elsevier, 2012.

[256] S. T. Hendow, S. A. Shakir, Structuring materials with nanosecond laser pulses, Optics Express 18 (10) (2010) 10188–10199.

[257] L. B. Valdes, Resistivity measurements on germanium for transistors, Proceedings of the IRE 42 (2) (1954) 420–427.

[258] T. Watanabe, H. Watakabe, T. Sameshima, M. Miyasaka, Electrical properties of solid-phase crystallized polycrystalline silicon films, Applied Physics A 77 (1) (2003) 87–92.

[259] B. Van Zeghbroeck, Principles of electronic devices (ch 2.7), University of Colorado.

[260] M. A. Alam, nanohub-u: Principles of electronic nanobiosensors, Online Course (2017).

[261] P. R. Nair, M. A. Alam, Design considerations of silicon nanowire biosensors, IEEE Transactions on Electron Devices 54 (12) (2007) 3400–3408.

[262] P. Nair, M. Alam, Performance limits of nanobiosensors, Applied physics letters 88 (23) (2006) 233120.

[263] L. Höfler, R. E. Gyurcsányi, Nanosensors lost in space. a random walk study of single molecule detection with single-nanopore sensors, Analytica chimica acta 722 (2012) 119–126.

[264] I. Makra, R. E. Gyurcsányi, Electrochemical sensing with nanopores: a mini review, Electrochemistry Communications 43 (2014) 55–59.

[265] R. Gupta, Q. Xiong, C. Adu, U. Kim, P. Eklund, Laser-induced fano resonance scattering in silicon nanowires, Nano Letters 3 (5) (2003) 627–631.

[266] V. Schmidt, S. Senz, U. Gösele, Influence of the si/sio 2 interface on the charge carrier density of si nanowires, Applied Physics A: Materials Science & Processing 86 (2) (2007) 187–191.

[267] V. Schmidt, J. Wittemann, U. Gosele, Growth, thermodynamics, and electrical properties of silicon nanowires, Chemical reviews 110 (1) (2010) 361–388.

[268] E. H. Nicollian, J. R. Brews, E. H. Nicollian, MOS (metal oxide semiconductor) physics and technology, Vol. 1987, Wiley New York et al., 1982.

[269] A. Kiani, K. Venkatakrishnan, B. Tan, V. Venkataramanan, Maskless lithography using silicon oxide etch-stop layer induced by megahertz repetition femtosecond laser pulses, Optics express 19 (11) (2011) 10834–10842.

[270] H. Wang, X. Liu, Z. M. Zhang, Absorption coefficients of crystalline silicon at wavelengths from 500 nm to 1000 nm, International Journal of Thermophysics 34 (2) (2013) 213–225.

[271] E. Loenen, L. Van der Tempel, Determination of absorption coefficients of glasses at high tempera-tures, by measuring the thermal emission, Tech. rep., Philips Research (1996).

[272] A. Q. Jiang, C. Wang, K. J. Jin, X. B. Liu, J. F. Scott, C. S. Hwang, T. A. Tang, H. B. Lu, G. Z. Yang, A resistive memory in semiconducting bifeo3 thin-film capacitors, Advanced materials 23 (10) (2011) 1277–1281.

[273] J. S. Park, W.-J. Maeng, H.-S. Kim, J.-S. Park, Review of recent developments in amorphous oxide semiconductor thin-film transistor devices, Thin solid films 520 (6) (2012) 1679–1693.

[274] F.-C. Chiu, A review on conduction mechanisms in dielectric films, Advances in Materials Science and Engineering 2014.

[275] G. Wang, L. Zhang, J. Zhang, A review of electrode materials for electrochemical supercapacitors, Chemical Society Reviews 41 (2) (2012) 797–828.

[276] J. Li, X. Cheng, A. Shashurin, M. Keidar, Review of electrochemical capacitors based on carbon nanotubes and graphene, Graphene 1 (01) (2012) 1.

[277] M. Suryawanshi, G. Agawane, S. Bhosale, S. Shin, P. Patil, J. Kim, A. Moholkar, Czts based thin film solar cells: a status review, Materials Technology 28 (1-2) (2013) 98–109.

[278] M. Koo, K.-I. Park, S. H. Lee, M. Suh, D. Y. Jeon, J. W. Choi, K. Kang, K. J. Lee, Bendable inorganic thin-film battery for fully flexible electronic systems, Nano letters 12 (9) (2012) 4810–4816.

[279] H. Choi, X. Li, Fabrication and application of micro thin film thermocouples for transient temperature measurement in nanosecond pulsed laser micromachining of nickel, Sensors and Actuators A: Physical 136 (1) (2007) 118–124.

[280] J.-H. Lee, N.-S. Kim, S.-S. Hong, J.-H. Lee, Enhanced extraction efficiency of ingan-based light-emitting diodes using 100-khz femtosecond-laser-scribing technology, IEEE Electron Device Letters 31 (3) (2010) 213–215.

[281] C. Luo, L. Lin, The application of nanosecond-pulsed laser welding technology in mems packaging with a shadow mask, Sensors and Actuators A: Physical 97 (2002) 398–404.

[282] T. Sugihara, T. Enomoto, Development of a cutting tool with a nano/micro-textured surfaceimprovement of anti-adhesive effect by considering the texture patterns, Precision Engineering 33 (4) (2009) 425–429.

[283] M. A. Green, M. J. Keevers, Optical properties of intrinsic silicon at 300 k, Progress in Photovoltaics: Research and Applications 3 (3) (1995) 189–192.

[284] E. Beder, C. Bass, W. Shackleford, Transmissivity and absorption of fused quartz between 0.22 μ and 3.5 μ from room temperature to 1500 c, Applied Optics 10 (10) (1971) 2263–2268.

Appendix

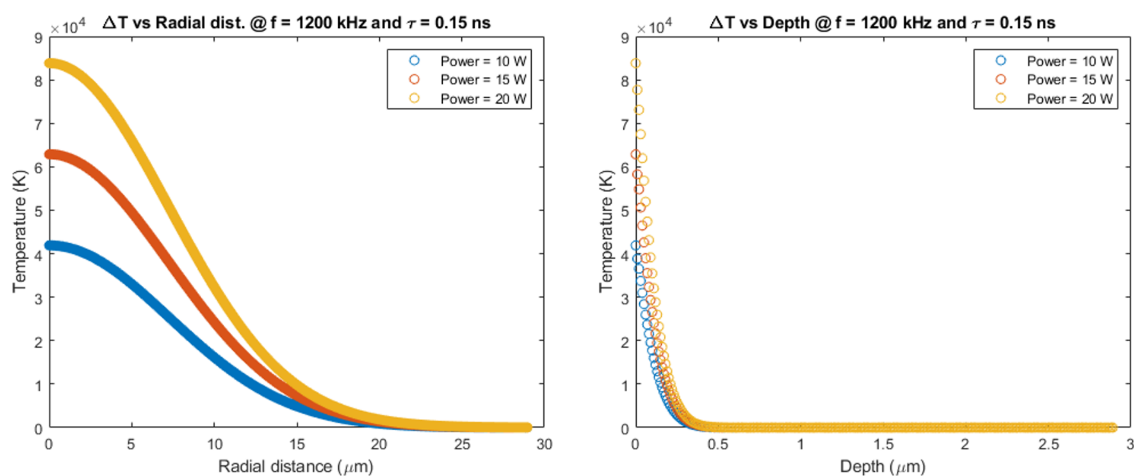

Figure 6.3: For various laser frequencies, plasma temperature ΔT at Si surface with respect to (a) radial distance from the center of focused laser spot and (b) depth of the surface being processed.

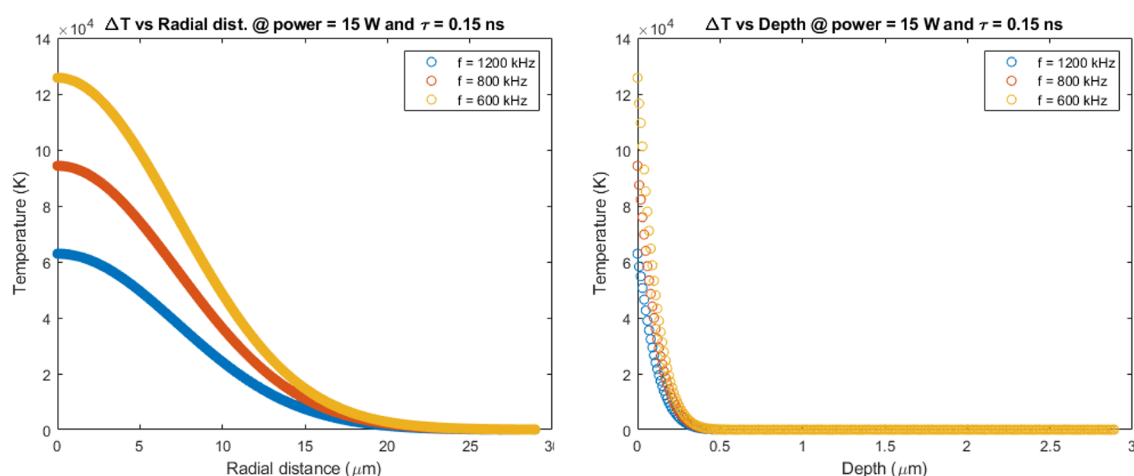

Figure 6.4: For various laser power values, plasma temperature ΔT at Si surface with respect to (a) radial distance from the center of focused laser spot and (b) depth of the surface being processed.